Abstract

When doing image guided surgery, it is important to find a proper alignment of the coordinate systems for the images and for the tracking system that tracks the positions of the surgeons tools. This report explores surface based methods for finding such an alignment, using either an optical shape measurement device, or surfaces gathered by passing the tracking tool along the surface of the patient. Accuracy and usability factors are explored, and compared to existing methods based on finding corresponding points

Preface

This report is the final delivery of my master thesis in computer science, specialising in image processing at the Norwegian University of Technology and Science (NTNU). The thesis work is done as the entire last half year of the five year master study, but builds heavily upon a previous preproject[3]. The work is done in cooperation with SINTEF MedTech, who has provided guidance and equipment for the work, and it is part of a larger internal SINTEF project on markerless patient registration. It is part of SINTEF MedTech's research on "future neurosurgery and improved patient treatment." [9].

Particular thanks to: Frank Lindseth for guidance and ideas, Geir Arne Tangen for help with positioning devices, experiments and CustusX fixes and to St. Olavs hospital for providing CT and MRI scans.

Contents

List of Tables

List of Figures

Nomenclature

Abbreviations

FLE Fiducial location error. The mean of the distance between the fiducials measured position and the unknown true position.

FRE Fiducial registration error. The mean of the distance between measured fiducial position in Moving data transformed with the resulting registration, and the measured fiducial position in Fixed data.

MCE Maximum correspondence error, a measure of registration accuracy.

NAI Noise amplification index, a measure of geometric constraint.

RCS Reference coordinate system (from dicom specification).

RMS Root mean square.

SVD Singular value decomposition. A method for decomposing a matrix into the product of two orthonormal and one diagonal matrices.

TRE Target registration error. The distance between one point in moving data, after registration, and the corresponding point in fixed data.

Glossary

Fixed data The target data set in a registration.

Moving data The dataset in a registration that is transformed.

Preoperative Done or acquired prior to surgery

Volume Or volume data or volume image. A three dimensional regular grid of voxels.

Voxel Three dimensional equivalent to a pixel.

Chapter 1

Introduction

In modern medicine there is an increasing desire to use available image data to guide and assist surgeons during operation. This field of research is called image guided surgery. An important part of any image guided surgery system is to align the medical imaged, usually captured beforehand to the patients current position in the operating room. This alignment procedure is called a patient registration. This report discusses the possibility of building an automatic patient registration system based on surfaces segmented from the medical images, and corresponding surfaces of the patient captured with either a tracking probe or a optical shape measurement device during surgery. The focuses is on accuracy and usability. The goal is to produce a system that can produce a patient registration with comparative or higher accuracy than registration using sticker fiducials, while being easier for the surgeon to use.

1.1 Traditional Patient Registration

Currently patient registration is usually done using point-based registration methods. This method works by manually, or semi-automatically finding corresponding points in preoperative data and in operating room coordinates, and then finding a geometric transformation that minimises the mean distance between corresponding points. There is currently two main ways to find corresponding points. These are discussed in the following sections.

1.1.1 Anatomical Landmarks

When registering the patient using anatomical landmarks the points are chosen to be distinct features in the human anatomy near the target area of the operation. Options include the tip of the nose and features in the ear for surgery in the head. These points are first located in the medical images, and then they are pointed to with a tracking probe

in the operating room. This results in a set of pairs of corresponding points, usable for the registration task.

1.1.2 Fiducial Markers

As an alternative to anatomical landmarks, fiducial markers are sometimes used. Fiducial markers are usually stickers filled with contrast in order to be highly visible in the desired image modality. These are attached to the patient before the imaging is done, and remain on until after the operation is completed. The registration procedure is very similar to the anatomical landmark method. First find the markers in the preoperative image data, then point to the marker using the tracking probe. This method provides better precision than the landmark based method, and it also has the potential for higher degree of automation, since the marker properties are well-defined and known in the image data. But the markers can potentially be uncomfortable for the patient. If the diagnosis was done based on images captured without fiducial markers this method will require an additional scan with markers attached, and this results in extra radiation doses for the patient. In some systems fiducial markers are attached to the patients bones with screws rather than to the skin with stickers. This allows for excellent accuracy, since these markers, unlike stickers, can not move, but inserting fixed fiducials introduces additional surgery for the patient.

1.2 System Overview

The envisioned system has the following main components:

- Optical shape measurement device
- Tracking system
- Navigation computer
- Modern medical imaging devices

The system works by importing the medical image data from the imaging device into the navigation computer that segments out the outer surface of the patient from this data. Then a surface representation is gathered from the operating room. When using the shape measurement device a point cloud representation of the patients outer surface is gathered. The point cloud is used to recreate a surface on the computer, and this surface is registered with the segmented surface from the imaging device. This part of the setup is shown in figure 1.1. Then the tracking devices reference frame

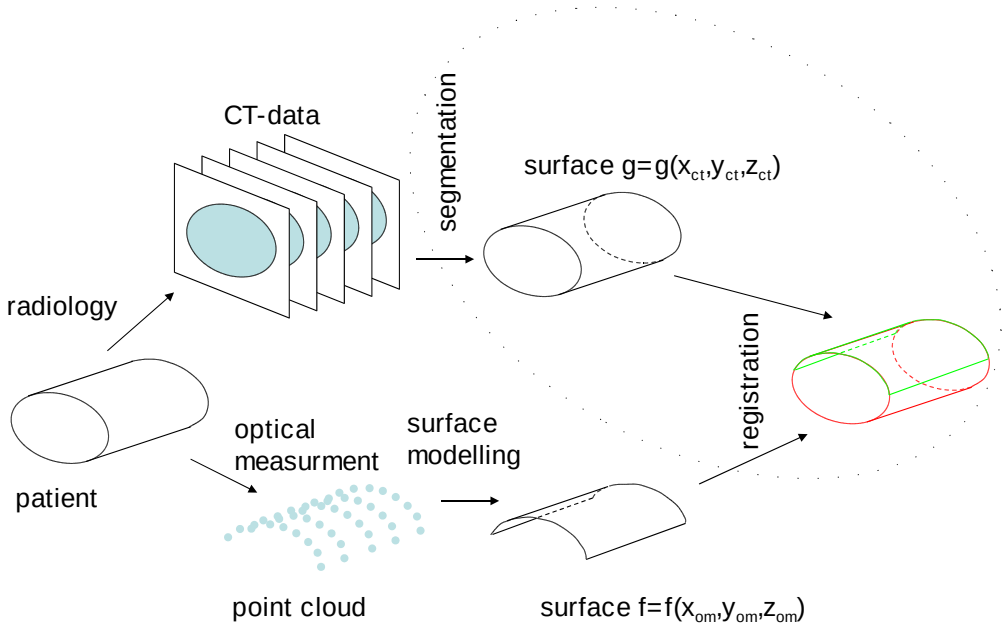

Figure 1.1: Overview of the first registration process. The parts emphasised in this report are in the dotted ellipse

is found in the shape measurement devices point-cloud and a registration is done between the shame measurement coordinate system and the tracking devices coordinate system. Combining these two registrations should result in a geometric transformation that maps coordinates from the tracking device into the preoperative medical images. Alternatively the surface could be gathered by moving the tracking probe along relevant parts of the patients outer surface while continuously storing the position, and then use this surface representation as well as the segmented surface to find the registration.

1.2.1 Tracking System

The tracking system used is the Passive Polaris system from Northern Digital Inc. This system consists of a position sensor and one or more tools. The position sensor consists of two infrared cameras and infrared light emitting diodes. The tools are fitted with three or more spheres designed to reflect infrared light. The position sensor detects the spheres with it's two cameras and use triangulation to find the position of the spheres in 3D space. The system then uses knowledge of the sphere configuration on the individual tools to give full six degree of freedom information about the tool positions. The position sensor needs line of sight to the tools in order to work, this mean that the sen-

sor might need to be moved if the area of interest get occluded from the sensors view. This would have resulted in a change of the coordinate system for the tracker tools. To overcome this problem, a special tool, called the reference frame, is attached to the operating table, and all tool coordinates given in the navigation computer are relative to this. The tracking system tracks the position and orientation of all the tools used. After the registration is completed, the tools are shown in the visualisation on the navigation computer, and relevant images can be automatically extracted from the volume based on the tools positions. A special tool, called the tracking probe, has no use other than sampling positions. This tool has a sharp tip with well defined position. When using the tracking device as the registration basis, this tool is pointed at the patients skin, and moved along the relevant anatomy while storing it's position, and thus gather a representation of the surface.

1.2.2 Optical Shape Measurement Device

The optical shape measurement device is a special device designed by SINTEF Fotonikk. It consists of a digital camera and a projector mounted with some distance between them, and directed at the same area. The projector illuminates the area of interest with a sequence of various stripe-patterns, and for each pattern the camera takes a picture of the area. The curvature of the stripes as seen from the camera gives information about the elevation of the object of interest at any given point. The stripe sequence is designed to calibrate the system, and to overcome problems when the object to measure have non-uniform colour. The output of the scan is a large set of points in 3D, typically around 100 000, all believed to be on the surface of the object to be scanned. The output of this scan is processed to detect the reference frame from the tracking system and the patient surface. This information will allow a full patient registration to be achieved.

1.2.3 Modern Medical Imaging Devices

Modern medicine have a wide variety of different imaging methods to show the inside of the patient. In this project we will use CT and MR scans. These scans results volume images that represent some property of the inside of the patient, like x-ray attenuation for CT. This information is used by the surgeon to plan the surgery before it is started, and to guide the surgeon during the procedure. In this system the CT/MR data is segmented to extract the outer surface. This surface is to be matched to the surface from the optical shape measurement device or tracking device.

1.2.4 Navigation Computer

The navigation computer is used to visualise the output of the imaging device. This is done both during planning and during surgery. The computer is attached to the shape measurement device and the tracking system, and it does all the calculations relating to the registration. During surgery the computer visualises the patient with all the surgeons tools shown on the screen. This allows for many things like showing the surgeon what is underneath the knife before he does the cut, or warning the surgeon if some of the tools are deviating from the planned course.

1.2.5 Alternative Solution

As an alternative solution, we will consider doing ordinary landmark based registration, and refine the result using surfaces gathered by rapidly sample the probes position while moving it along the surface of the patient in some pattern. This would allow to free the space of the shape measurement device from the operating room, and still give good accuracy without using fiducial markers.

1.3 Report Overview

The focus of this report is on the segmentation of the outer surface from volume data, and on matching this surface to the surface found in the shape measurement. The other parts of the system is being developed by other parts of SINTEF and is not the focus off this report, even though they will be part of the final test rig, and they will all affect the accuracy of the complete system. This is shown in figure 1.1.

The report starts by reviewing relevant theory on surface-based registration (chapter 3), registration accuracy (chapter 4) and accuracy measurement, as well as surface segmentation from volume data (chapter 5). Then the implementation is discussed and described (chapter 6). Chapter 7 shows some results of the methods and the results of some experiments. Chapter 8 analyses the results, and chapter 9 gives the conclusions. Finally future work is summarised in chapter 10.

1.3.1 Previous Work

In a previous project[3], surface based registration was explored and found to be feasible in a setting like this. This report will extend that work by replacing the segmentation methods used and improving the registration scheme. Furthermore this report will try to give experimental and analytical measures for the accuracy of the system.

Chapter 2

Problem Description

This chapter will further explain the registration problem, introduce some terminology and describe the input data in a bit more detail.

2.1 Registration

Registration is, according to Fitzpatrick's definition in [6] "the determination of a geometrical transformation that aligns points in one view of an object with corresponding points in another view of that object or another object". This definition is very broad, and covers a lot of different tasks, from aligning different images(Image registration) to aligning preoperative medical images to operating room instruments(Patient registration, which is the problem considered in this report), but does also cover lots of other tasks like comparing patient images to medical atlases, or comparing images of different patients, or images of the same patient at different times, or glueing together surface scans of objects from different angles to a complete model, to name a few. Fitzpatrick continues to give a eight dimensional categorisation of the general registration problem along the following axes:

Axis	Shape method	Tracker method	Point-based
Dimensionality	3	3	3
Basis	Surface	Surface	Corresponding Points
Transformation	Rigid Body	Rigid Body	Rigid Body
Interaction	Fully automatic	Semi-Automatic	Semi-Automatic
Optimisation	Local search	local search	Closed form
Modalities	CT/MR+shape	CT/MR+tracker probe	CT/MR+tracker probe
Subject	intra-patient	intra-patient	intra-patient
Object	Head	Head	Any

Table 2.1: Classification of registration tasks. Comparing the two methods proposed here with traditional point-based patient registration

For convenience, we name the view to be transformed "moving data", and the view that it should be transformed into "fixed data", or for short $\mathbf{M}$ and $\mathbf{F}$. These two are mathematically defined as the set of all points on the surface of the object in the respective views, for surface based registration, or as the ordered sets of corresponding points for point based registration. Other terms are also commonly used in the literature, these include data/model, source/target and left/right.

2.2 Rigid Body Transformations

As stated above, the registration task in question involves finding a rigid body transformation. A rigid body transformation is a transformation that consists of only rotations and translations. Using homogeneous coordinates[2] any rigid body transformation can be represented by a 4x4 matrix such as:

$$\mathbf{M} = \begin{bmatrix} R_{11} & R_{12} & R_{13} & T_1 \\ R_{21} & R_{22} & R_{23} & T_2 \\ R_{31} & R_{32} & R_{33} & T_3 \\ 0 & 0 & 0 & 1 \end{bmatrix} \tag{2.1}$$

Where R_{ij} are a 3x3 orthonormal rotation matrix[1], and T_i is a translation vector. We use $\mathbf{M}_{vn}$ to denote the rigid body transformation from coordinate system v to n. For pure translations or rotations we use $\mathbf{T}_{vn}$ or $\mathbf{R}_{vn}$ respectively.

Using homogeneous coordinates, and representing a vector as $\mathbf{v} = [x\ y\ z\ 0]^T$ and a point as $\mathbf{p} = [x\ y\ z\ 1]^T$ any transformation can be calculated using a simple matrix multiplication like this:

$$\mathbf{x}' = \mathbf{M}\mathbf{x} \tag{2.2}$$

It follows from this that

$$\mathbf{x}'' = \mathbf{M}_2\mathbf{x}' \tag{2.3}$$

which gives that

$$\mathbf{x}'' = \mathbf{M}_2\mathbf{M}\mathbf{x} = \mathbf{M}^*\mathbf{x} \tag{2.4}$$

if $\mathbf{M}^* = \mathbf{M}_2\mathbf{M}$. calculating $\mathbf{M}^*$ allow one to transform a large number of points

[1]Note that not all orthogonal matrices are pure rotation matrices, but some also hold point of line reflections

through the same set of transformations at the same cost of transforming the same set of points with only one transformation. This is a property that we will take advantage of, both in derivations later in the report and in implementation of the registration system.

2.3 Input Data

2.3.1 Volume Data

The term volume data, or volume image, is here used for the three-dimensional image data produced by MR and CT scanners. This data is effectively a three dimensional array of voxels. A voxel is a is basically a rectangular prism, that have a finite constant extent along each of the axes and is associated with a intensity value. The voxel size along the x and y axis is usually equal and a bit below one millimetre, and along the z axis the size is usually 1 mm or larger. The intensity value is usually 16 bits, of which only the 12 least significant bits are used. This results in about four thousand different intensity values per voxel.

2.3.2 Surface Data

Polygonal surface data models are used both as input from the shape measurement device, and as output of the segmentation process. The polygon data model can be viewed as a ordered list of *points*, where each point is three floating point numbers giving the points position in the coordinate system along each the access in unit millimetres. Following the list of points is a ordered list of *cells*. Each cell is a tuple of N indexes into the point list. These lists are followed by any number of arrays containing information about either the points or the cells. Common uses are to store normal-vectors for points and/or cells. Other properties could be gradients, curvature, colour etc.

Chapter 3

Registration Methods

This chapter gives an overview of methods and algorithms useful for patient registration with emphasis on surface based methods.

3.1 Point Based Methods

We will first briefly discuss some of the common point based registration methods, because they are an important part of most surface based methods.

3.1.1 Horn's Quaternion Solution

Horn presented the first closed form solution to the corresponding points registration problem in 1986[10]. He used unit quaternions to ease the development of a solution for finding the best translation, rotation and possibly scaling, in a least squares error sense, from a set of three or more points in three dimensions.

The method first finds the mass centre of the two point clouds. Using $\mathbf{M}$ and $\mathbf{F}$ as the two point sets, with N points each, this can be done as following.

$$\overline{\mathbf{m}} = \frac{1}{N}\sum_i \mathbf{m} \qquad\qquad \overline{\mathbf{f}} = \frac{1}{N}\sum_i \mathbf{f} \tag{3.1}$$

Let $\mathbf{m}'_i$ and $\mathbf{f}'_i$ be normalised versions of $\mathbf{m}_i$ and $\mathbf{f}_i$ with regard to the centroids, like this:

$$\mathbf{m}'_i = \mathbf{m}_i - \overline{\mathbf{m}} \qquad\qquad \mathbf{f}'_i = \mathbf{f}_i - \overline{\mathbf{f}} \tag{3.2}$$

The scale is found to be:

$$s = \sqrt{\frac{\sum_i ||\mathbf{f}'_i||^2}{\sum_i ||\mathbf{m}'_i||^2}} \tag{3.3}$$

The matrix:

$$\mathbf{M} = \sum_i \mathbf{m}'_i \mathbf{f}'^T_i = \begin{bmatrix} S_{xx} & S_{xy} & S_{xz} \\ S_{yx} & S_{yy} & S_{yz} \\ S_{zx} & S_{zy} & S_{zz} \end{bmatrix} \tag{3.4}$$

can easily be computed from the point pairs of the input, and it hold all the information needed for finding the rotation component of the transformation. The rotation is represented by the unit quaternion that is the eigenvector with the largest eigenvalue of the following matrix, constructed from additions and subtractions of the elements of $\mathbf{M}$:

$$\mathbf{N} = \begin{bmatrix} S_{xx}+S_{yy}+S_{zz} & S_{yz}-S_{zy} & S_{zx}-S_{xz} & S_{xy}-S_{yx} \\ S_{yz}-S_{zy} & S_{xx}-S_{yy}-S_{zz} & S_{xy}+S_{yx} & S_{zx}+S_{xz} \\ S_{zx}-S_{xz} & S_{xy}+S_{yx} & -S_{xx}+S_{yy}-S_{zz} & S_{yz}+S_{zy} \\ S_{xy}-S_{yx} & S_{zx}+S_{xz} & S_{yz}+S_{zy} & -S_{xx}-S_{yy}+S_{zz} \end{bmatrix} \tag{3.5}$$

The translation is, as the last step, found to be the vector difference between the centroid of the fixed points and the scaled and rotated centroid of the moving points, like this:

$$\mathbf{T} = \overline{\mathbf{f}} - sR(\overline{\mathbf{m}}) \tag{3.6}$$

This method has quite a few good sides compared to other methods. It is fast, requires no iteration and uses no approximation. It also makes sure that the result is purely rotation, scale and translation, even when finite precision arithmetics might cause rounding errors.

3.2 Singular Value Decomposition

One popular alternative to Horn's solution presented in among others [8], is to use singular value decomposition(SVD). This method finds the rotation part as an orthonormal rotation matrix.

Starting with the matrix

$$\mathbf{B} = \begin{bmatrix} \mathbf{b}_1 & \mathbf{b}_2 & \mathbf{b}_3 \end{bmatrix} \tag{3.7}$$

where

$$\mathbf{b}_k = \sum_i w_n \mathbf{f}'_{ik} \mathbf{m}'_i \tag{3.8}$$

where $\mathbf{f}'$ and $\mathbf{m}'$ are normalised versions of $\mathbf{f}$ and $\mathbf{m}$ as explained in equation (3.2). This matrix has the singular value decomposition

$$\mathbf{B} = \mathbf{UDV} \tag{3.9}$$

where $\mathbf{U}$ and $\mathbf{V}$ are orthonormal and $\mathbf{D}$ is diagonal. The rotation matrix is found to be

$$\mathbf{R} = \mathbf{V}^T\mathbf{U}^T \tag{3.10}$$

The translation part is finally found equivalently with Horns solution in equation (3.6).

3.3 Comparison

Both methods have some benefits and some drawbacks. The SVD method directly allows for point pairs to be weighted and thus contribute with different degree to the final result. This is handled by the w_n constants in equation (3.8). Methods have been made to estimate these weights based on the data in order to create more robust registration. Although Horn shows that his method can be extended for weighting point pairs, the SVD method seems to be the method of choice for weighted or robust corresponding point registration problems. Another feature of the SVD method is that it easily generalises to N dimensions, while the unit quaternion solution only works in two and three dimensions. The major drawback with the SVD method is that an orthonormal matrix can represent both rotations and reflections, and the method does not guarantee that the result is a rotation only.

3.4 Iterative Closest Point Algorithm

The Iterative closest point algorithm was first introduced by Besl [4], and is a well known algorithm for registration of surface data. In our previous study [3] we have shown that this algorithm is feasible as a basis for a surface based, marker-less registration scheme. The algorithm is very general which makes it an ideal basis for modification. The general ICP algorithm is given in algorithm 1.

The algorithm in algorithm 1 is slightly generalised compared to Besl's original, in particular Besl did not have a FILTER_PAIRS step. In the original article, Besl uses a global search for FIND_CLOSEST_POINT, alternatively sped up using a K-d tree. For CORRESPONDING_POINTS_REGISTRATION he uses Horns quaternion based solution, [10]. Numerous suggestions have been presented to speed up the algorithm, or to make it more robust when meeting outliers and noise, or to adapt it to specific tasks.

Algorithm 1 Baseline ICP

$Transform \leftarrow Initial\_Transform$
$Moving\_data \leftarrow TRANSFORM(Moving\_data, Transform)$
repeat
  for each $point$ **in** $Moving\_data$ **do**
    $closest\_point \leftarrow FIND\_CLOSEST\_POINT(Fixed\_data, point)$
    $Point\_pairs \leftarrow Point\_pairs \cup \{[point, closest\_point]\}$
  end for
  $Point\_pairs \leftarrow FILTER\_PAIRS(Point\_pairs)$
  $Increment \leftarrow CORRESPONDING\_POINTS\_REGISTRATION(Point\_pairs)$
  $Transform \leftarrow Transform * Increment$
  $Moving\_data \leftarrow TRANSFORM(Moving\_data, Increment)$
until (Convergence)
return $Transform$

Some common modifications include:

- Weighting pairs in CORRESPONDING_POINTS_REGISTRATION according to matching features (colour, curvature, normals etc), or weighing pairs based on distance between points to speed up convergence
- Replacing the least mean squares CORRESPONDING_POINTS_REGISTRATION with a least median squares registration, to allow up to 50% outliers [18]
- Replacing the least mean squares CORRESPONDING_POINTS_REGISTRATION with a registration that minimises the mean of some transfer function of the squared distance between the points, to increase robustness.[16],[8]
- Use a projection in FIND_CLOSEST_POINT, to speed up each iteration.
- Use auxiliary information when finding closest point. Examples include luminance [29], colour
- Use a neighbourhood heuristic as FIND_CLOSEST_POINT, to speed up each iteration. [12]

3.5 Multi-resolution Iterative Closest Point Algorithm

One important modification to the original ICP algorithm is to run it in a multi-resolution scheme as suggested by Jost [11]. This is done by first running the algorithm on a small part of the dataset, and using the result as initial transformation for another run with a larger part of the dataset and continue until all the available data is used, as described in algorithm 2. This result is a registration which is more robust in handling local minima,

and that is much faster. The speed gain is caused by the ICP algorithms tendency to give most significant changes in the earliest iterations. The added robustness is caused by the fact that with a smaller dataset the solution space have a lower resolution, which may fail to represent some of the minima.

The following subsampling methods are suggested in the literature:

- Uniform subsampling [28]
- Random subsampling, with different subsampling each iteration. [18]
- Uniform normal distribution. [22]

In addition we suggest subsampling done uniformly according to increasing curvature, as explained in algorithm 3. This will guarantee that points from both smooth areas and areas of high curvature gets included in each subsampled dataset, even with very few points.

Algorithm 2 Multi-Resolution ICP

$Transform \leftarrow Initial\_Transform$
$Num\_Points \leftarrow N$
while $Num\_Points < Size(Moving\_data)$ **do**
  $Sub\_moving\_data \leftarrow SUBSAMPLE(Moving\_data, Num\_Points)$
  $Sub\_fixed\_data \leftarrow SUBSAMPLE(Fixed\_data, Num\_Points)$
  $Transform \leftarrow BASELINE\_ICP(Sub\_moving\_data, Sub\_fixed\_data, Transform)$
  $Num\_Points \leftarrow INCREASE(Num\_Points)$
end while

Jost suggests starting with a low number of points (about fifty) and double the amount for each level. Making the INCREASE function in algorithm 2 a simple duplication. He also shows that when using an acceleration for the FIND_CLOSEST_POINT, such as a Kd-tree search, there is no need to subsample the fixed data.

Algorithm 3 Curvature subsampling

$CURVATURE\_SORT(Moving\_data)$
$Step \leftarrow Moving\_data/Num\_Points$
$i \leftarrow 1$
while $i < Num\_Points$ **do**
  $Sub\_moving\_data[i] \leftarrow Moving\_data[i * step]$
  $i \leftarrow i + 1$
end while
return Sub_moving_data

3.6 Handling Partial Overlap

When imaging with CT or MR scanners, it is usual to scan the minimum area required to get the relevant area well covered. This is because of radiation doses in the CT case, and in the MR case it is because the resolution/accuracy gets reduced when the field of view is large. As a result of this, we will often get a problem when the surface scanned by the optical measurement device covers areas not included in the CT/MR scan. This case is not handled by the ICP algorithm directly. One proposed solution for this kind of problem can be found in [28]. Here Turk uses a modified ICP algorithm to merge range images of the same object captured from different angles, in order to recreate a complete model of the object. This task obviously needs to handle partial overlap. Turks heuristic approach states that after pairs of corresponding points have been found, all pairs where one of the points is on the edge of the the surface should be dropped before doing corresponding points registration. In addition he also drops points that are more than a certain distance apart.

Other solutions have been proposed as well. Masuda proposes to replace the minimum mean square distance registration with a minimum median square distance registration [18]. This allow for up to 50% non-overlapping surfaces. Another solution [19], is to first run a registration, and remove all outliers after the registration and run the registration once more afterwards.

3.7 Geometric Constraint

In order for any surface based registration to work it is necessary that the shapes to be registered have sufficient geometric constraint. For example it is impossible to find the right rotational values for a sphere or a cylinder based on geometry alone, while a cube may work well[1]. Even further, if the registration is to be performed with only a limited portion of the objects surface as moving data, which is the case for our registration using tracking device, the used points should be selected so as to provide maximal geometrical constraint.

Simon[26] uses principal component analysis to derive a measure for the geometric constraint for any given object. Given a function $\mathbf{V}(\mathbf{x_s})$ of a point $\mathbf{x_s}$ on the surface of the object and the normal vector $\mathbf{n}$ of the object in that point as follows:

$$\mathbf{V}(\mathbf{x_s}) = \begin{bmatrix} \mathbf{n} \\ \mathbf{x_s} \times \mathbf{n} \end{bmatrix} \tag{3.11}$$

[1] disreguarding symmetry

he shows that the magnitude of the minimal eigenvalue for the matrix:

$$\sum_{\mathbf{x_s} \in \mathbf{M}} \mathbf{V}(\mathbf{x_S})\mathbf{V^T}(\mathbf{x_s}) \tag{3.12}$$

is a good measure of the geometric constraint for the model. The corresponding eigenvector represent the direction of maximum freedom and is composed as follows:

$$\mathbf{t} = \begin{bmatrix} t_x & t_y & t_z & \omega_x & \omega_y & \omega_z \end{bmatrix}^T \tag{3.13}$$

where $(\omega_x, \omega_y, \omega_z)$ is rotations about the respective axes, and (t_x, t_y, t_z) are translations about the newly rotated axes.

Given the six eigenvalues $\lambda_1 \geq \lambda_2 \geq \lambda_3 \geq \lambda_4 \geq \lambda_5 \geq \lambda_6$ of the matrix in equation (3.12), the noise amplification index(NAI) is defined as:

$$\frac{\lambda_6}{\sqrt{\lambda_1}} \tag{3.14}$$

This is an even better measure than the minimum eigenvalue alone, and will be used in analysis of our results.

Chapter 4

Registration Accuracy

4.1 Metrics

There are several measures available to give the accuracy of a registration. The most common is the Fiducial Registration Error (FRE for short). FRE is defined as some function of the distances between one point and the corresponding point in the other dataset. Usually this is the mean euklidian distance or RMS distance. The FRE value is usually very easy to get from the registration system since most systems work by trying to minimise it. The measure has some serious drawbacks as explained in [7].

A better measure is the target registration error(TRE), which is defined as a function of the distance from one point in moving data after registration to the corresponding point in fixed data. This makes TRE a function of the input space, and thus it can not give a single number for the resulting accuracy. The ideal measure of registration accuracy would be a confidence interval for the TRE throughout the area involved in the surgery. The value of TRE is very hard to estimate in general, even though some special cases are explored. In particular Fitzpatrick presents in [7] some interesting theories on accuracy metrics in a point based registration setting. He uses perturbation theory to explore the relationships between the fiducial location error[1](FLE), FRE and TRE. He shows how the TRE depends on FLE, the number of points, and the point configuration, while the FRE only depends on the FLE and the number of points, but not on the point positions and configuration.

If a ground-truth is known, it is common to give the error as maximal displacement and rotational error. This is also a common way to give accuracy requirements of a specific task. As noted by Simon in [24] this metric is ambiguous and depends on the coordinate system used. He suggest that if this method is to be used, the coordinate system must be defined relative to the task to be solved.

[1]the mean distance between the unknown true positions of the fiducials and the measured positions

In later work Simon[26] proposes the maximum correspondence error (MCE). The MCE is defined as

$$MCE = \max_i ||F_i - M_{err}F_i|| \tag{4.1}$$

where M_{err} is the difference between the ideal transformation, and the actual transformation like this:

$$M_{err} = M_{true}M_{est}^{-1} \tag{4.2}$$

Calculating MCE is only feasible when the true transformation(M_{true}) is known, but Simon shows how an upper bound on MCE can be found from the RMS FRE.

Both [24] and [5] use a screw axis analysis of registration results to analyse the registration results. This method makes it fairly easy to detect the areas of worst error. Simon also reports that visualising the screw axis superimposed on the relevant anatomy is useful when interpreting the registration error.

4.2 Factors

Numerous factors affect the accuracy of the registration. Here are a few:

- Volume data acquisition
- Surface reconstruction/segmentation
- Optical measurements
- Surface reconstruction from optical measurements
- Registration errors
- Anatomical deformations

We will discuss each of these in the following sections.

4.2.1 Volume Data Acquisition

The spacial resolution of the used volume data is an obvious limitation of the representation of the object to register. That is, a volume image with voxel resolution 2 mm x 2 mm x 2 mm can not represent the surface of an object as accurately as a volume image with voxel resolution 0.5 mm x 0.5 mm x 0.5 mm. Consider a diagonal line sampled in these two resolutions, the higher resolution image would be a fine grained staircase

following the line, while the lower resolution image would be a rough staircase, nearly checkerboard patterned. Now consider there was a bump on this line, like a 1 mm radius semicircle. The fine resolution image would represent this to some degree, while the low resolution image might totally miss it, or make it much larger than it actually is, depending on where in the sampling it hits.

The contrast resolution(number of available gray levels) also have an affect on registration accuracy. More gray levels will allow for more accurate positioning of the surface. Higher contrast resolution will also allow for better separation of the wanted object from neighbouring object with similar properties.

Lastly acquisition errors, like mechanical inaccuracy and different artefacts may result in reduced accuracy. These are however not discussed in this work, more than noting their existence.

4.2.2 Volume Data Surface Reconstruction/Segmentation

As noted in [24] little have been published on validation of surface model geometric accuracy. This is generally speaking a very difficult thing to do, and it is linked to the fundamental difficulty of segmentation in general. For validation of a image segmentation, a ground truth is needed, but if a ground truth is readily available the segmentation is not needed in the first place. There are two general ways suggested in the literature: Either compare the methods output to manual segmentation done by and expert, or run the method on scans of an object for which a good representation already exist. The last method usually requires precise manufacturing of an object from a model specification. The former method is very time consuming, and expensive, since the competence needed for good manual segmentation is highly priced. In order to say something general about the segmentation performance the procedure must be run on, and evaluated for several different datasets, to make sure it doesn't just work for one given set.

4.2.3 Shape Measurement Device

The optical shape measurement device used is specified to have an point accuracy of 0.1 mm. A possible source of error here is when unwanted surfaces get included in the scan. These might include hair, cloths, the operating table etc.

4.2.4 Surface Reconstruction from Optical Measures

A special spline based algorithm is used to create a smooth surface from the points of the shape measuring device. This algorithm is also responsible for removing unwanted surfaces from the point cloud. Possible causes of errors from this step include: Incorrect

trimming and moved surface errors. The spline surface can, due to the nature of splines, be evaluated for any (x, y) to get the corresponding z. This, however, is not wanted since the surface isn't really available for all (x, y). Therefore the spline surface is trimmed, to remove the parts with little correspondence in the shape measurement point cloud. Errors in this trimming process can cause the surface to be slightly extrapolated in some areas, and trimmed too much in others. The former error can introduce registration errors (most noticeably rotational errors, when the extrapolation is asymmetric), while the latter only reduce the available information needed to do the registration, and therefore also the total possible accuracy. This we call trimming errors. The moved surface errors is caused by the nature of splines. In areas with high curvature the spline surface will lie fully within the control points(from the shape measurement device) and thus even further away from the real surface than the inaccuracy of the shape measurement device.

4.2.5 Registration Errors

Registration errors are a common name for all errors caused by the registration system itself. This includes when the algorithm gets stuck in a non-global minimum, and when higher functions of the registration, like detection of overlap, fails. When registration fails it is often a real error, more than a source of inaccuracy. However noisy data, or data with poor geometric constraints, can result in additional local minima near the global minima, creating good, but not perfect results.

4.2.6 Tracking Device

Errors of the tracking device is directly contributing to the total registration error. Even if all other parts of the system were completely perfect, the tool position on the navigation computer could not be more precise than the accuracy of the tracking system. The passive Polaris system used is specified to have a RMS error in positioning of 0.35 mm. Furthermore this will affect the registration accuracy as well, when using the tracking device registration. For the tracking device registration there is another source of error that should be considered here, namely the operator. If the operator does not manage to keep the tip of the tracking probe in contact with the patient skin at all times during position capture, incorrect positions will appear in the resulting data. This may happen for a number of reasons including, but not limited to:

- The probe gets stuck and "jumps" free again. This was in particular a problem with the rubber skin of the phantom used in our tests.

- Hair or other feature touches the probe further up from the tip, and pulls the tip of the probe away from the surface.

Both of these can be improved by building better tracking probes for the task, improve training and build better procedures for the data capture.

Chapter 5

Segmentation Methods

In previous work we used a method combining thresholding and operations from mathematical morphology to do the surface extraction from volume data. This method, even though it worked well enough for our tests, has a number of drawbacks. In this work we have tried to overcome these using modern level set techniques.

5.1 Level Set Introduction

Level set methods are one of the latest achievements in image manipulation, and have proven effective in numerous applications. The level set methods build on the "active contours" idiom, but implements it with a different mathematical formalism. It is known that a curve or surface can be viewed as the level set[1] of a one dimension higher function. In level set image segmentation[17] one starts with a contour, and then constructs a higher dimensional implicit function that has this contour as it's zero level set. This higher level function is then used as a first solution to a differential equation, and it is iteratively refined. When the refinement stops, due to convergence or timeout, the zero level set of the resulting higher dimensional function is found, and this level set is the result of the segmentation procedure. Constructing different differential equations makes it possible to quickly implement different segmentation algorithms, with different properties. The different parts of the differential equation are called "energy terms" and the solver iteratively tries to minimise the energy of the resulting curve. Usual energy terms include:

- An upwind term that expands the curve through regions of low gradient, but that stops near high gradients. Also called and advection term. This term allows the segmentation to work even with a very rough initial contour.

[1] also known as level surface or level curve i 3 and 2 dimensions

- A curvature dependant term, that minimises curvature. This term reduces the effect of noise in the image, and allows the curve to close gaps, when edge segments fail to completely enclose the object.
- A term that attract the curve to high gradients.

5.1.1 Fast Marching Method

When the differential equation has a simple enough form, the solver may be simplified quite a bit. In particular, when using only the upwind term the normal solver may be replaced by an algorithm called the fast marching method. In the fast marching level set solver, the working matrix does not contain the current value of the higher dimensional function at the different points, but rather contains the time in which the zero level set crossed that area. This buffer is initialised so that points inside the initial contour are zero, and points outside are $+\infty$. In addition all points inside the initial contour, without neighbours outside, are put in a list of visited points. Then one repeatedly selects the non-visited point with lowest value, calculate the speed at this point, multiply it with the time step, and add the value of the current point. This value is assigned to all non-visited neighbours whose value is not already lower than this. Then the point is flagged as visited and the next point is selected. This is repeated until all points have been visited, or until the lowest unvisited points value is larger than a given threshold.

Now the different level sets of this matrix will give the solution at a given time. Taking the level set at a very high time will give the curve when the motion stopped, which is equivalent to the energy minimum.

The algorithm, following [23] becomes algorithm 4. When using a heap structure

Algorithm 4 Fast Marching Level Set

$T[x] \leftarrow 0 | x \in INITIAL$
$KNOWN \leftarrow \{x | x \in INITIAL, \forall y \in NEIGHBOUR(x) y \in INITIAL\}$
$TRIAL \leftarrow \{x | x \in INITIAL, x \notin KNOWN\}$
repeat
  $x \leftarrow x' | x' \in TRIAL, \forall_{y \in TRIAL} T[x'] \leq T[y]$
  $TRIAL \leftarrow TRIAL \setminus \{x\}$
  $KNOWN \leftarrow KNOWN \cup x$
  for each y **in** $NEIGHBOUR(x) \cap \overline{KNOWN}$ **do**
    $TRIAL \leftarrow TRIAL \cup \{y\}$
    $T[y] \leftarrow \min(T[y], T[x] + Speed(x) * TIMESTEP)$
  end for
until $TRIAL = \emptyset$

for the trial list, the insertion, removal and minimum search in this algorithm can be

done in $O(logN)$. This results in a run time of $O(N^3logN)$ for the complete algorithm for a NxNxN volume.

The good thing about the fast marching method, is that it allow the contour to evolve fairly long, fairly fast. Thus smaller and less accurate initial curves can be used. For instance one could start with a single point known to be inside the desired structure and evolve this point using fast marching methods until that converges. This will give a contour that is close to the desired objects real contour, and can be used as input in the heavier full level set methods.

5.2 Anisotropic Diffusion

The level set segmentation methods use a local gradient operator to detect edges. It is a known fact that local gradient operators are very sensitive to noise. Noise can easily be suppressed with a blur operation, like convolving with a gaussian kernel, but this diffuses the edges, which can cause the algorithm to expand through the edge, or just cause the position of the edge to be a bit wrong. One solution, suggested by Perona and Malik [21], is the anisotropic diffusion.

This method is based on the observation that blurring an image with a gaussian kernel is equivalent with the solution of the heat equation at a given time depending on the size of the gaussian kernel, where the image intensities act as initial temperatures. Changing the conductivity term of the heat equation from a constant value (isotropic) to a value that changes throughout the image (anisotropic) allows for similar operations but with different properties.

The anisotropic heat equation is as follows:

$$\frac{\delta I}{\delta t} = c(x, y, z, t)\nabla^2 I + \nabla c \cdot \nabla I \tag{5.1}$$

For constant conductivity this reduces to the classic heat equation:

$$\frac{\delta I}{\delta t} = c\nabla^2 I \tag{5.2}$$

Making the conductivity change dependant on the local brightness gradient, such that lower gradients give better conductance, and higher gradients have lower conductivity will give a smoothing effect that preserves edges. The function recommended by Perona and Malik is:

$$c(x, y, z, t) = g(||\nabla I(x, y, z, t)||) \qquad g(\nabla I) = e^{-(||\nabla I||/K)^2} \tag{5.3}$$

Solving this equation gives a function $I(x, y, z, t)$ with the properties that $I(x, y, z, 0)$ is the initial image, and evaluations of the function at values $t > 0$ gives smoothed versions where the image is more smoothed for a higher t.

The equation is usually solved using finite forward differences, and only solved to the time level wanted.

5.3 Marching Cubes

The marching cubes algorithm is an algorithm to extract isosurfaces from volume data. It was invented by Lorensen and Cline [15] to help visualisation of medical volume images. Although the algorithms original intent was in visualisation, it is generally useful in extracting polygonal models from volume data. This has uses in surface based registration, both as a stand alone segmentation method, and as a means to extract the result of methods that does volume segmentation entirely in the volume data domain, like the various level set methods described in section 5.1.

The marching cubes algorithm consider 2x2x2 voxel sub-volumes, called a *cube*, of the original input volume. It flags each of the voxels as either *inside* or *outside* depending on whether the value of that voxel is higher or lower than the wanted isosurface. Noting that the resulting polygon model must separate each inside point from each outside point gives 2^8 topologically different ways to create polygon models for such a cube. Taking into account rotational symmetry, and the observation that the model must be the same if all inside and outside points are swapped, the number of basic cases is reduced to 14. This allow for a quick table lookup implementation to find the number and topology of the triangles to create. The location of the triangles vertices are then calculated using linear interpolation between the position of the inside and outside voxels, taking into account the voxel sizes. The location of the output vertexes are therefore given in floating point mm position along the three axes, independent of input volume resolution and voxel sizes.

When the triangles for one *cube* is added, the algorithm moves on to consider the next cube, in scan-line order, until the entire volume is processed. This means that the algorithm needs only have two slices of the volume in memory at the same time.

Alternatively the algorithm can calculate normals from the image gradients. These normals can be used in shading during visualisation. This extension increases the memory need to four slices.

An interesting property of this algorithm is that all surfaces it produces are closed where not cut by the volume data boundary. Thus all edges of the surface will be located on the surface of the outputs bounding box.

Chapter 6

Implementation

This chapter discusses implementation details for the test system. The selected algorithms and methods are described and relevant details on how they are implemented are described.

6.1 ITK, VTK and CustusX

The implementation relies heavily on the open source libraries ITK and VTK for image processing and visualisation, as well as geometric support code.

ITK is short for The Insight Toolkit, and it "is an open-source software toolkit for performing registration and segmentation."[13]. ITK contains all the building blocks used in the segmentation part of this work.

VTK is short for The Visualization Toolkit. It is an open-source toolkit for image processing and visualisation. It contains all the necessary building blocks for an efficient implementation of the ICP algorithm.

CustusX is SINTEF MedTech's visualisation and navigation application. It is used in the experiments, and it is used to capture tracking device positions, and finding landmarks in the volume data.

6.2 Segmentation

The goals for the segmentation is to extract the following:

- An accurate surface
- No inner surfaces
- No false surfaces

Time step	0.625
Conductance parameter	9
Iterations	5

Table 6.1: Parameters for smoothing operation

An inaccurate surface will negatively affect the registration accuracy. Inner surfaces may appear if areas inside the body has similar properties in the given image modality as the outside, or because of ear canals and nasal pits or similar that are considered part of the surface. These will not show up on outer surface scans, and will negatively impact the registration. False surfaces usually is the result of noise, or external objects that show up in the images. Typically this is the gantry in CT scans. These surfaces may cause the registration to fail horribly.

The following steps were chosen as means to fulfil these goals:

- Resample to uniform voxel size
- Smooth using edge preserving smoothing
- Rough segmentation using fast marching level set methods
- Segmentation refinement using laplacian level sets
- Surface extraction using marching cubes
- Selecting correct surface

The level set solver system in ITK does not support volume images with inhomogeneous voxel dimensions. Therefor the first step is to resample the volume image in such a way that the voxels becomes cubes, with all sides equal in length to the smallest side length in the input image. Usually the input volume image has equal voxel size along the x and y axes, while the voxel is a little bit larger in the z direction. The resampling then just increases the amount of slices in the volume image.

The level set approach uses edge information. This calls for a smoothing operator to reduce the sensitivity to noise. The chosen operator is ITK's `CurvatureAnisotropicDiffusion`. This algorithm is a slight modification to the standard anisotropic diffusion equation in order to prevent negative diffusion. This equation is solved using level set methods. The parameters used are listed in table 6.1.

The fast marching segmentation step starts of with an initial contour consisting of a single voxel set in all eight corners of the volume. It uses the sigmoid of the reciprocal of the gradient magnitude as the speed function, like this:

$$S(x,y,z) = \left(1 + e^{-\frac{R(x,y,z)-\beta}{\alpha}}\right)^{-1} \quad R(x,y,z) = \frac{1}{N(1 + ||\Delta I(x,y,z)||)} \tag{6.1}$$

Modality	α	β
MR T1	0.1	0.5
MR T2	0.1	0.5
CT	0.001	0.012

Table 6.2: Parameters for sigmoid function

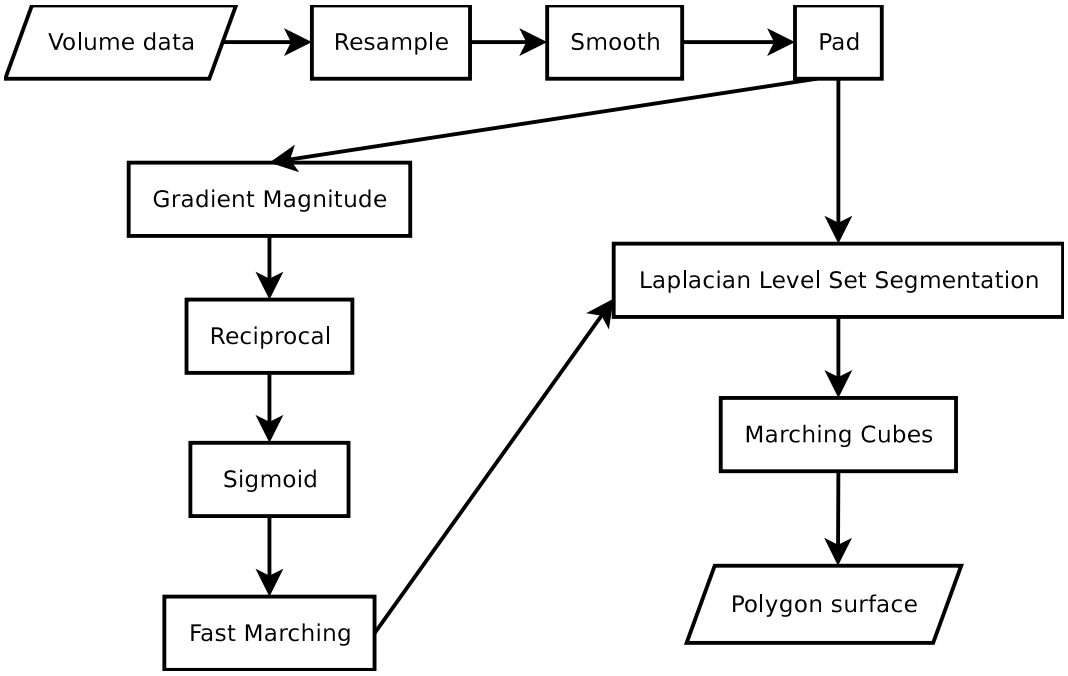

Figure 6.1: Data flow in MR segmentation

. The sigmoid allows to separate strong edges from weak ones. The β parameter states where the separation between strong end weak edges are. The α parameter selects how hard to separate them. Ideally these two parameters should be the only parameters needing change between different modalities. The parameters used are shown in table 6.2.

Seeding surface outside the patient and growing inwards ensures that no inner surfaces of the patient that is not connected to the outside is included in the result, as well as making the segmentaton easier since the outside is more homogeneous to progress the surfaces through than the inside.

The Segmentation refinement step uses ITK's Laplacian level set segmentation algorithm, because of it's few free parameters, and it's claim to be a good method for refining existing segmentations. This method is essentially a ordinary level set method that contains two energy terms. One that attracts the contour to zero crossings of the laplacian of the image, and one that minimises curvature. The parameters in this step is given in section 6.2

Curvature scaling	40
Propagation scaling	1
Minimum RMS change	0.001
Maximum iterations	20

Table 6.3: Parameters for laplacian level set segmentation

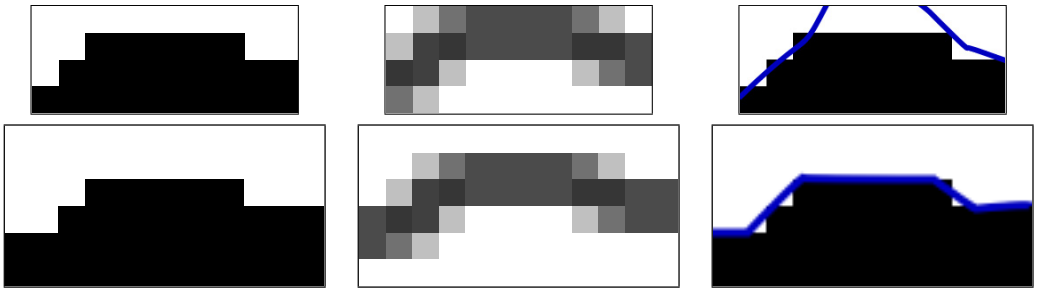

Figure 6.2: Examples of problem near data boundary. Upper row shows part of image, it's gradient magnitude and the resulting surface. Second row show how padding the volume allow the surface to close the object.

The curvature term in the level set refinement step allows to limit how long into ear and nose the surface will progress. There is however a trade-off between limiting the surfaces progression and the total accuracy. Too high curvature scaling will limit how well the surface may represent features of the surface, and thus limit the total accuracy.

A problem arises when parts of the surface to be extracted appear close to the data boundaries. When calculating gradients, the `GradientMagnintudeImageFilter` of ITK uses Neumann boundary conditions to select values outside the image in order to calculate a gradient magnitude image of the same size as the input image. As can be seen from figure 6.2 this causes the outermost voxels of the output to get a large gradient magnitude. This in turn stops the level set surfaces from closing through that region, even though it is clear from the input that there is a surface there. This problem can be solved by padding

The final step is to select the right surface to use. This is done my selecting the connected surface that contains middle point of the volume. An overview of the data flow in the complete procedure is described in figure 6.1.

6.3 Registration

The registration implementation is based on the ICP algorithm, and the modifications stated in chapter 3. In particular we use a multi resolution approach starting with 50 points, and increasing the amount with N*2+10 for each run. The subsampling is done uniformly according to increasing curvature. This allow points from different features

to be fairly well represented.

The implementation is based on the `vtkIterativeClosestPointTransform` class from the VTK library. This is a fairly straight forward implementation of the baseline ICP algorithm. It uses Horn's quaternion solution, implemented in the `vtkLandmarkTransform` class, as corresponding points registration, and a search structure where points and surfaces are split into buckets based on a regular division of the space (`vtkCellLocator`), to find the closest point. The original implementation is modified in a number of ways: It now takes an initial transform. This allow for modular initialisation of the algorithm, and allows for multi-resolution operation, by setting the object's initial transform to the object itself after running once, and then rerun with different parameters. Secondly the class is modified to use the curvature based subsampling when curvatures are available. Thirdly the default method of finding closest point is replaced with a Kd-tree approach using the `vtkKdTree` class. The vertexes of the polygonal model is used to build the tree, after the closest vertex is found, each of the polygons this vertex is a part of is investigated, and the closest location to the given point on each of the polygons is computed. The closest of these are selected as the closest point. Since our surfaces have fairly regular polygon size, and this size is always small compared to the bend in the surface, we believe this approximation will find the true closest point with a very high probability.

Turk's method for handling partial overlap is implemented very simply by checking if the fixed point of each point pair is located on the bounding box of the fixed data. This is equivalent with checking if the point is on the surface edge, because of a property of the marching cubes algorithm (see section 5.3). Rather than using a fixed distance threshold like Turk suggests, we automatically estimate the threshold value using an automatic thresholding algorithm [27]. We call this distance threshold the *filter*, because it mainly removes areas where the surfaces don't match (presumably due to noise), as opposed to areas where one of the surfaces is simply missing. The filter needs the registration to be nearly finished in order to properly separate the noise. The filter is therefore only used in the final two pyramid levels.

The ICP algorithm is, as stated in chapter 3 a local search method. In order to properly find a global registration a initial transform, capable of transforming the moving data into the "catch basin" of the ICP algorithm needs to be found. How this is done is handled independently for registration with the shape measurement device, and registration using tracking device in the following sections.

6.3.1 Registration by Shape Measurement

In order to archive a proper initialisation for registration with the shape measurement device, knowledge of the medical imaging devices, and the optical shape measurement device is used.

DICOM

All medical imaging devices follow a standard called DICOM (Digital Imaging and COmmunications in Medicine). The DICOM standard defines a patient-oriented coordinate system as the reference coordinate system[1], RCS for short. The coordinate system is defined such that the x-axis increases towards the patients left side. The y-axis increases towards the patients back and the z-axis increases towards the patients head. The standard doesn't enforce the images to be sampled in this coordinate system, but rather includes a tag, "Image Orientation (Patient)", that holds necessary information to do the transform. This tag consists of six values. The first three are the cosines of the angles between the first row of pixels and the three coordinate axes. The next three values are the same, but for the first column of pixels. The cosine vectors are specified to be orthogonal and normalised, and the RCS is specified to be a right-hand coordinate system, so the z-axis cosines can be found by taking the cross product of the row cosines and column cosines. Resulting in the following transformation from voxel coordinates to RCS coordinates.

$$\begin{bmatrix} x_r \\ y_r \\ z_r \\ 1 \end{bmatrix} = \mathbf{R}_{fr} \begin{bmatrix} x_v \\ y_v \\ z_v \\ 1 \end{bmatrix} = \begin{bmatrix} X_x & Y_x & Z_x & S_x \\ X_y & Y_y & Z_y & S_y \\ X_z & Y_z & Z_z & S_z \\ 0 & 0 & 0 & 1 \end{bmatrix} \begin{bmatrix} x_v \\ y_v \\ z_v \\ 1 \end{bmatrix} \tag{6.2}$$

Where X_i are the row cosines, and Y_i are the column cosines, Z_i is their cross-product. S_i is the image origin defined by the image position tag in the dicom file. This equation is simplified by assuming that the voxel size is 1 mm x 1 mm x 1 mm, which is a safe assumption, since the voxel sizes have already been taken into account when extracting the polygonal surface from the volume data.

Shape Measurement Device

The shape measurement device returns samples in a coordinate system such that, assuming the patient is lying on his back, the x-axis increases towards the patients left side, the y-axis increases towards the patients feet, and the z-axis increases towards the patients front. When this assumption is correct, the transformation needed to take the

coordinates of the shape measurement device into the RCS will be as follows.

$$\begin{bmatrix} x_r \\ y_r \\ z_r \\ 1 \end{bmatrix} = \mathbf{R}_{mr} \begin{bmatrix} x_s \\ y_s \\ z_s \\ 1 \end{bmatrix} = \begin{bmatrix} -1 & 0 & 0 & 0 \\ 0 & 0 & 1 & 0 \\ 0 & 1 & 0 & 0 \\ 0 & 0 & 0 & 1 \end{bmatrix} \begin{bmatrix} x_s \\ y_s \\ z_s \\ 1 \end{bmatrix} \tag{6.3}$$

If another patient position is required the matrix $\mathbf{R}_{sr}$ must be given. This could be done as part of the surgery planning, or it could be done quickly by sampling the directional position of the tracking device when holding it aligned with the patient.

Complete Initial Transform

The complete initial transform from the shape measurement coordinate system to the coordinate system defined by the volume image is as follows: first translate $\mathbf{M}$ so that it's mass-centre is in the origin:

$$\mathbf{T}_{co} = \begin{bmatrix} 1 & 0 & 0 & -\widetilde{M_x} \\ 0 & 1 & 0 & -\widetilde{M_y} \\ 0 & 0 & 1 & -\widetilde{M_z} \\ 0 & 0 & 0 & 1 \end{bmatrix} \tag{6.4}$$

next, convert from the shape measurement devices coordinate system to the RCS, using the $\mathbf{R}_{sr}$ matrix from equation (6.3).

Then apply the inverse of the conversion from the volume coordinate system to the RCS, by inverting $\mathbf{R}_{fr}$ from equation (6.2).

$$\mathbf{R}_{rf} = \mathbf{R}_{fr}^{-1} \tag{6.5}$$

Then match the body centre of $\mathbf{M}$ and $\mathbf{F}$

$$\mathbf{T}_{of} = \begin{bmatrix} 1 & 0 & 0 & \widetilde{F_x} \\ 0 & 1 & 0 & \widetilde{F_y} \\ 0 & 0 & 1 & \widetilde{F_z} \\ 0 & 0 & 0 & 1 \end{bmatrix} \tag{6.6}$$

Finally, we note that $\mathbf{F}$ is a closed surface, while $\mathbf{M}$ usually is only a piece of this surface. If these are left with matching body centre then $\mathbf{F}$ could converge to any part of $\mathbf{M}$. We know that the inside of $\mathbf{F}$ is located at lower z-values, while the outside is at higher values. We therefor want to translate the moving data, so that it extreme point along the z-axis matches the fixed data's extreme point along the rotated version of the

z-axis. The extreme point along any given vector can easily be found by finding the maximal dot product between the vertices of the dataset and the vector. Starting with a unit vector $\mathbf{v}$ along the z-axis, in homogeneous coordinates:

$$\mathbf{v} = \begin{bmatrix} 0 \\ 0 \\ 1 \\ 0 \end{bmatrix}$$

This vector is rotated into the fixed data's coordinate system:

$$\mathbf{v}' = \mathbf{R}_{rf}\mathbf{R}_{mr}\mathbf{v}$$

The extreme points along the vector in the moving data, and the rotated version in the fixed data is found. Note that when $\mathbf{v}$ and $\mathbf{v}'$ are axis aligned the extreme values can be found quickly from the data's bounding box.

$$\mathbf{f}_{max} = \mathbf{v}' \cdot \max_{u \in \mathbf{F}} \{\mathbf{u} \cdot \mathbf{v}'\}$$

$$\mathbf{m}_{max} = \mathbf{v}' \cdot \max_{u \in \mathbf{M}} \{\mathbf{u} \cdot \mathbf{v}\}$$

The final translation then becomes:

$$\mathbf{t} = -(\mathbf{m}_{max} - \tilde{M} \cdot \mathbf{v}' \cdot \mathbf{v}') + (\mathbf{f}_{max} - \tilde{F} \cdot \mathbf{v}' \cdot \mathbf{v}')$$

$$\mathbf{T}_{max} = \begin{bmatrix} 1 & 0 & 0 & \mathbf{t}_x \\ 0 & 1 & 0 & \mathbf{t}_y \\ 0 & 0 & 1 & \mathbf{t}_z \\ 0 & 0 & 0 & 1 \end{bmatrix} \tag{6.7}$$

Combining all these transformations using matrix concatenation yields the complete transformation:

$$\mathbf{M}_{init} = \mathbf{T}_{max}\mathbf{T}_{fc}\mathbf{R}_{rv}\mathbf{R}_{sr}\mathbf{T}_{co} \tag{6.8}$$

6.3.2 Registration Using Tracking Device

The tracking device surface is created by moving the tracking device along the patients skin, and storing it's position at regular intervals. For our tests we have used four samples per second. The result is a partial representation of the patients outer surface based on a limited amount of data points, typically 100–200.

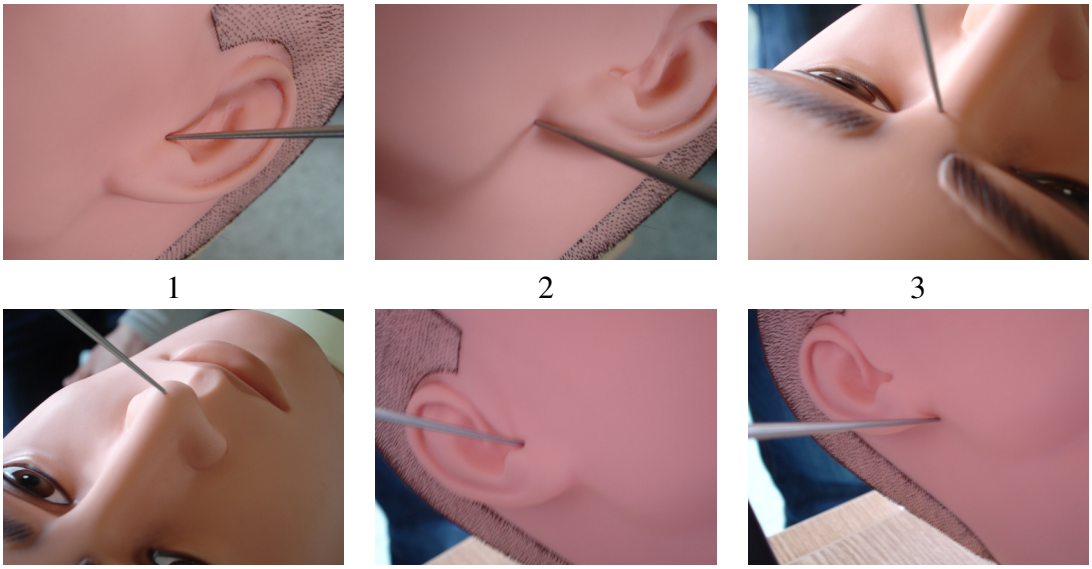

Figure 6.3: Landmarks used for registration

The resulting surface is much smaller, and with much less geometric constraint than the surfaces from the shape measurement device. Because of this a registration based on these surfaces alone will have much smaller catch basin. A more accurate initial transformation is therefore needed. A landmark based registration is selected for the task, since it allows for fairly high accuracy without the need for markers. The surface based registration will act as a refinement for the landmark registration. Two landmarks in each ear, and two on the nose were used. When the patient were lying on the side, the points in the bottom ear were dropped. The precise landmarks used are shown in figure 6.3.

By visualising the fixed surface to the person gathering the surface with the tracking device, we can ensure that no data is collected that does not overlap. This allow for disabling the partial overlap heuristics, and thus makes the algorithm a bit simpler.

Chapter 7

Results

We will present results from three different datasets, run through both the presented registration methods. The datasets are head scans from a phantom and two volunteers. The phantom is scanned with CT, and the volunteers are scanned with MR. For each of the datasets both registration methods are tested in one or more positions. For each of the positions three different patterns are used to gather data for the tracker based method. All registrations are done twice to ensure reproducablity. A summary of the results are shown in table 7.1.

7.1 Segmentation

The segmentation results are presented as selected slices from the volume data, that are upsampled without interpolation, and then overlaid with the 2D polygon resulting from cutting the 3D polygon model with a plane. This allow for accurate visual inspection of the result. We have due to resource limitations not done extensive tests, nor done comparisons with manual segmentation. For each dataset four slices are given. For each slice the direction and location as well as window/level(W/L) settings are given. The resulting surface, cut through the middle of each shown slice is shown in red. Where the angle between the surface and the shown slice is low the surface cut through the top and bottom of the slice is shown in green and pink.

Dataset	Modality	Shape Measurement Positions	Tracker Positions	Total Number of Registrations
Volunteer 1	MR T2	3	1	12
Volunteer 2	MR T1	3	1	12
Phantom	CT	5	3	28

Table 7.1: Overview of results

7.1.1 Volunteer 1

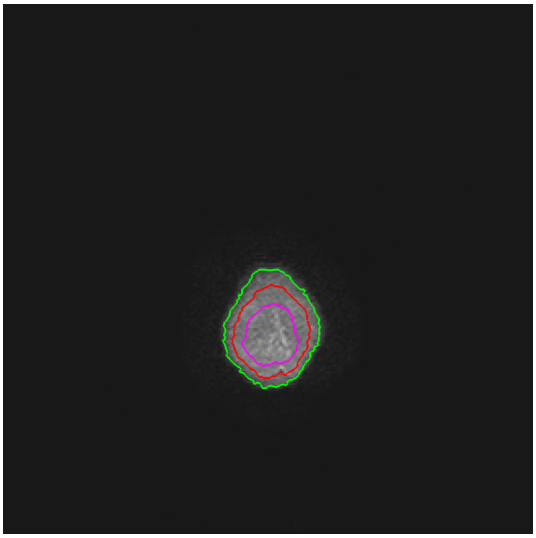

Axial slice 114/120.

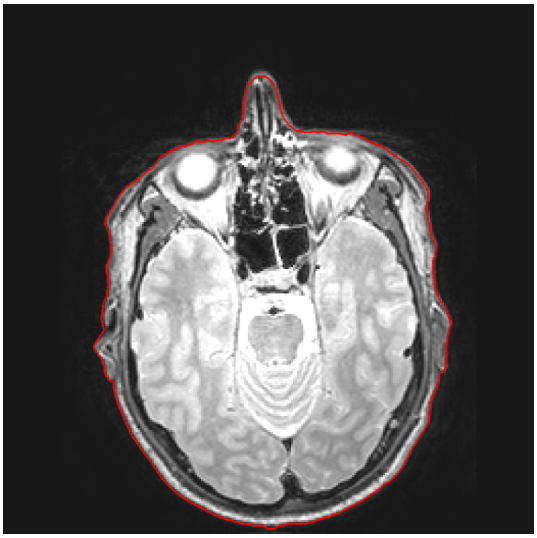

Axial slice 44/120.

Coronal slice 94/256.

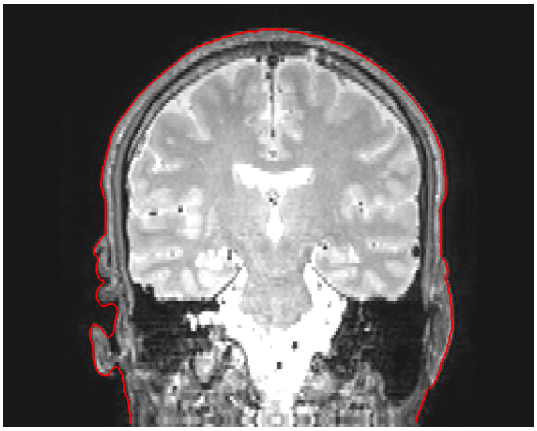

Sagittal slice 96/256.

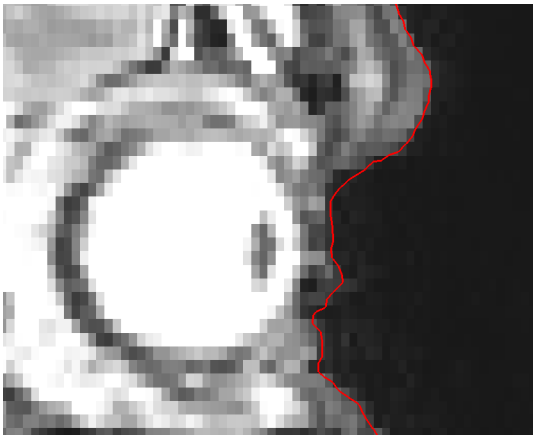

Zoom in on the eye in the above picture

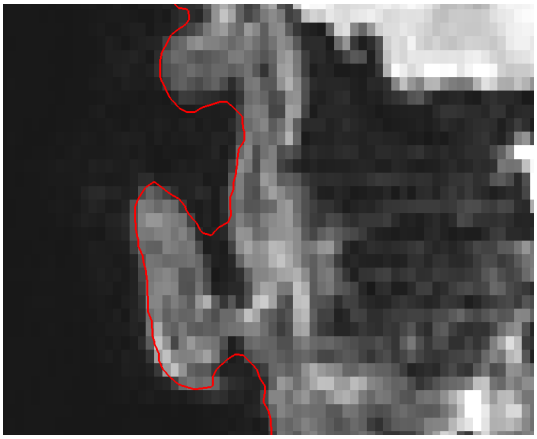

Zoom in on the ear in the above picture

Figure 7.1: Segmentation results for volunteer 1. Window/level: 620/250

7.1.2 Volunteer 2

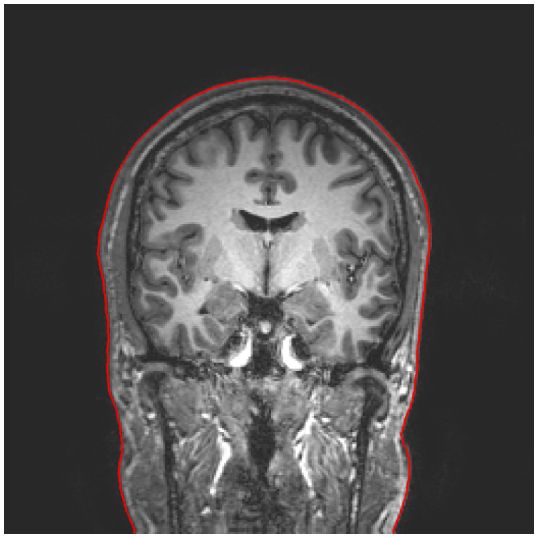

Sagittal slice 90/255

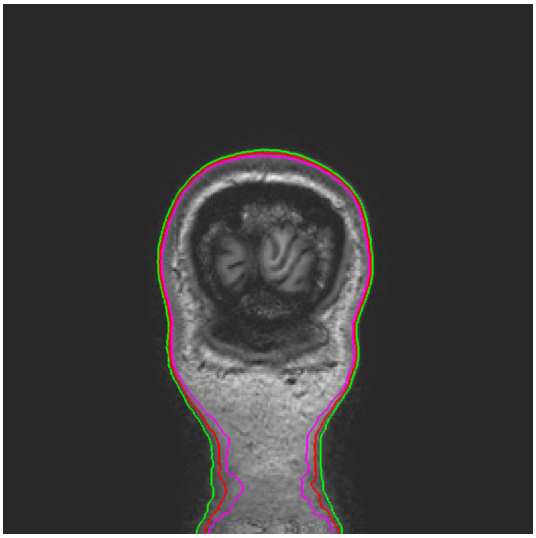

Sagittal slice 167/255

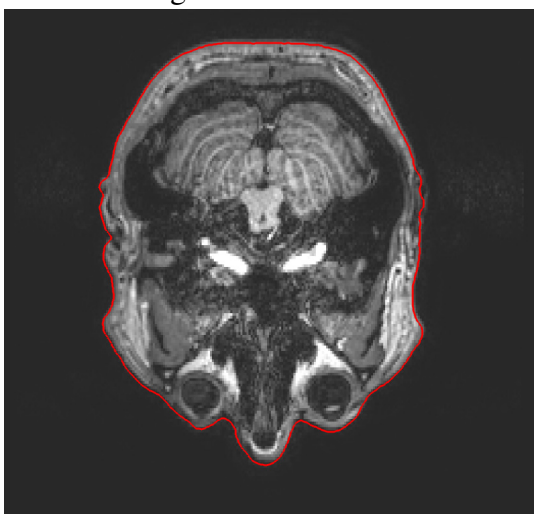

Axial slice 84/182

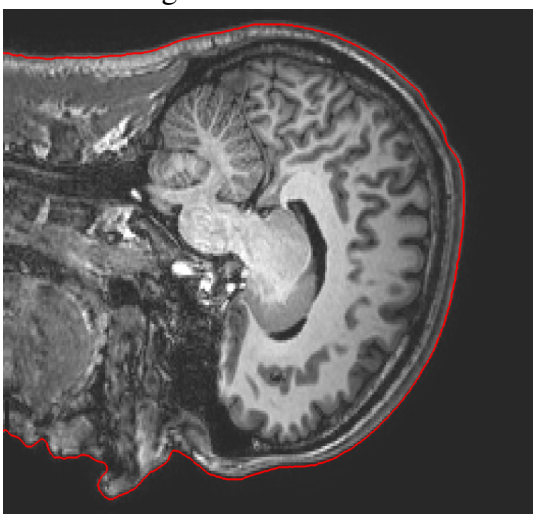

Coronal slice 118/255

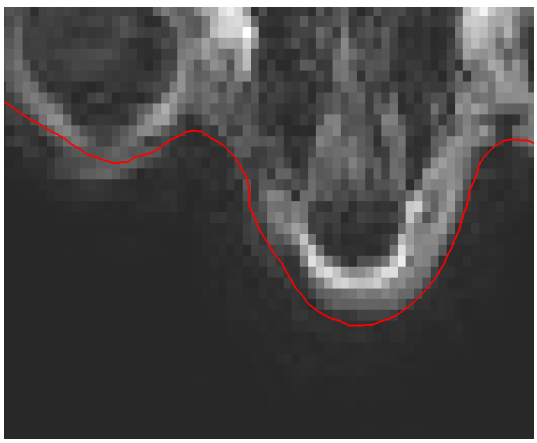

Zoom in on left eye and nose in above picture

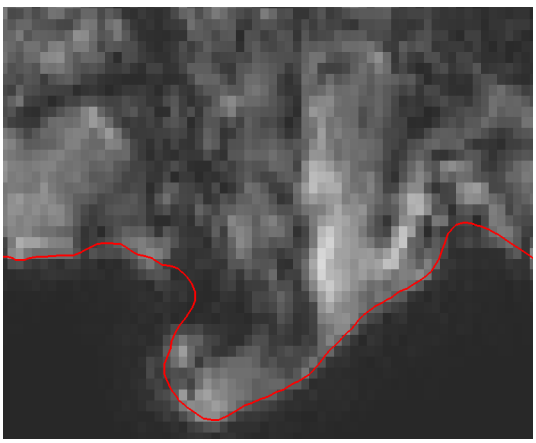

Zoom in on nose in above picture

Figure 7.2: Segmentation results for volunteer 2. Window/level: 500/170

7.1.3 Phantom

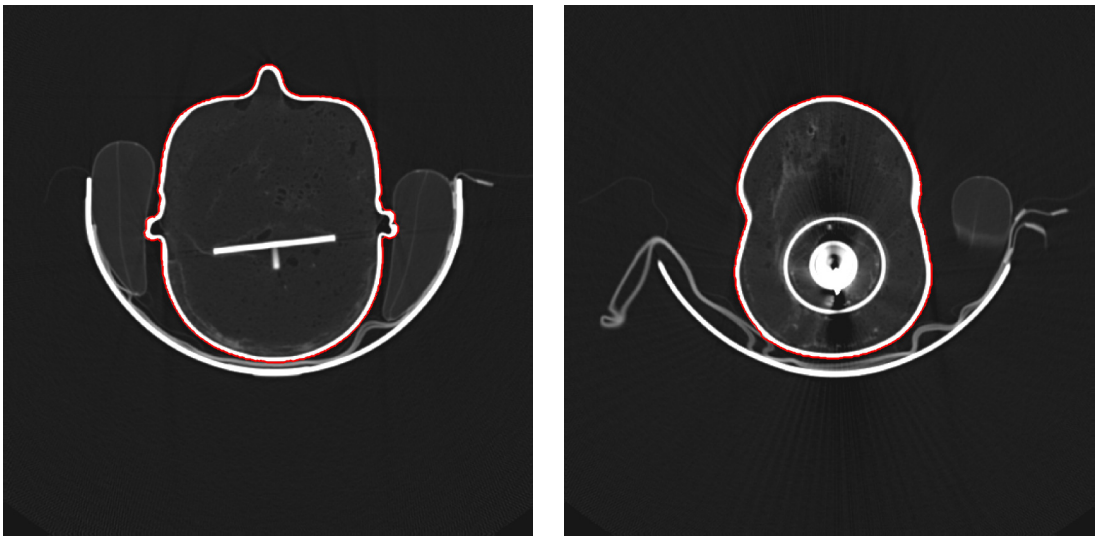

Axial slice 121/255 | Axial slice 56/255

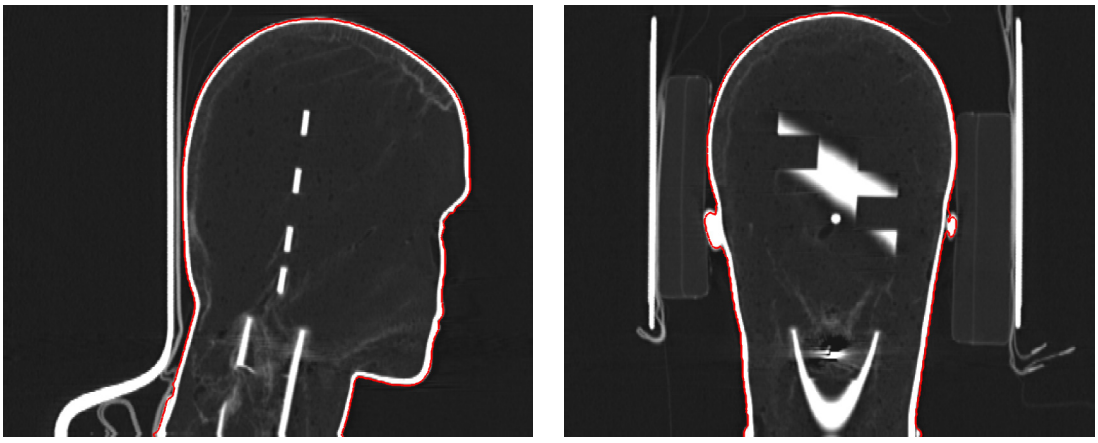

Coronal slice 224/512 | Sagittal slice 290/512

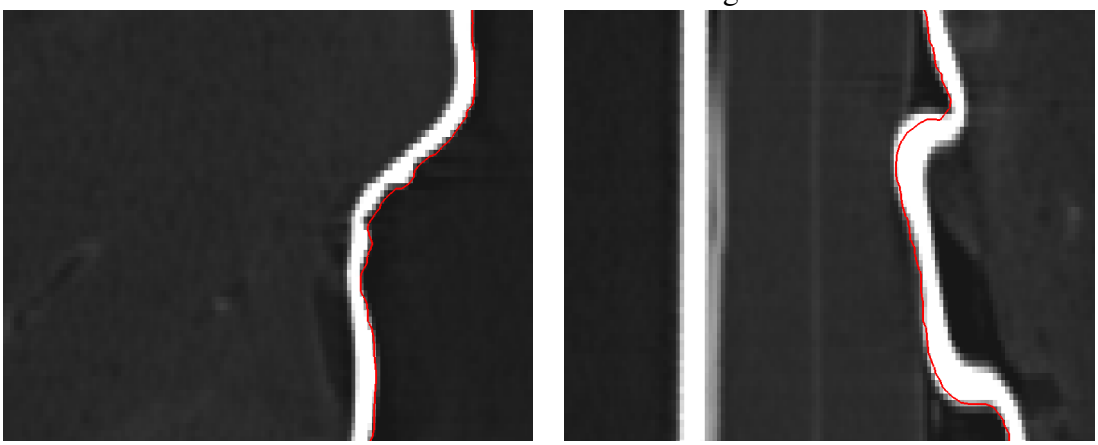

Zoom in on eye in above picture | Zoom in on left ear in above picture

Figure 7.3: Segmentation results for the phantom. Window/level: 880/360

7.2 Registration Using Shape Measurement

For the shape measurement registration we will present the resulting FRE, the determined overlap, the NAI and a series of images suitable for visual inspection of the registration result. In addition the computation time on a AMD Athlon XP 2200+(1800MHz) CPU is given. The NAI is calculated by using the vertices of the moving data and the surface normal of the fixed data in the corresponding closest point. All NAI values are multiplied by 1000 for readability. For each dataset and position combination, two lines are given corresponding to the two different scans. Each line consists of three images. The first is the surface scan colour coded with the local distance from the fixed surface after registration. The second surface shows what the algorithm considered overlapping areas with blue and non-overlapping areas with magenta, and the third show the fixed and the moving surface rendered together to show how they align. Five positions were used: Front, left, right, back and sitting. The front position is the patient lying on his back face up. This is believed to provide the most geometric constraint and the least noise, while being least clinically relevant. In real world surgery the patient is either lying on the left or right side, sitting halfway upright or lying face down. The sitting and back(face down) positions were not used for the two healthy volunteers because of hair related problems. Initial rotation matrices were entered manually with front position as explained in 6.3.1. An additional 45 degrees rotation was added for the left and right positions for the volunteers, and 90 degrees for the phantom. The normal front matrix was used for the sitting position, and an additional 180 degrees rotation were used for the back position.

7.2.1 Volunteer 1

Take	Mean distance	Overlap	NAI	Time
Front 1	0.54 mm	59.2%	1.99	51s
Front 2	0.98 mm	75.8%	2.53	65s
Left 1	1.83 mm	56.2%	0.83	198s
Left 2	1.58 mm	56.3%	0.78	131s
Right 1	1.01 mm	48.9%	1.93	93s
Right 2	1.32 mm	58.9%	2.06	229s

Table 7.2: Shape measurement registration results for volunteer 1

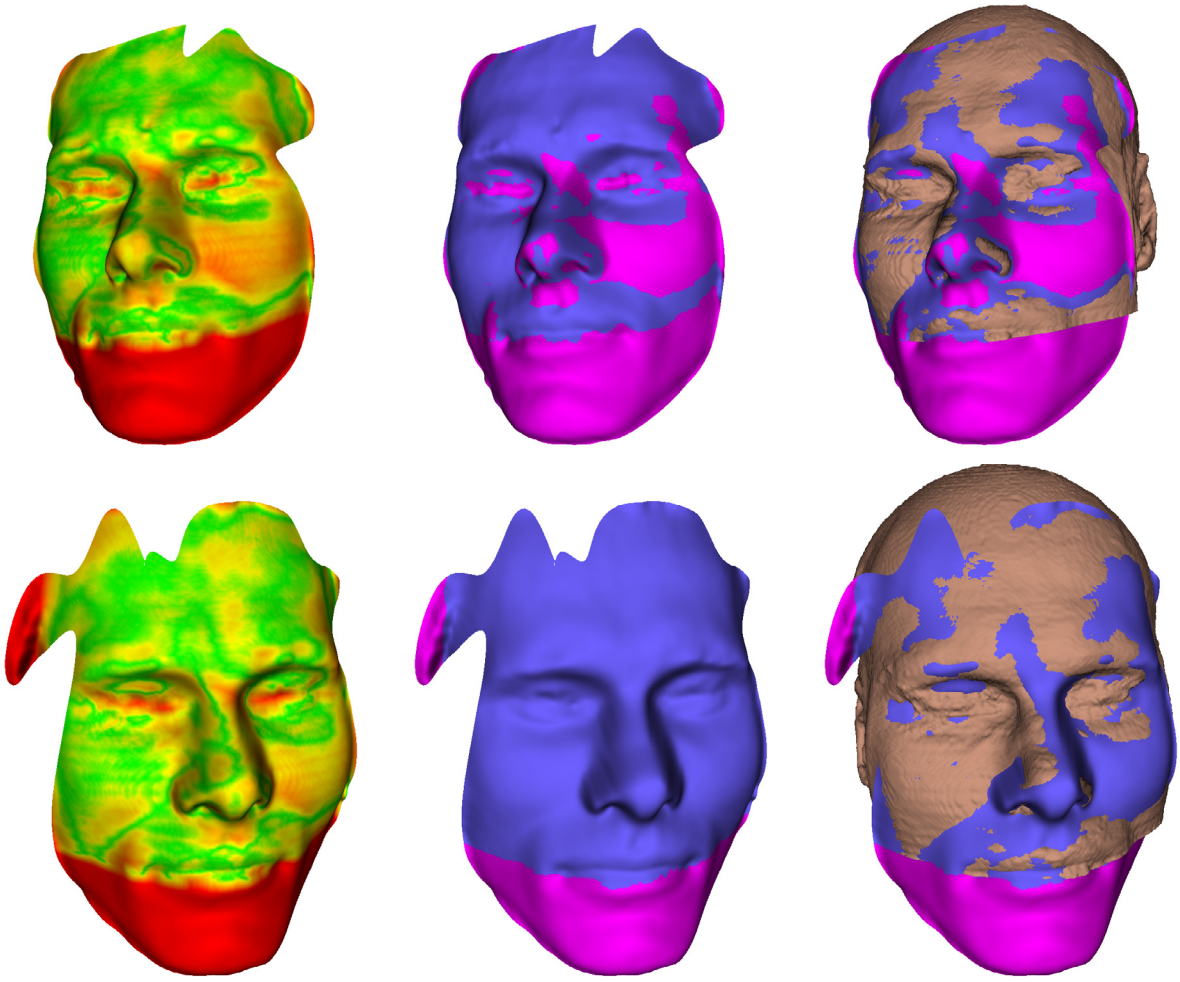

Figure 7.4: Shape measurement registration results for volunteer 1, front

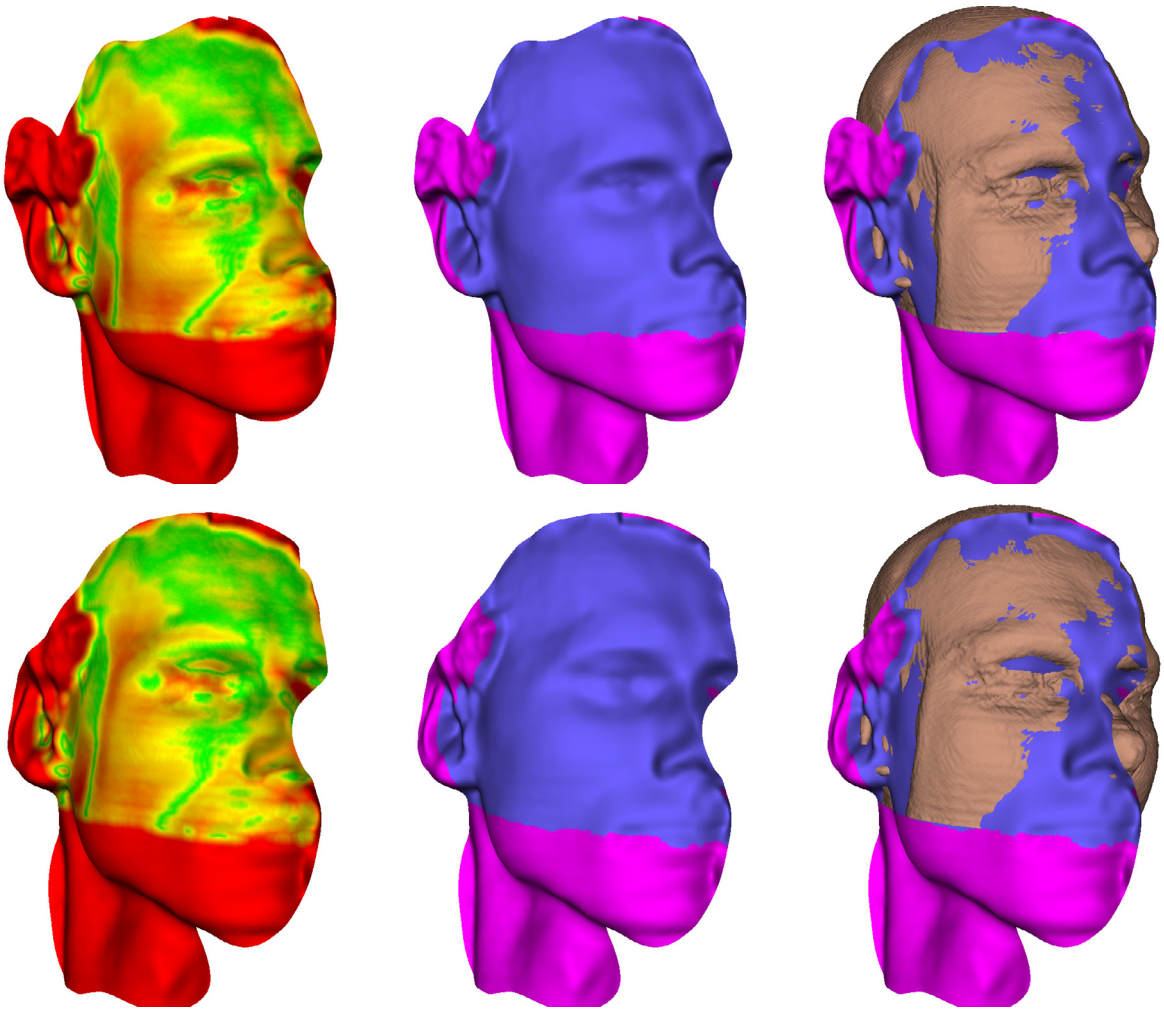

Figure 7.5: Shape measurement registration results for volunteer 1, left

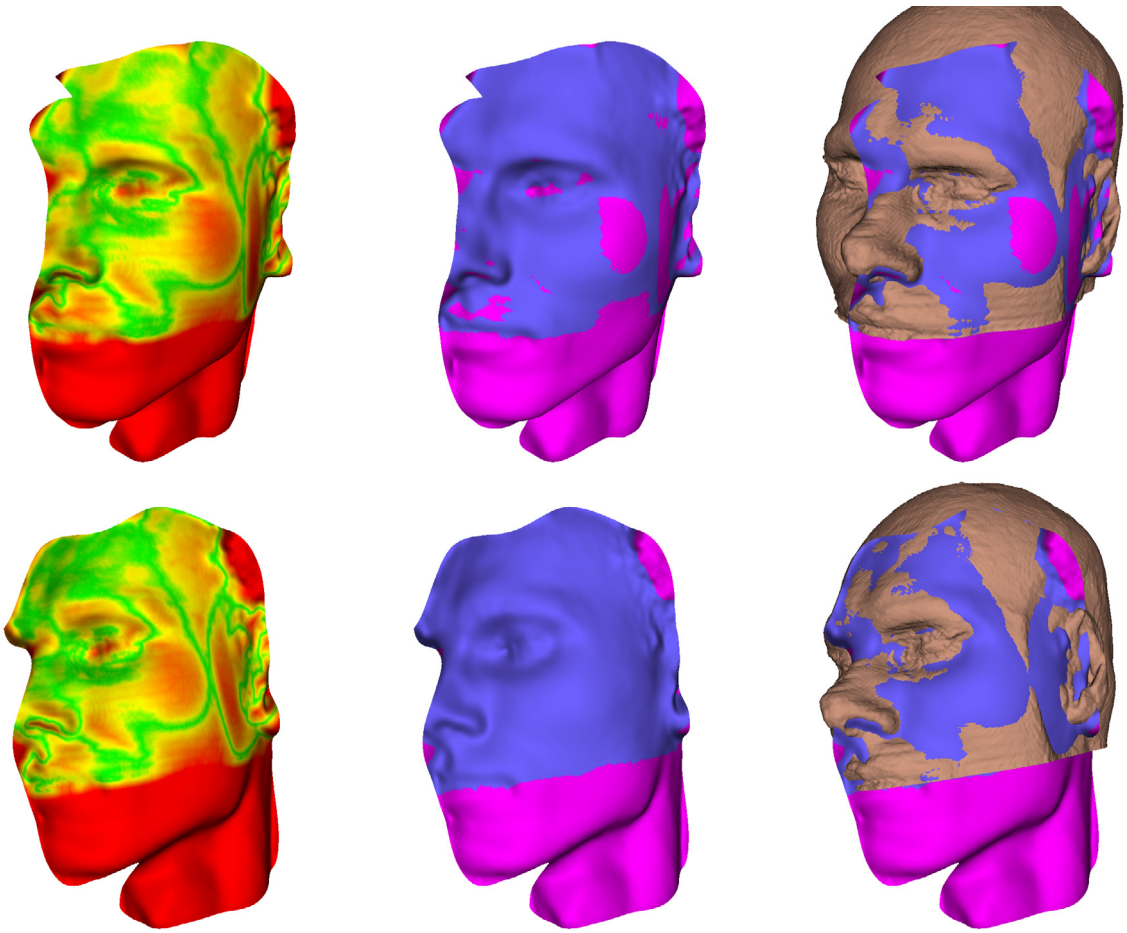

Figure 7.6: Shape measurement registration results for volunteer 1, right

7.2.2 Volunteer 2

Take	Mean distance	Overlap	NAI	Time
Front 1	0.98 mm	83.9%	3.34	48s
Front 2	0.97 mm	84.3%	3.35	53s
Left 1	1.62 mm	54.3%	3.50	101s
Left 2	1.62 mm	54.8%	3.32	108s
Right 1	1.32 mm	67.6%	4.85	110s
Right 2	1.18 mm	68.6%	4.52	148s

Table 7.3: Shape measurement registration results for volunteer 2

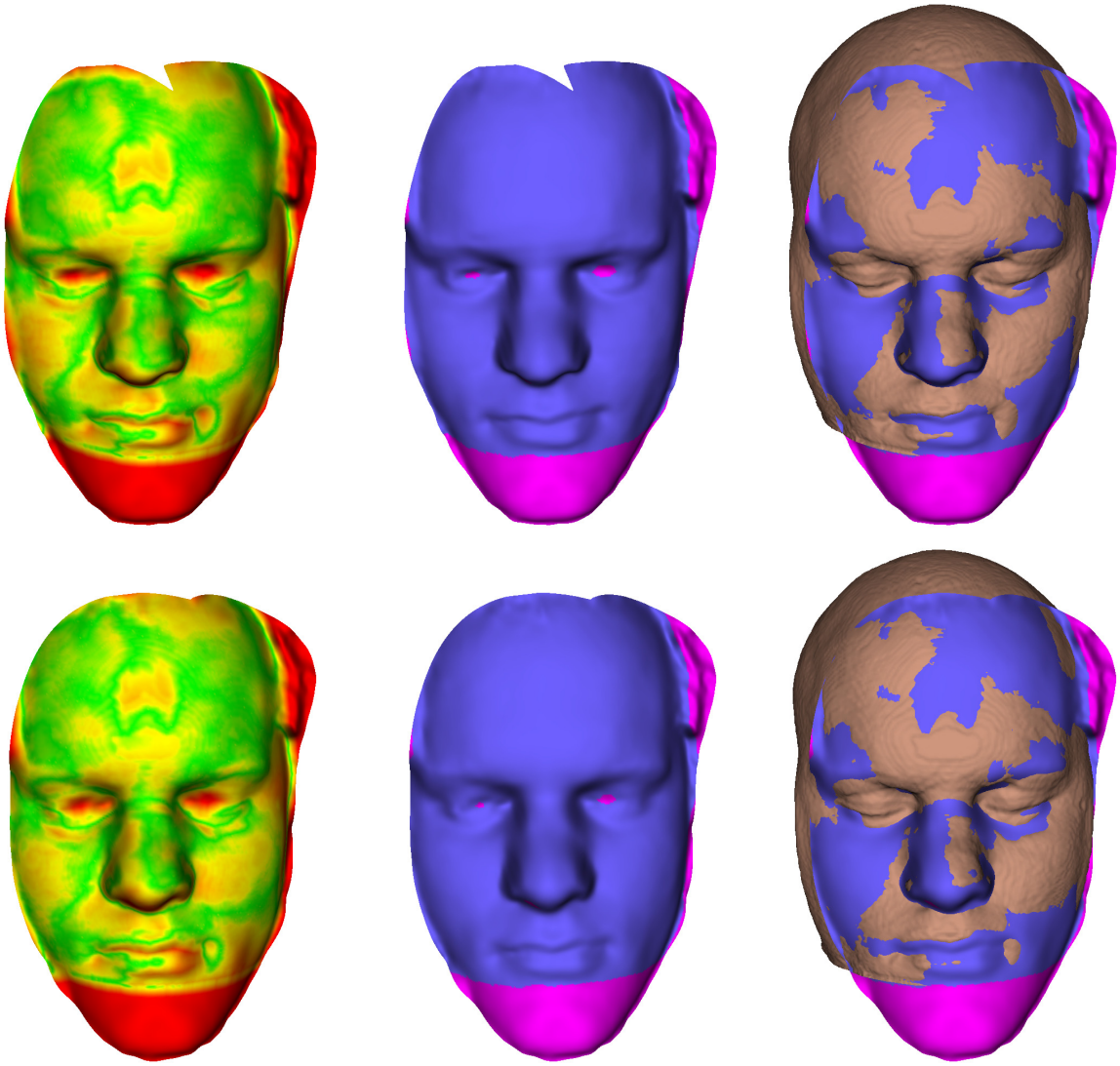

Figure 7.7: Shape measurement registration results for volunteer 2, front

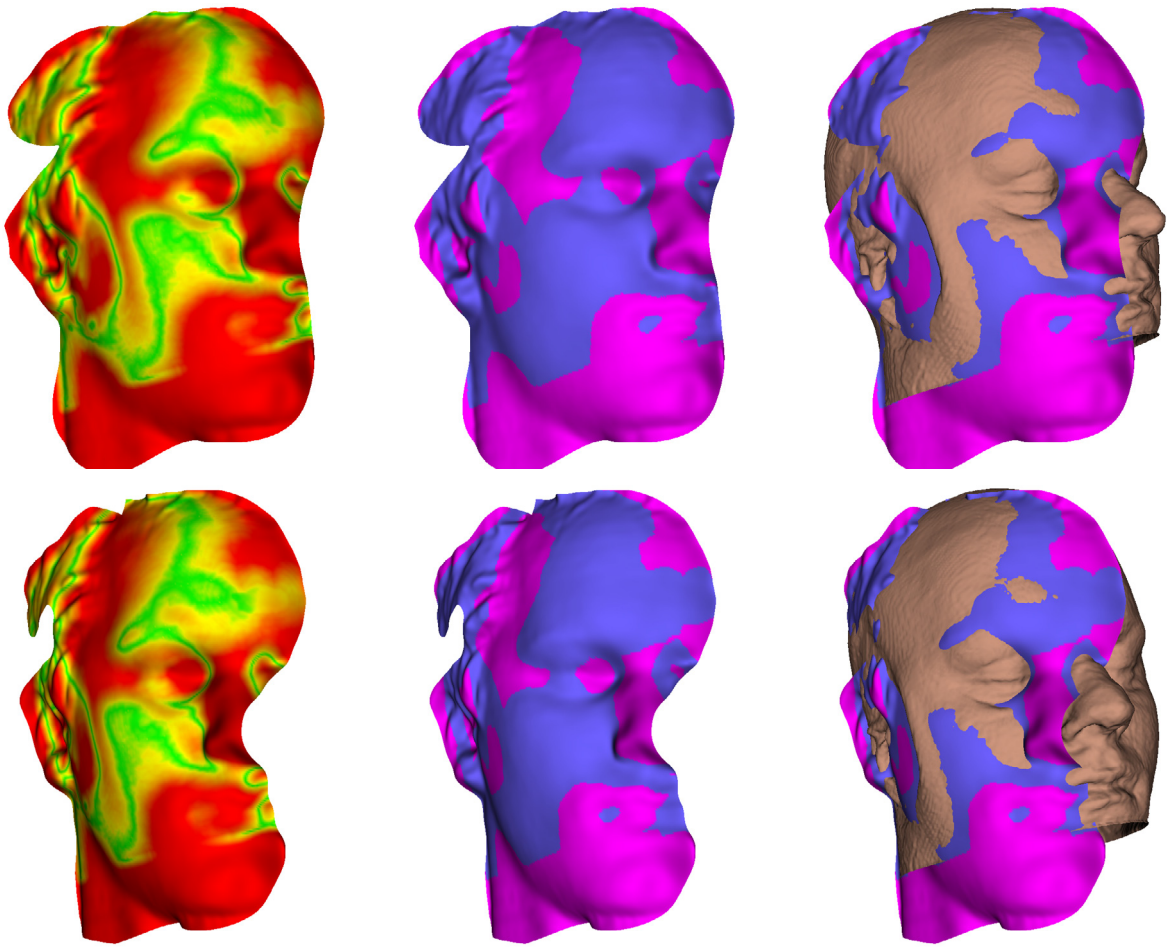

Figure 7.8: Shape measurement registration results for volunteer 2, left

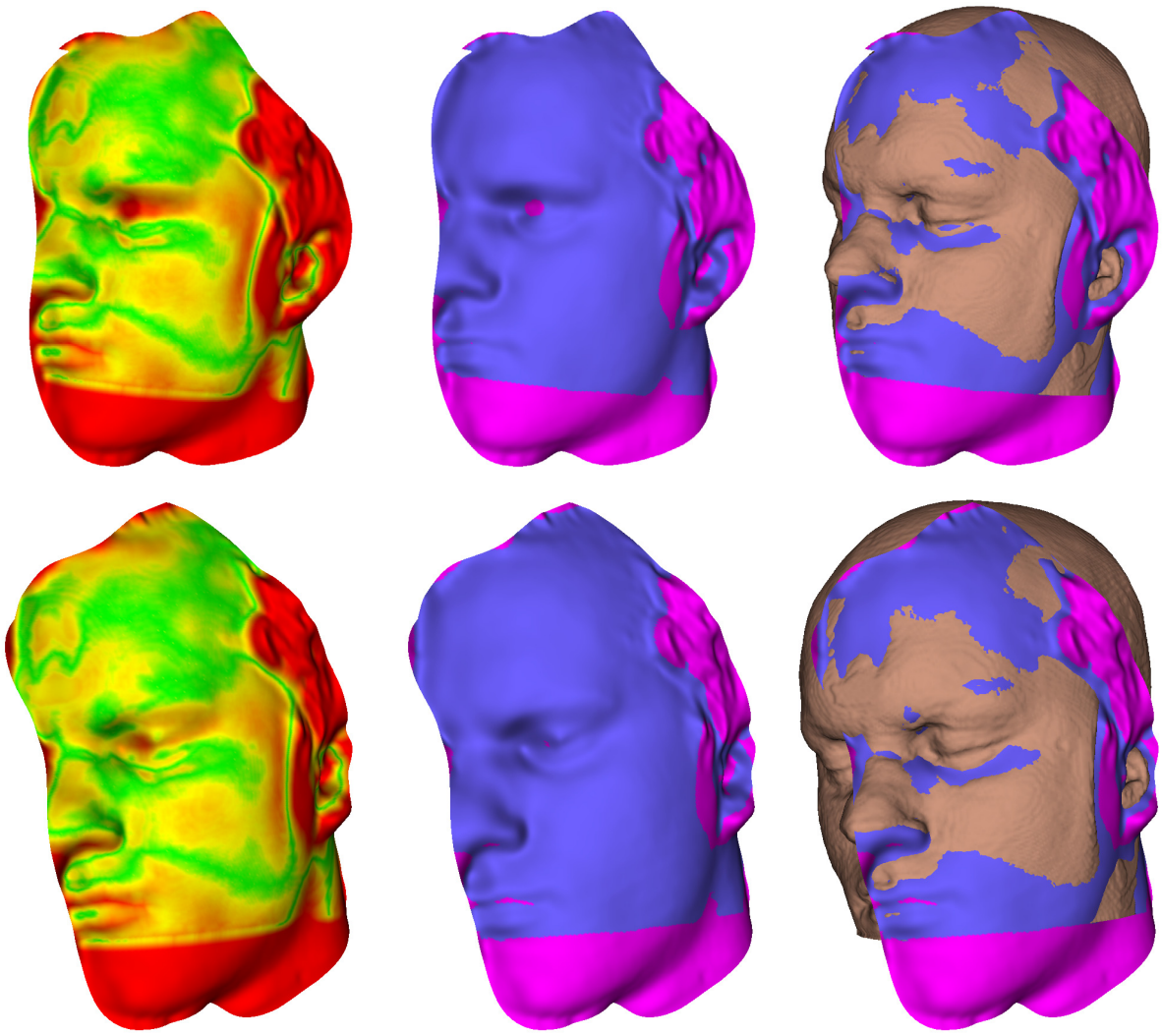

Figure 7.9: Shape measurement registration results for volunteer 2, right

7.2.3 Phantom

Take	Mean distance	Overlap	NAI	Time
Front 1	0.37 mm	82.6%	2.29	40s
Front 2	0.37 mm	82.9%	2.25	40s
Left 1	0.55 mm	84.3%	2.91	71s
Left 2	0.55 mm	84.2%	2.89	68s
Right 1	0.58 mm	73.7%	3.43	57s
Right 2	0.58 mm	73.7%	3.40	66s
Back 1	0.54 mm	83.4%	0.32	58s
Back 2	0.55 mm	85.6%	0.33	60s
Sit 1	0.37 mm	84.8%	1.84	43s
Sit 2	0.39 mm	85.7%	1.85	41s

Table 7.4: Shape measurement registration results for the phantom

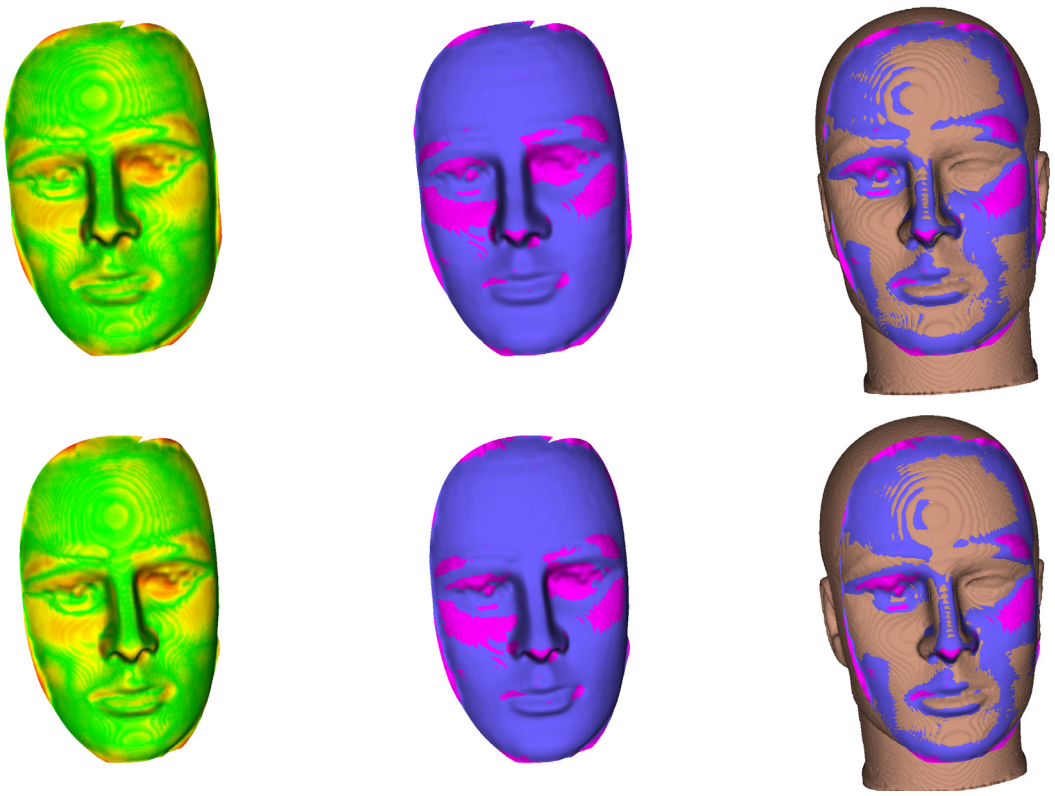

Figure 7.10: Shape measurement registration results for the phantom, front

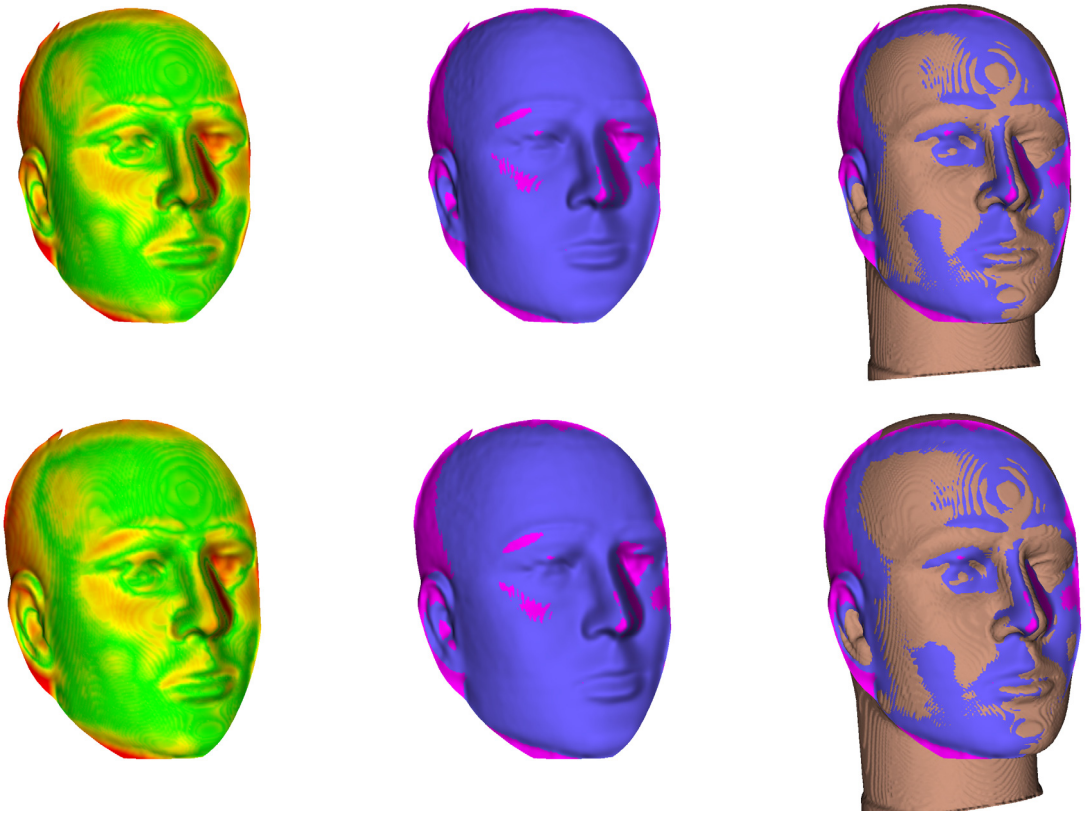

Figure 7.11: Shape measurement registration results for the phantom, left

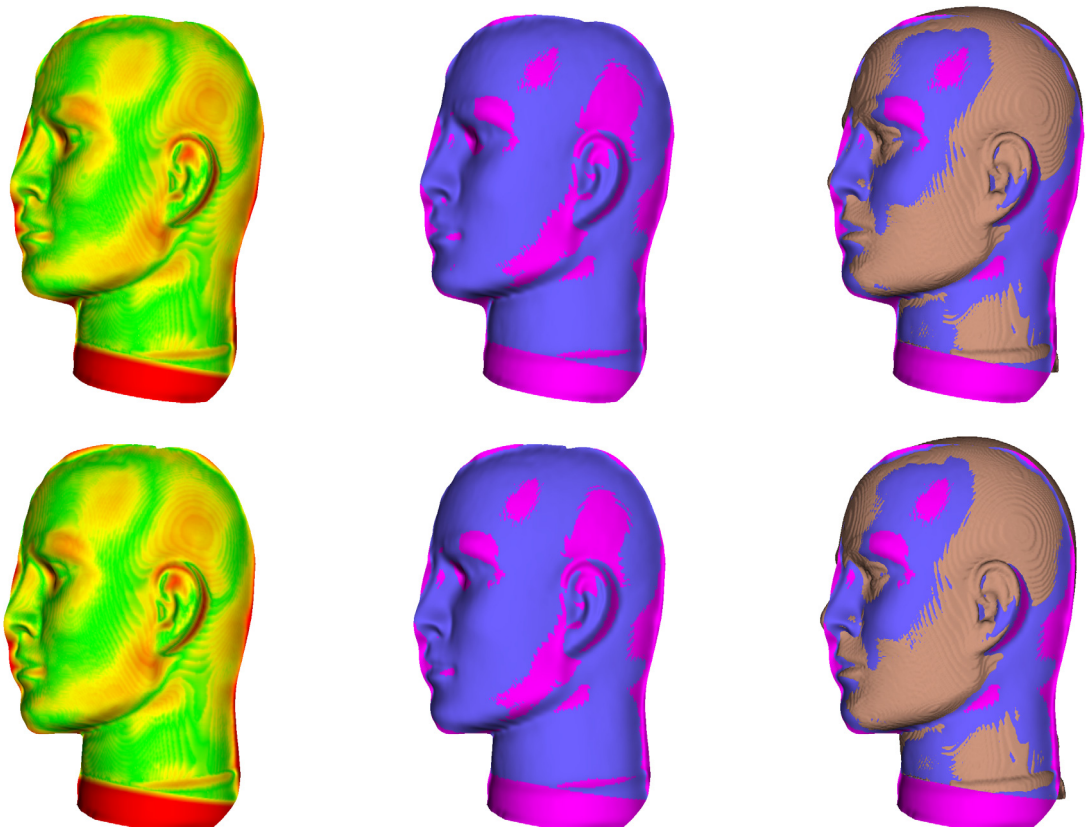

Figure 7.12: Shape measurement registration results for the phantom, right

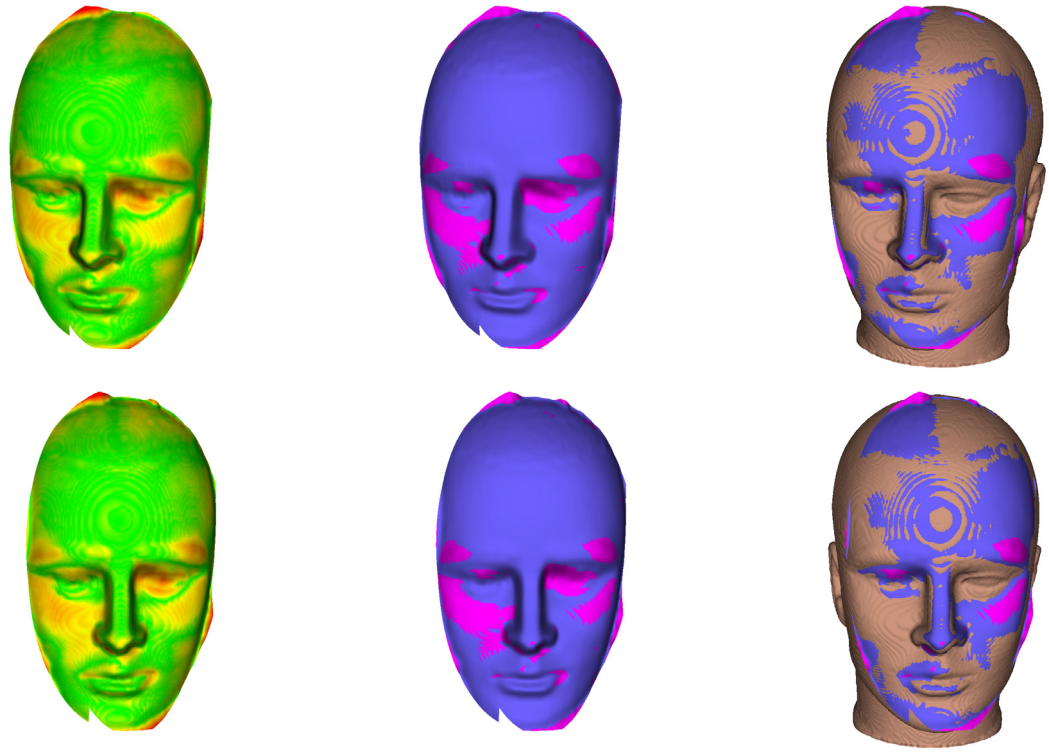

Figure 7.13: Shape measurement registration results for the phantom, sitting

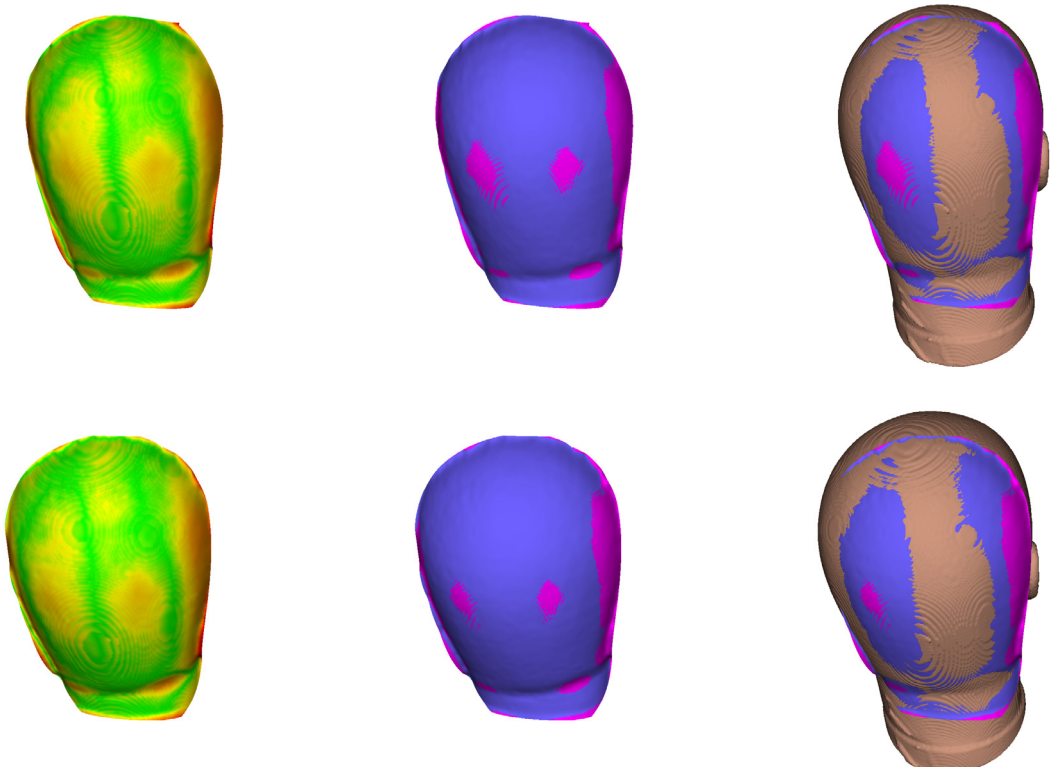

Figure 7.14: Shape measurement registration results for the phantom, back

7.3 Registration Using Tracking Device

For the tracking device registration each position was sampled with three different patterns. The first pattern is called *cross* and consists of moving the tracker back and fourth from an central position in four different directions. The second pattern is called *around* and starts at the nose, moves up over the top of the head to the back of the head, then goes counter-clockwise three quarters around the head, and then up to the top. The third pattern is called *free* and is free-hand sampling as the operator sees fit. All patterns were repeated to test reproducibility.[1]. The computation time was less than three seconds for all these runs.

[1]For the free-hand pattern this only mean that two freehand patterns was sampled, they need not be the same

7.3.1 Volunteer 1

Take	Number of Points	Mean Distance
Cross 1	173	0.94 mm
Cross 2	135	1.12 mm
Around 1	91	0.86 mm
Around 2	102	0.92 mm
Free 1	153	0.87 mm
Free 2	156	0.83 mm

Table 7.5: Tracking device registration results for volunteer 1

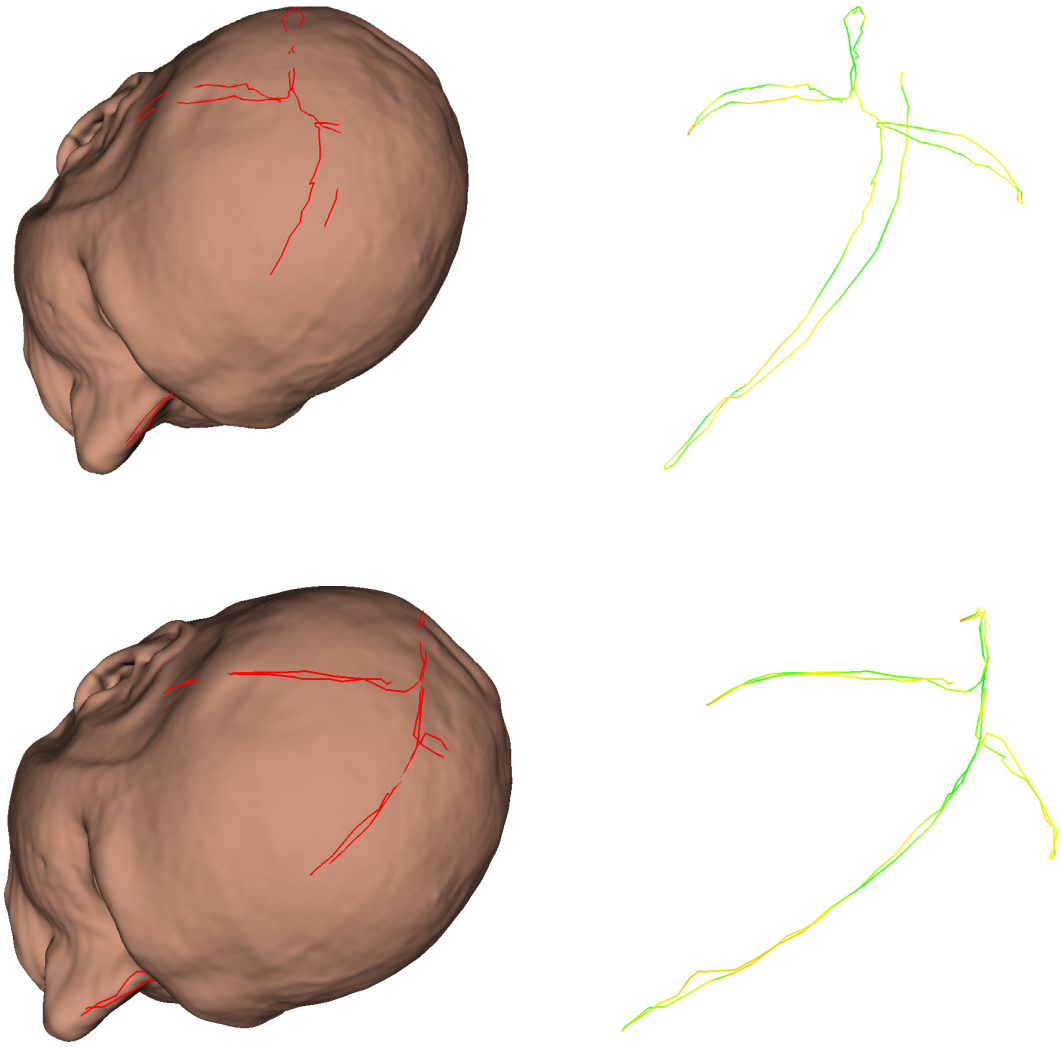

Figure 7.15: Tracking device registration results for volunteer 1, lying on left side, using cross-pattern

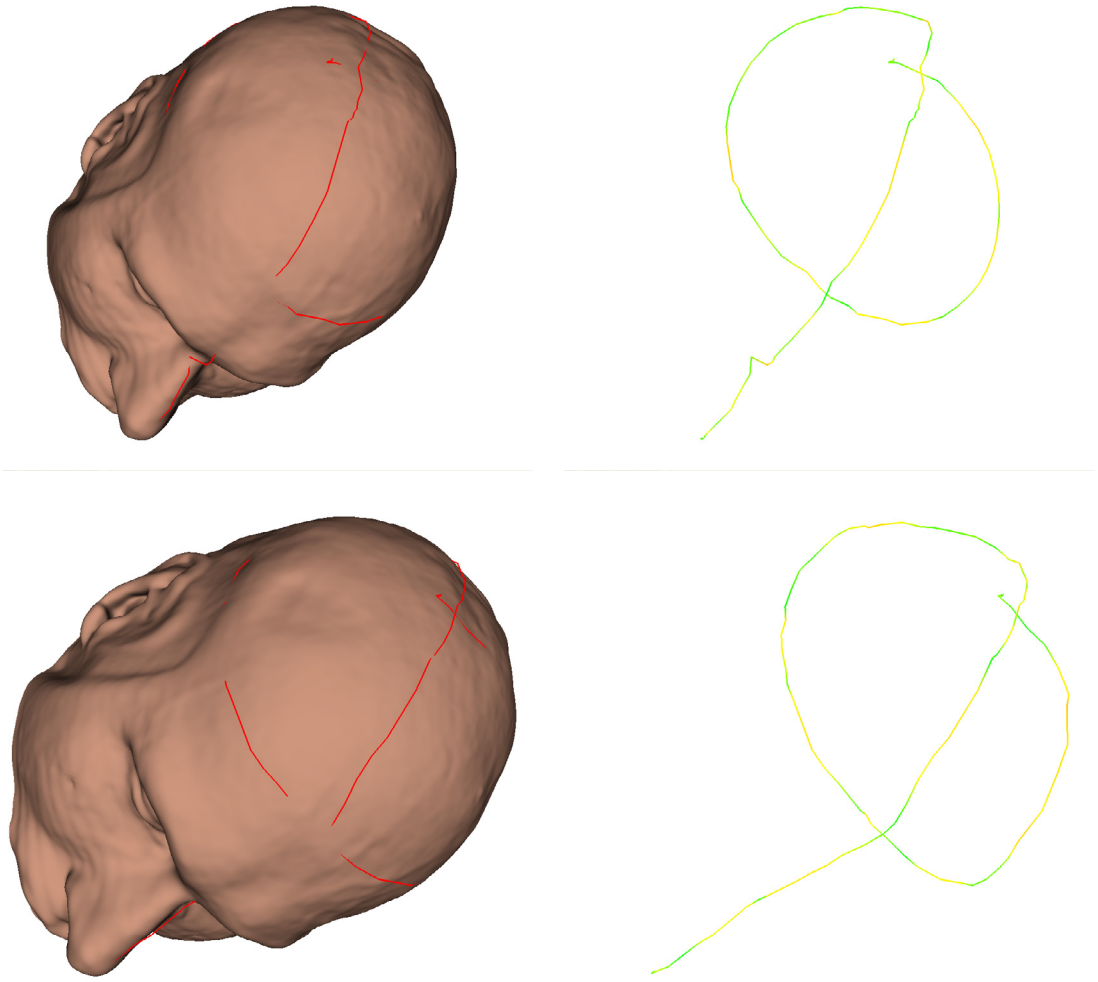

Figure 7.16: Tracking device registration results for volunteer 1, lying on left side, using around-pattern

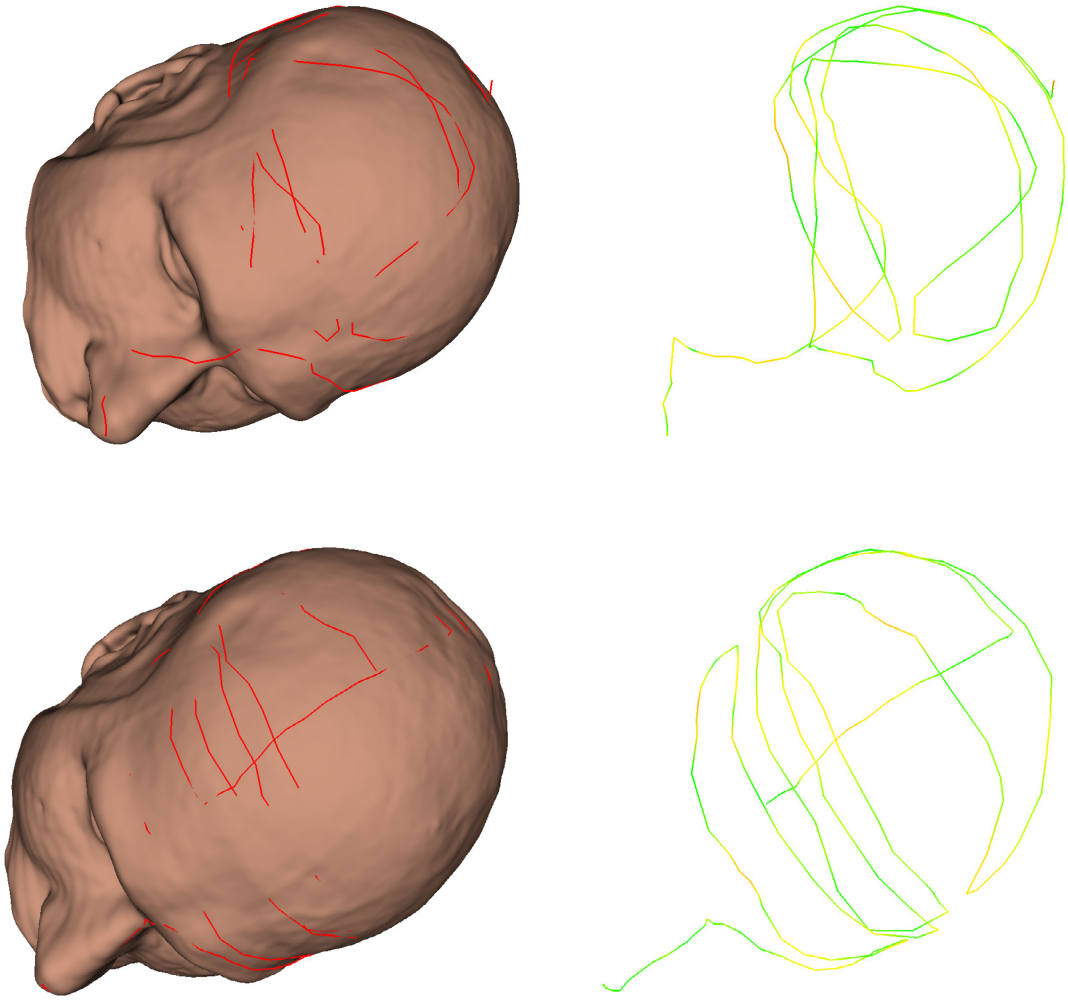

Figure 7.17: Tracking device registration results for volunteer 1, lying on left side, free hand

7.3.2 Volunteer 2

Take	Number of Points	Mean Distance
Cross 1	164	1.36 mm
Cross 2	128	0.78 mm
Around 1	118	1.25 mm
Around 2	102	1.26 mm
Free 1	168	1.48 mm
Free 2	151	1.41 mm

Table 7.6: Tracking device registration results for volunteer 2

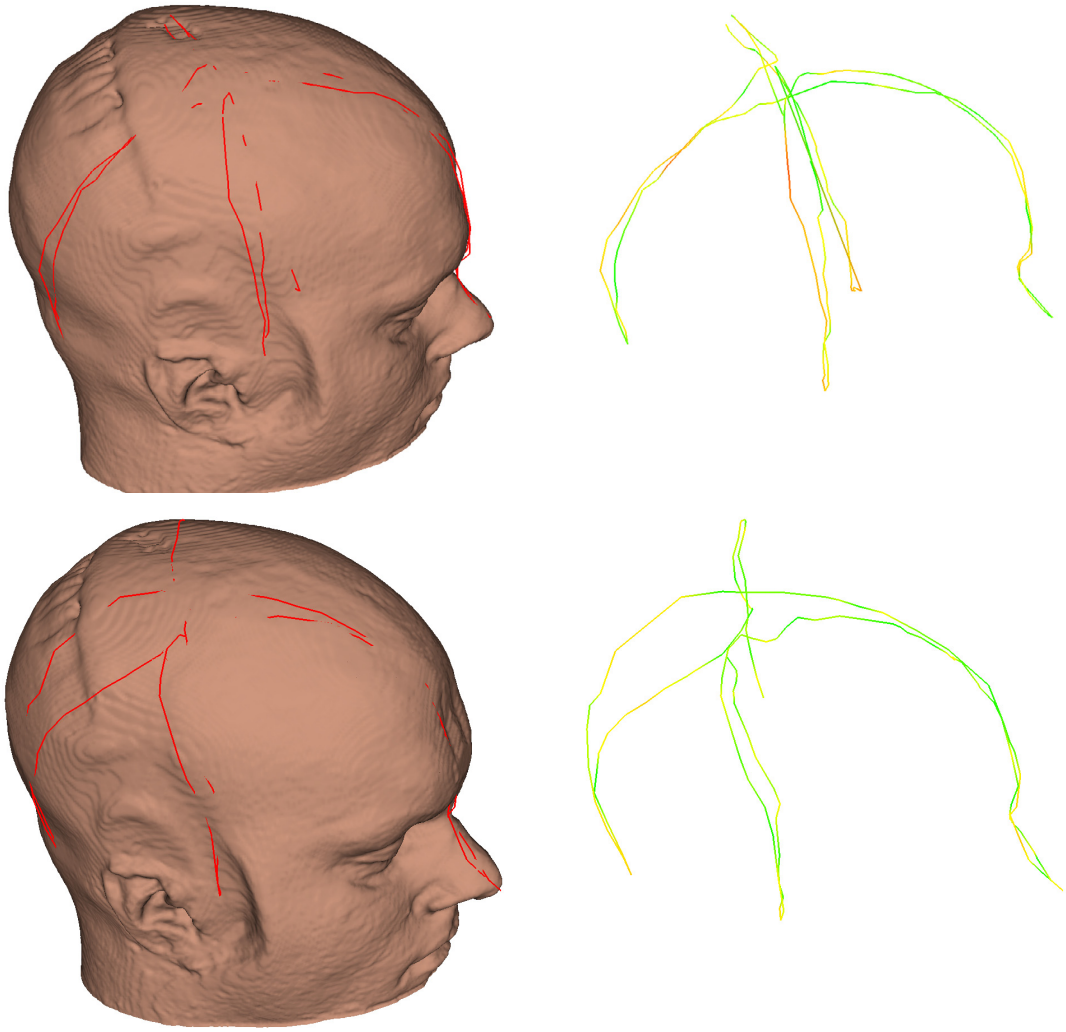

Figure 7.18: Tracking device registration results for volunteer 2, lying on left side, using cross-pattern

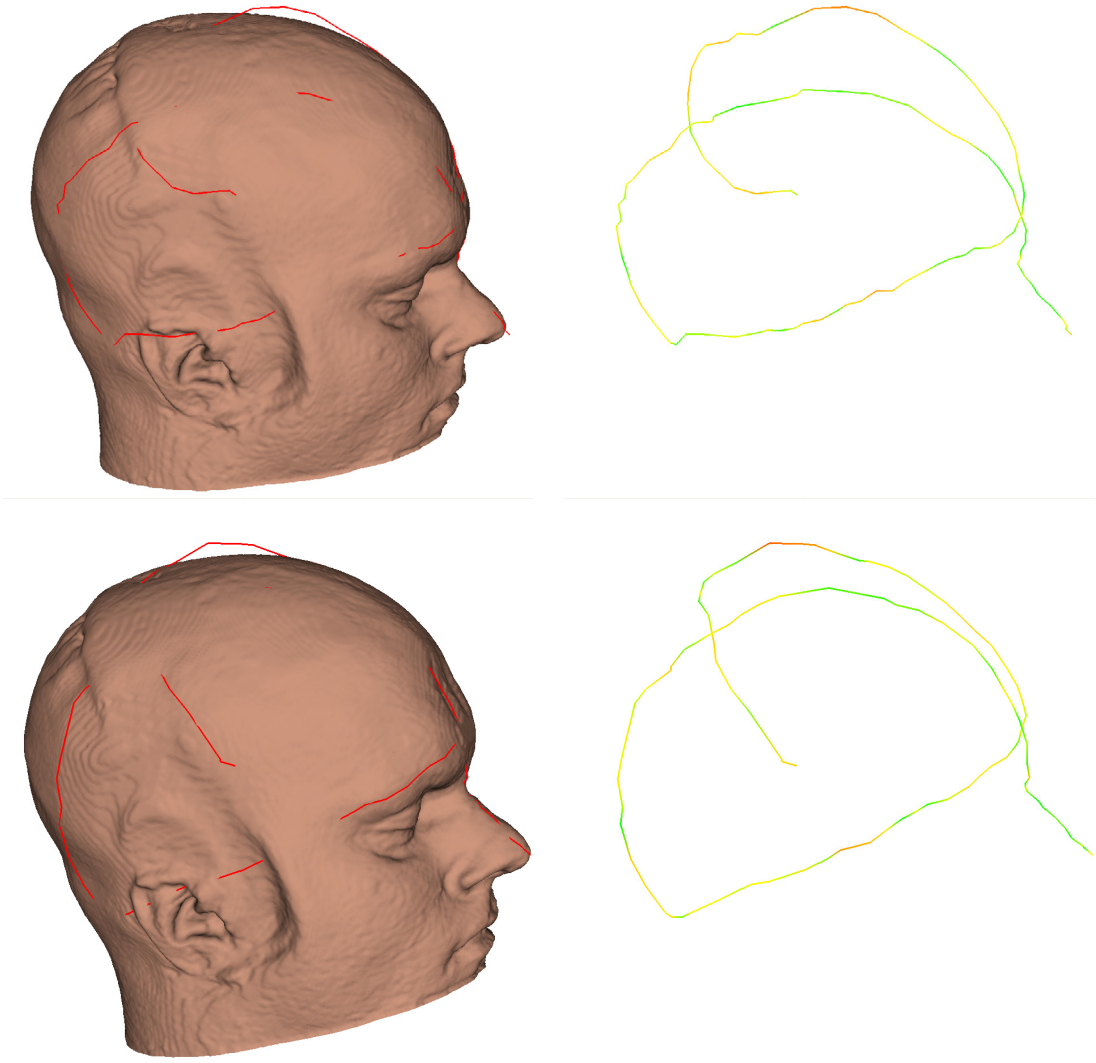

Figure 7.19: Tracking device registration results for volunteer 2, lying on left side, using around pattern

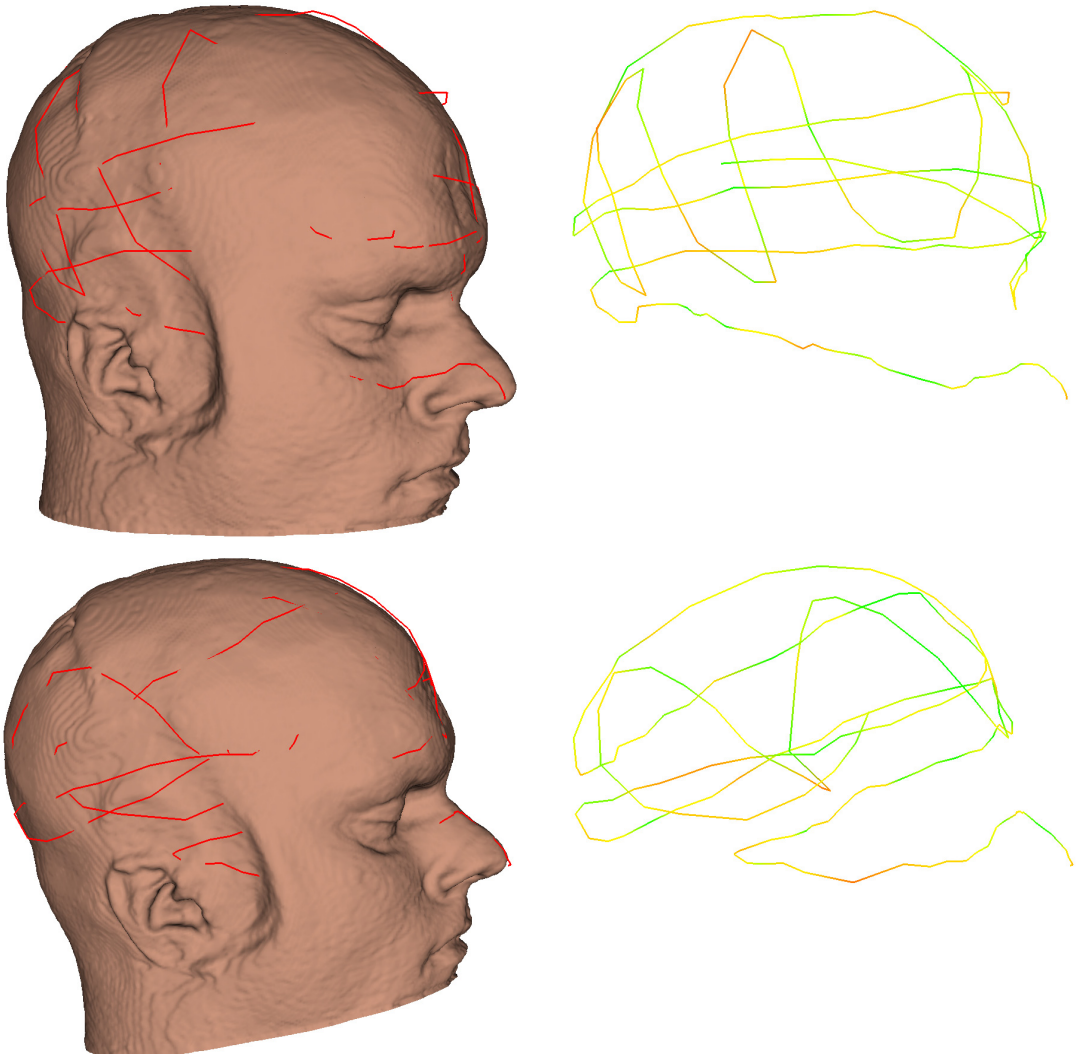

Figure 7.20: Tracking device registration results for volunteer 2, lying on left side, free hand

7.3.3 Phantom

Position	Take	Number of Points	Mean Distance
Front	Cross 1	173	0.94 mm
	Cross 2	135	1.12 mm
	Around 1	91	0.86 mm
	Around 2	102	0.92 mm
	Free 1	153	0.87 mm
	Free 2	156	0.83 mm
Left	Cross 1	173	0.94 mm
	Cross 2	135	1.12 mm
	Around 1	91	0.86 mm
	Around 2	102	0.92 mm
	Free 1	153	0.87 mm
	Free 2	156	0.83 mm
Sit	Cross 1	173	0.94 mm
	Cross 2	135	1.12 mm
	Around 1	91	0.86 mm
	Around 2	102	0.92 mm
	Free 1	153	0.87 mm
	Free 2	156	0.83 mm

Table 7.7: Tracking device registration results for the phantom

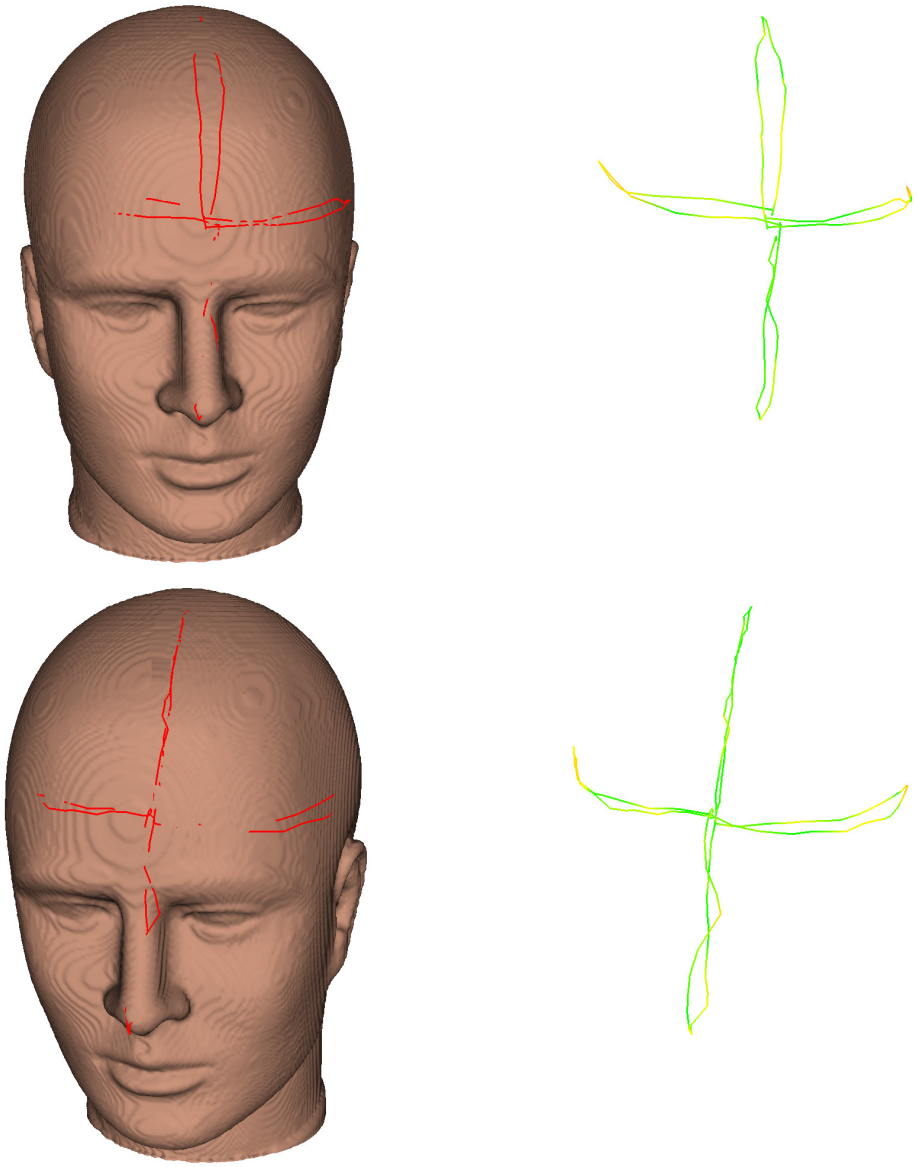

Figure 7.21: Tracking device registration results for the phantom, front, using cross-pattern

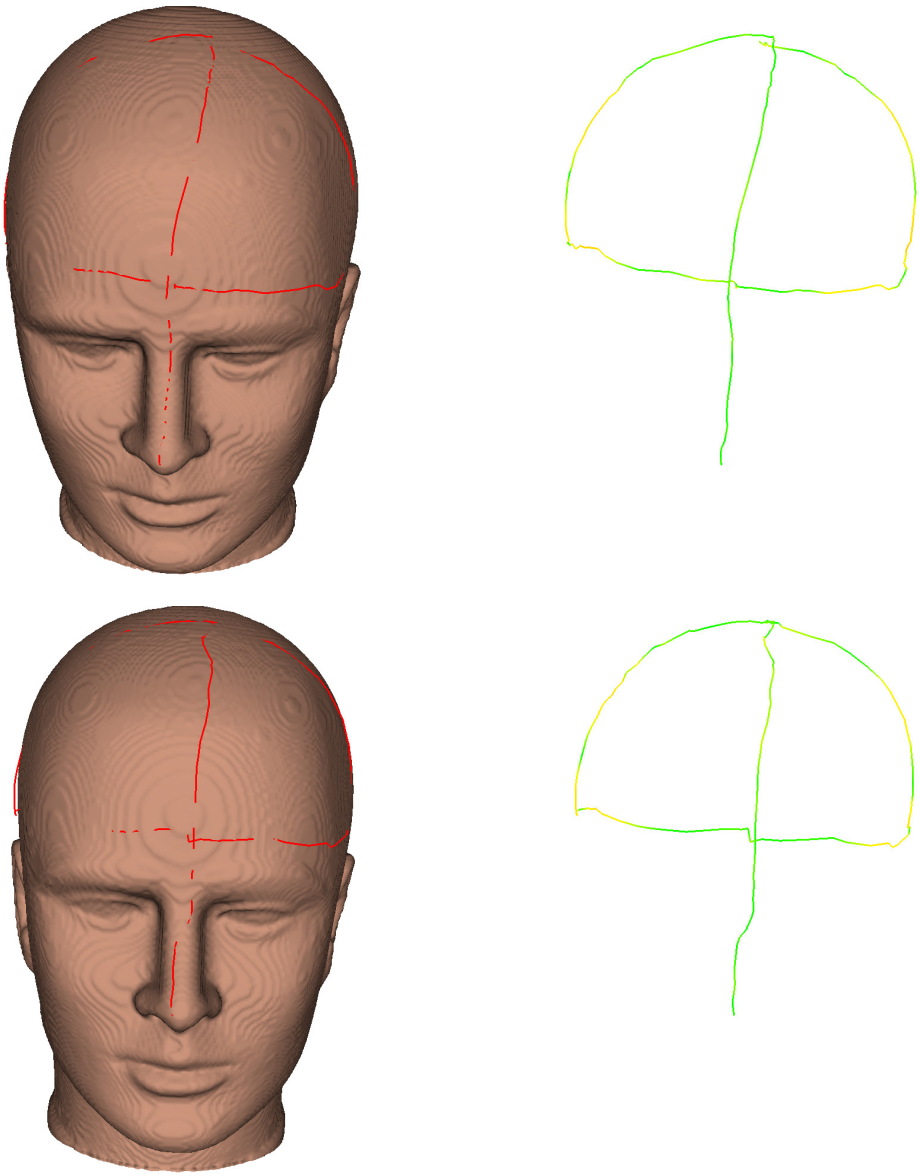

Figure 7.22: Tracking device registration results for the phantom, front, using around-pattern

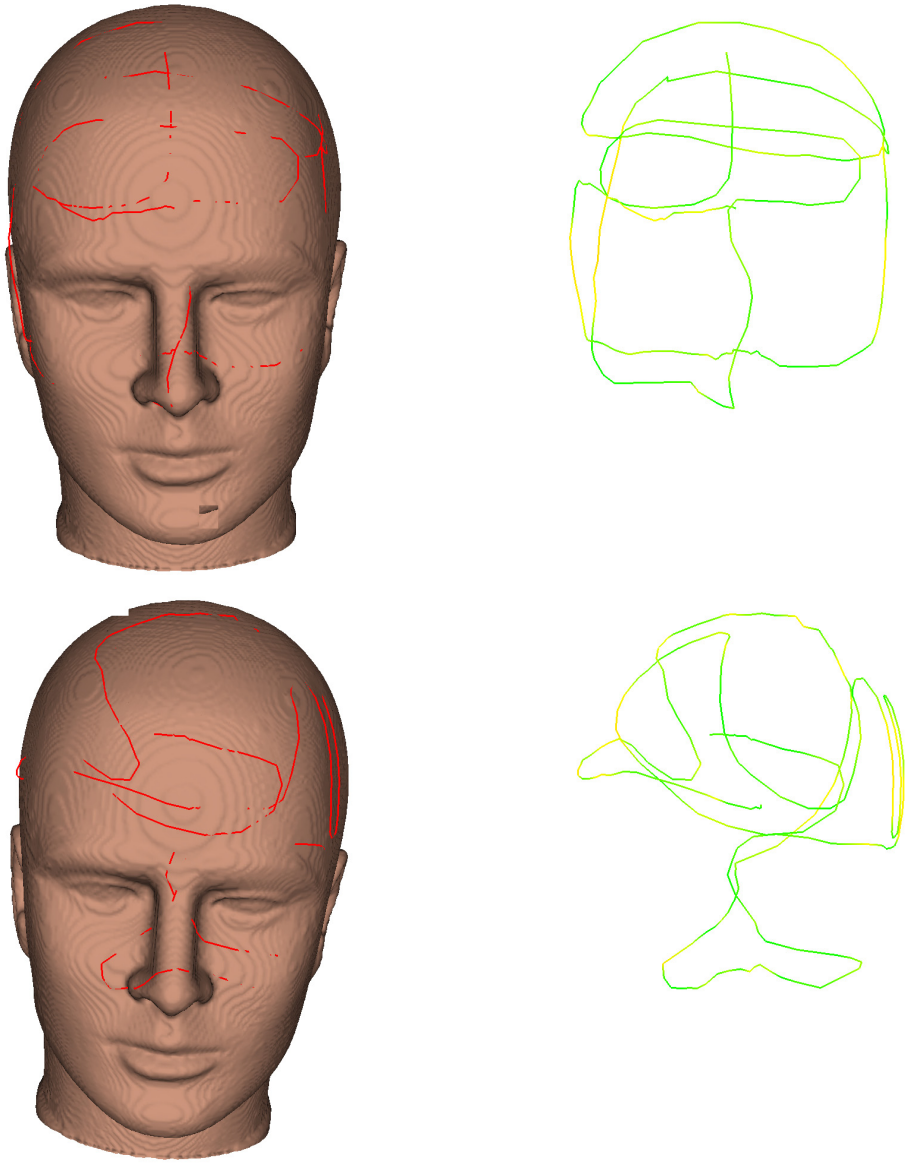

Figure 7.23: Tracking device registration results for the phantom, front, free hand

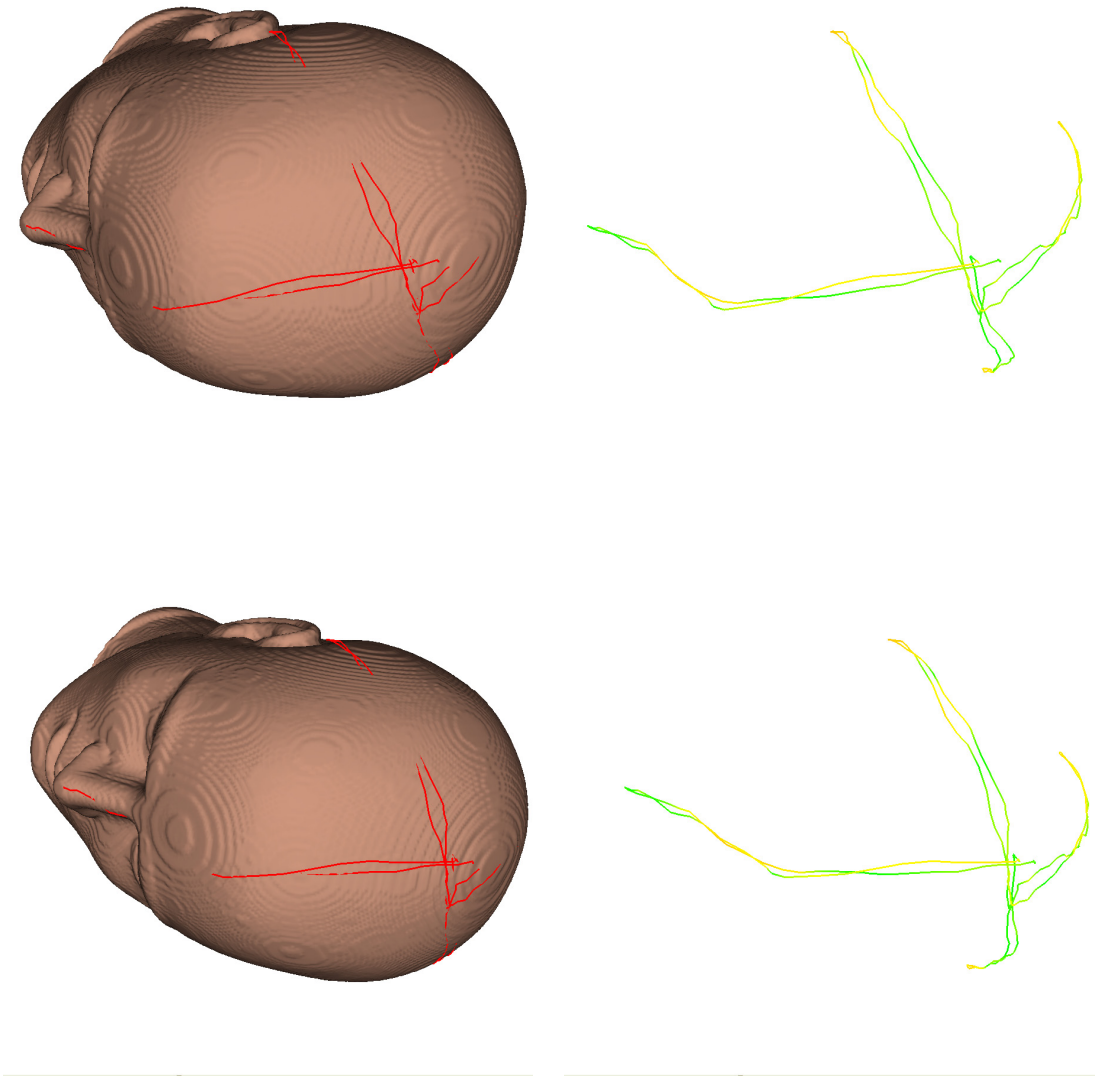

Figure 7.24: Tracking device registration results for the phantom, lying on left side, using cross-pattern

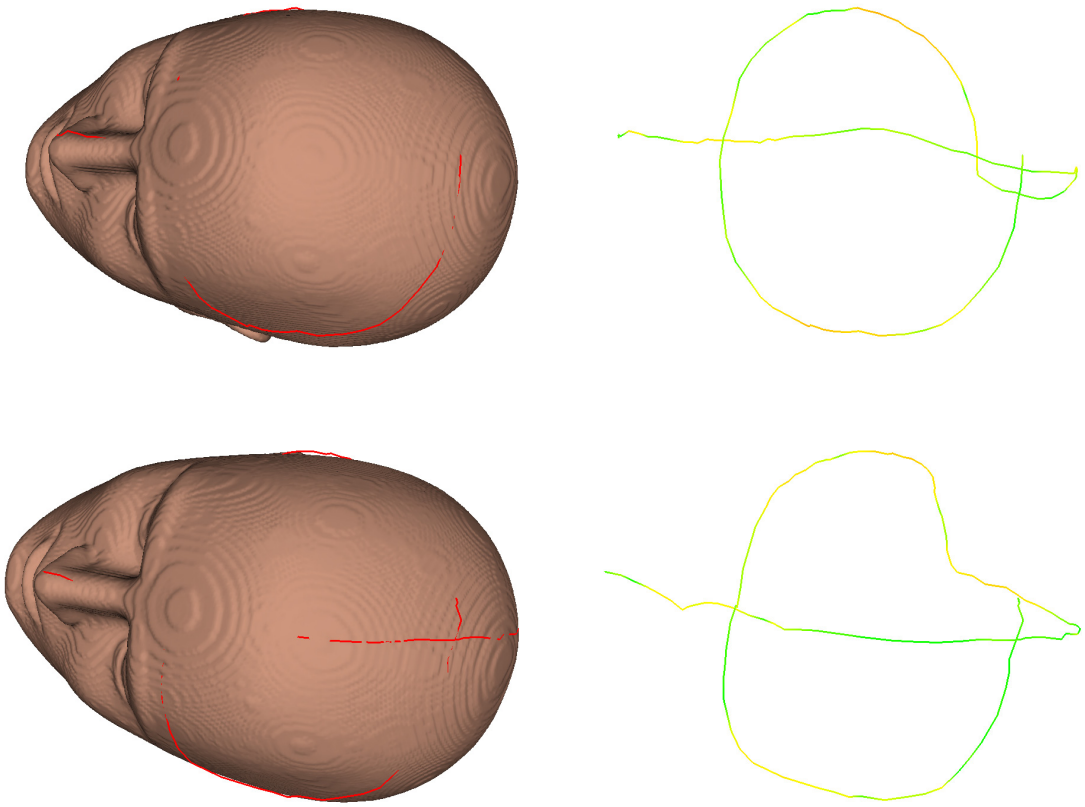

Figure 7.25: Tracking device registration results for the phantom, lying on left side, using around-pattern

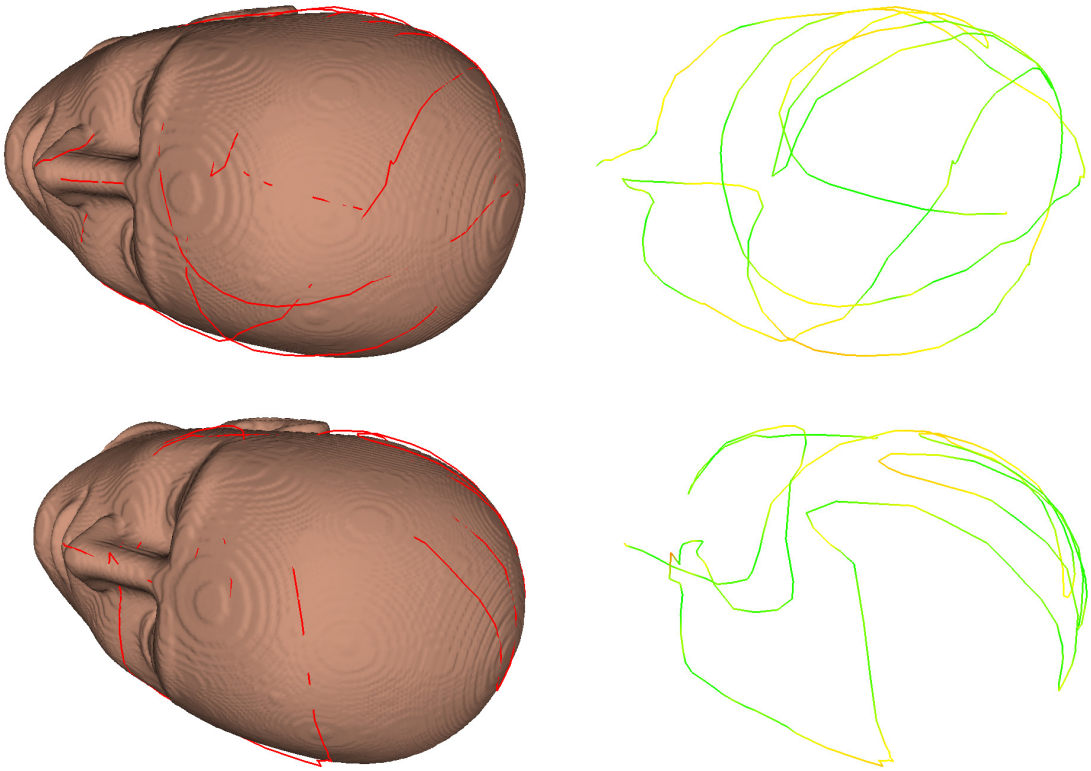

Figure 7.26: Tracking device registration results for the phantom, lying on left side, free hand

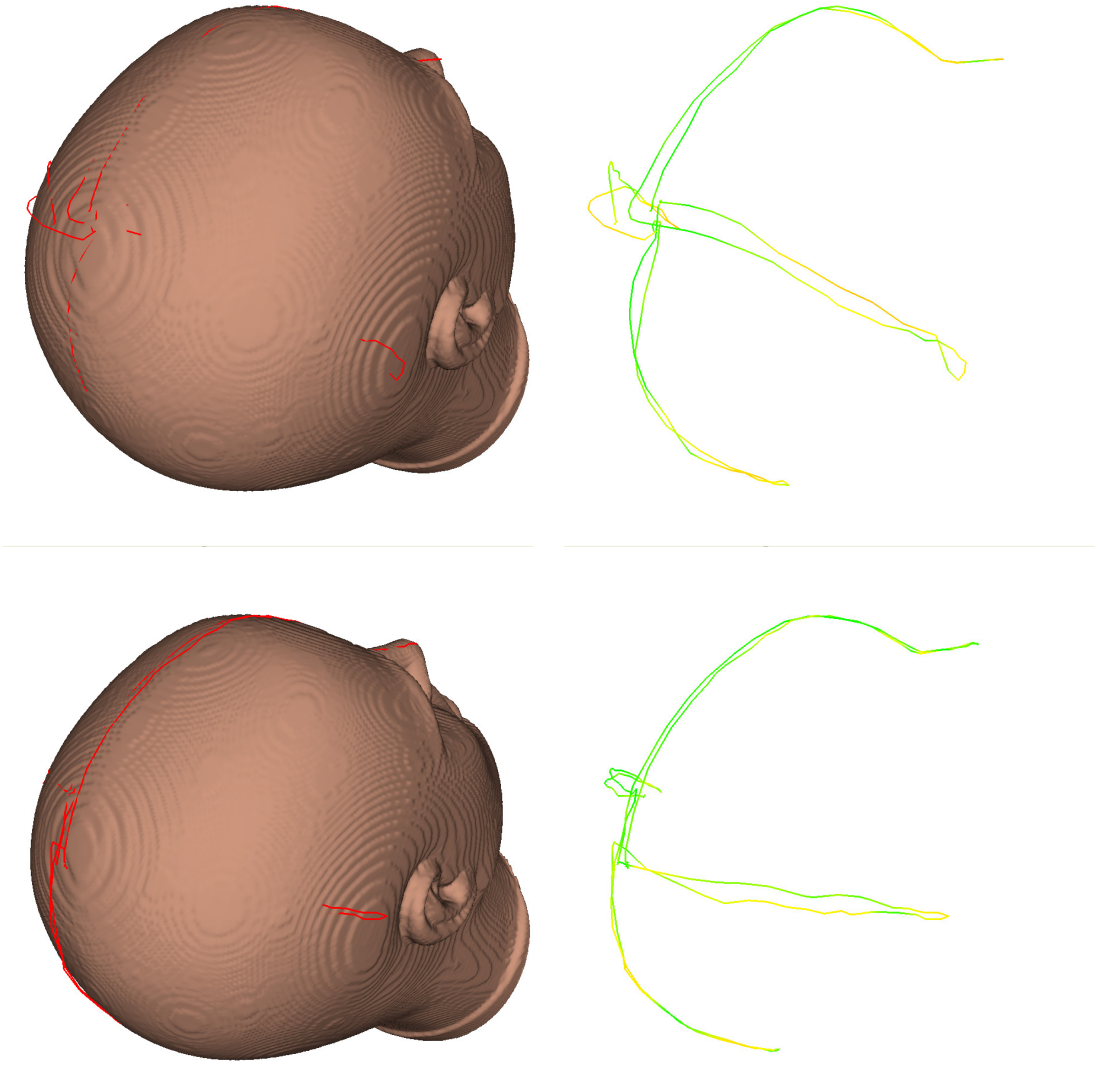

Figure 7.27: Tracking device registration results for the phantom, sitting, using cross-pattern

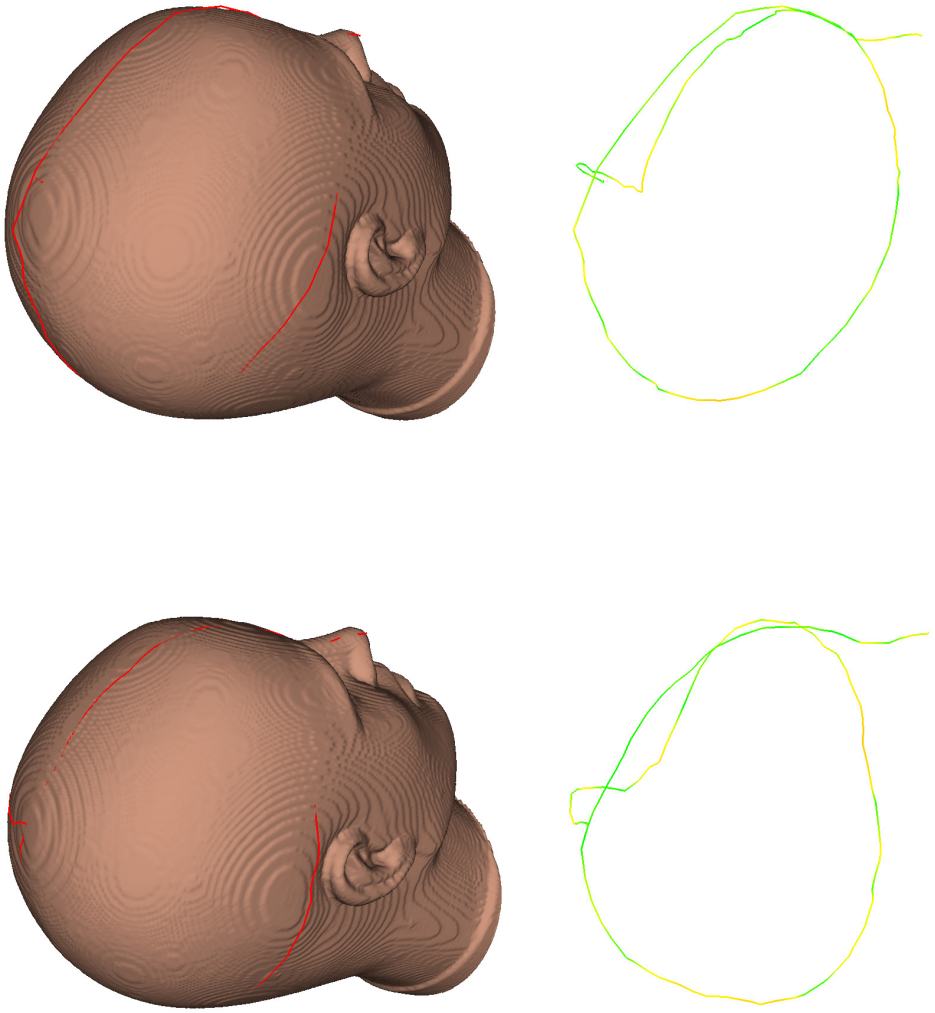

Figure 7.28: Tracking device registration results for the phantom, sitting, using around-pattern

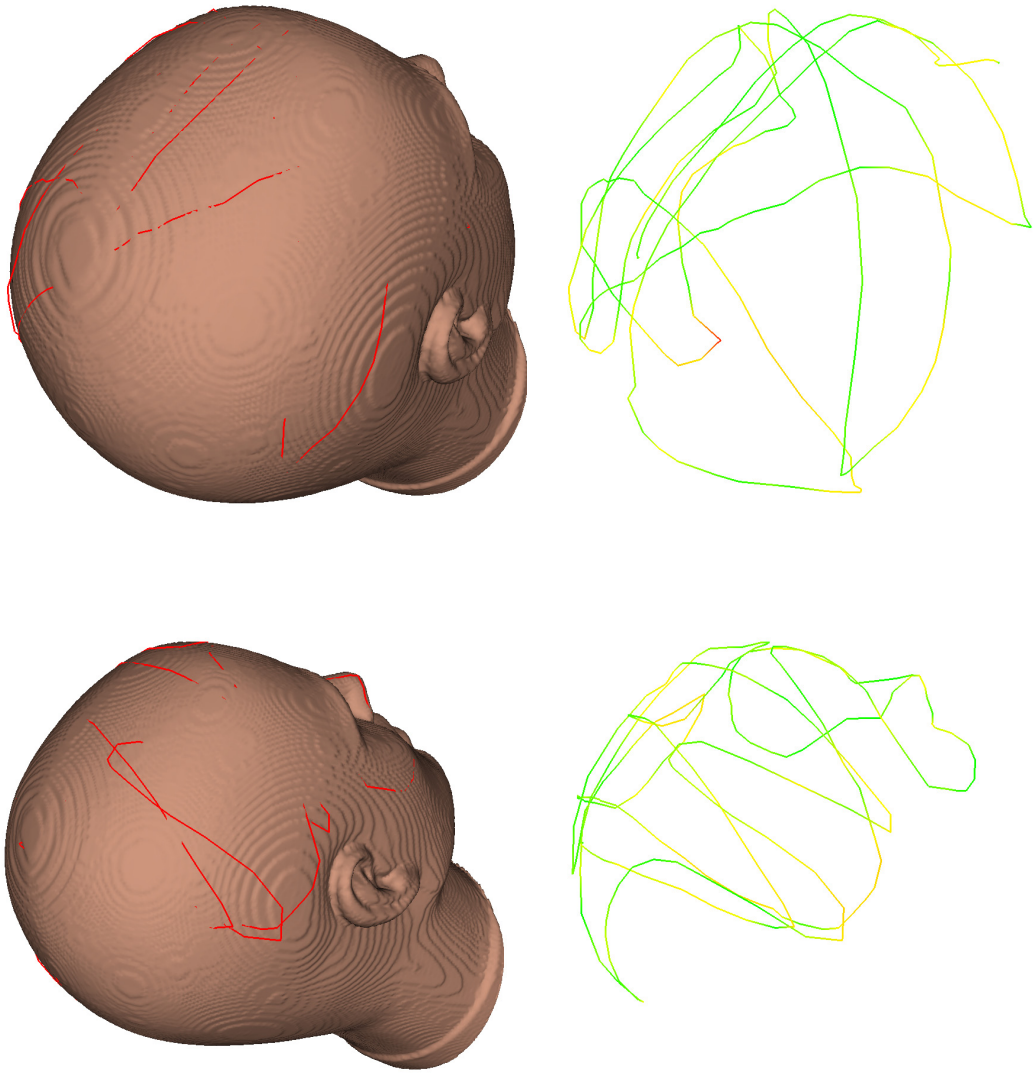

Figure 7.29: Tracking device registration results for the phantom, sitting, free hand

7.4 An In Vitro Experiment

In addition to gathering data for later off line experimentations, we have done real life experimentations with the tracker based method and the phantom. The shape measurement method was not tested this way, since we do not yet have a way to registrate the shape measurement device with the tracking device. The experiment was only run on the phantom, since the time needed to complete a registration (with all manual preparations) is currently longer than one can expect a healthy volunteer to lie completely still.

For the first part of the experiment a registration was done using a 215 point cross-pattern. The resulting mean distance was 0.62 mm. Afterwards the tracker probe were

pointed at different locations on the phantom, and photographs where taken along with screen shots of the navigation computer to show how well aligned the on screen pointer was with the real tracking probe. The results are shown in figure 7.30.

For the second part of the experiment three registration was performed. One using the anatomical landmarks only, and two using refinement with a “cross” and an “around” pattern. Screen shots were taken of the navigation computer with the tracking device at different locations using all three registrations. The pointers distance from the surface on the computer were used as indications of the target registration error.

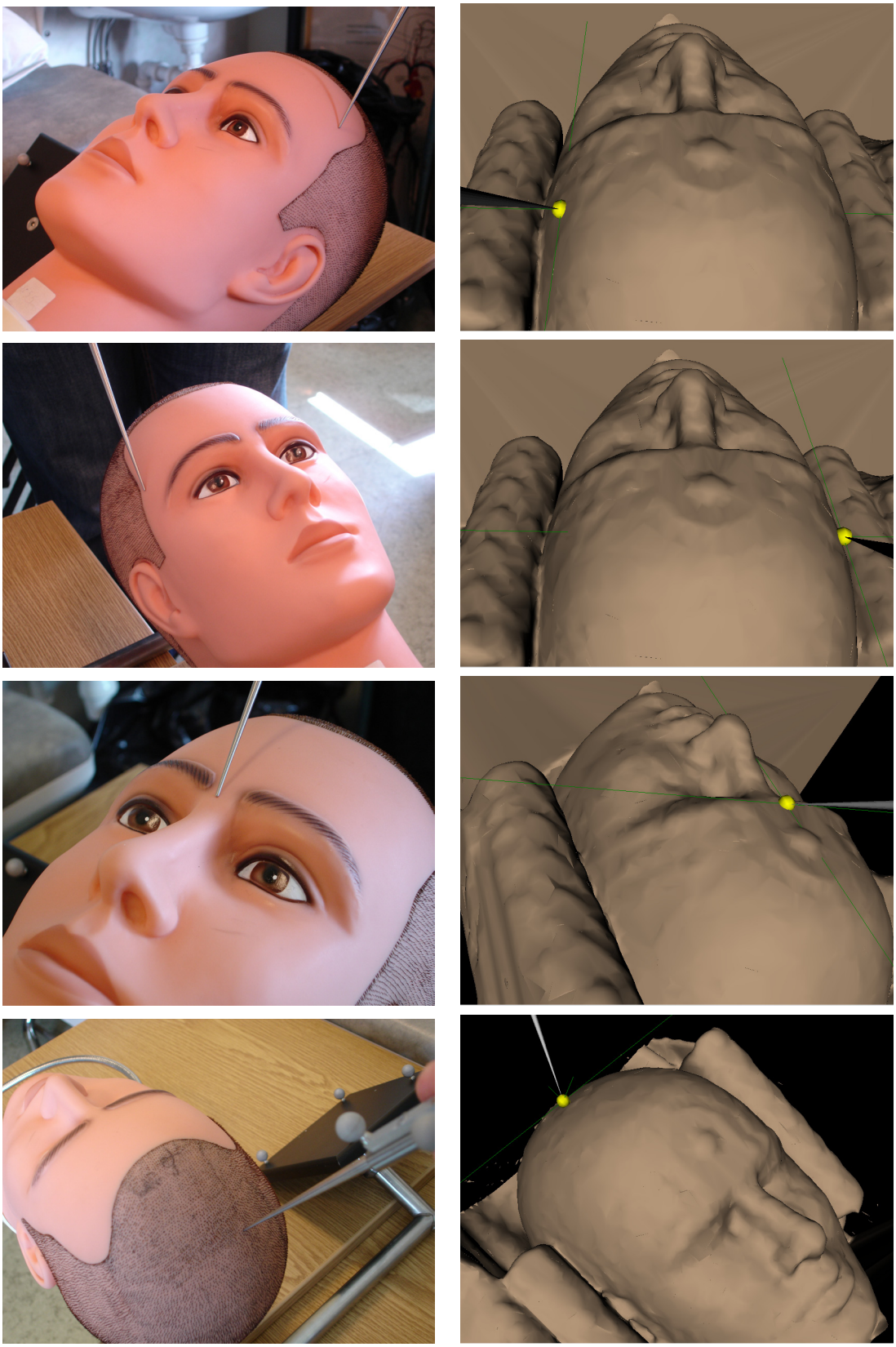

Figure 7.30: Photographs with corresponding screen shots. Left side: Photographs taken of the phantom while holding the tracking device at different positions on it's outside. Right side: Screen shots of the navigation computer showing the resulting tool position after registration for each of the positions. The yellow sphere has 4 mm radius.

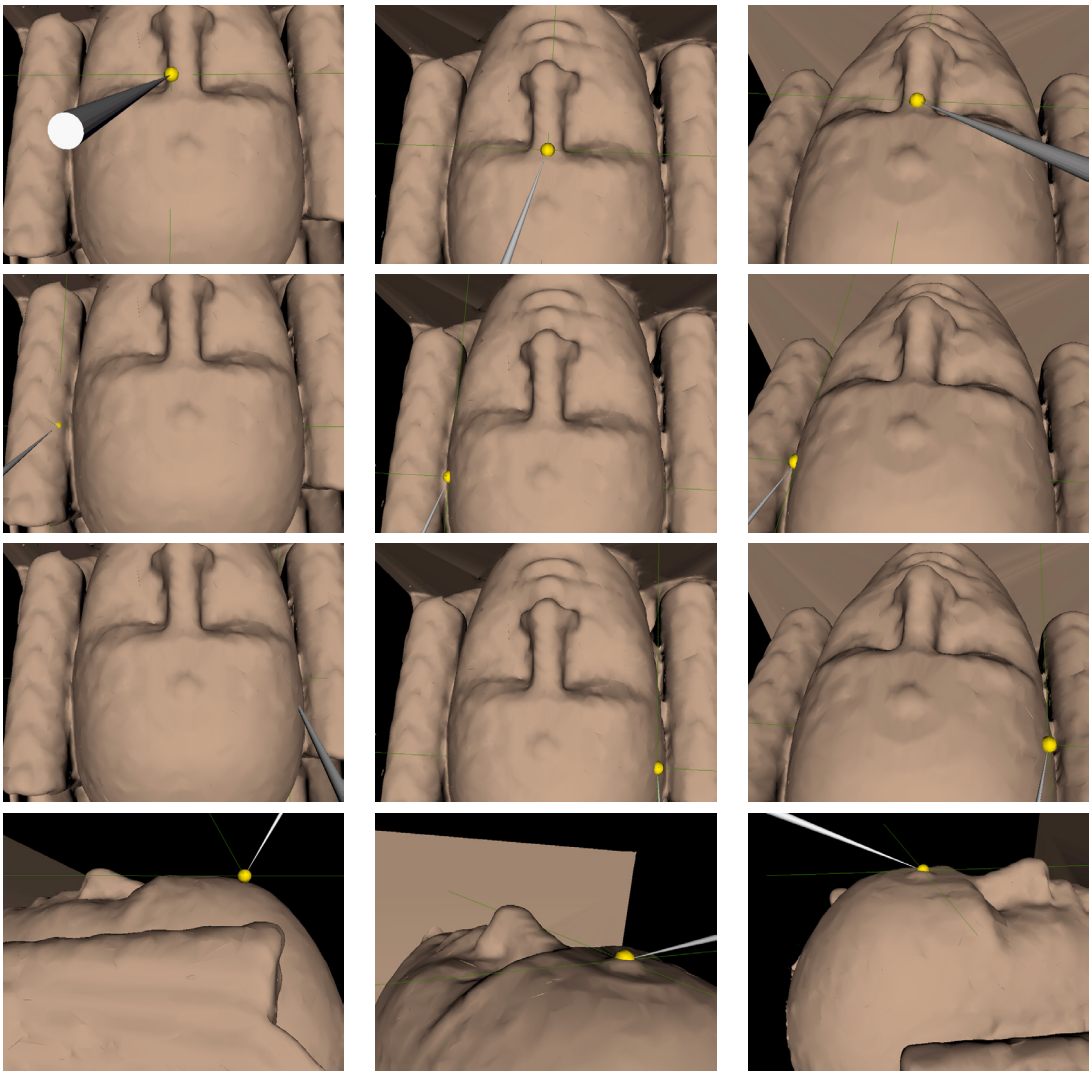

Figure 7.31: Target registration for different methods. Left: Anatomical landmarks. Middle: Cross pattern. Right: Around pattern

Chapter 8

Discussion

8.1 Initial Observations

First we will explain some immediate observation for each of the methods.

8.1.1 Segmentation

We can see from the segmentation results (figure 7.1, figure 7.2 and figure 7.3) that the segmented surface is very close to the real surface when the surface is smooth. In areas of higher curvature, the segmented surface tend to lie inside the curve of real surface giving a smaller total curvature. This is as expected because of the level set method.

8.1.2 Shape Measurement Registration

It is clear from the images that all registrations completed successfully, except the left side takes of volunteer 2. This is because the distance based filtering failed to properly separate the hair from the actual surface. From the middle images of figure 7.8 one can see that surface areas representing the persons hair have been used, while areas representing the skin has been dropped because it's too far away. This is inhibiting the registration algorithm from recovering the final rotation. Other surfaces, like the right side scan of volunteer two show how the distance based filter is supposed to work. Here nearly all the hair has been removed, along with most of the ear and surrounding areas which is heavily deformed and moved by the hearing protection in the mr surface. Little else has been removed.

Another observation is that when there are no false surface areas, the distance threshold will remove large parts of the useful surface. This is easily seen from figure 7.4, where the filter has removed large parts of the surface for the first scan, while the second scan has a little piece of hair that allow the filter to work properly.

Finally we observe that the resulting mean distance seems better for the phantom than for the two volunteers. This is most likely because the phantom lacks hair, because it is rigid and because it does not move.

8.1.3 Tracking Device Registration

For the tracking device any noise or mispositioned points are likely to be positioned too far out, while no points ever get sampled inside the actual surface. These errors happen when the operator for some reason does not manage to keep the tracking device in contact with the patients surface at any time. When no samples are gathered with similar noise on the opposing side of the object, the resulting registration will be slightly pushed inside the object. Consider figure 7.15. The volunteer is lying on his left side, therefor more points are sampled on the right side than on the left side. No points are sampled on an opposing surface to the top of the head, for natural reasons. The end result of this is that the branch of the cross that goes to the patients left side is completely pushed inside the fixed surface, as opposed to the three others that goes both inside and outside.

8.2 Analytical View on System Accuracy

Based on the work by Fitzpatrick[7] one can safely say that the shape measurement registration has potential for a high degree of accuracy due to it's many points. There are however some drawbacks. Firstly, according to Fitzpatrick's TRE statistic, the highest accuracy should be in the mass centre of the fiducials. For the shape measurement registration this will be close to the surface of the head, while the area that need highest accuracy usually is further inside the head. This is particularly true when scanning the front of the face. The mass centre of the scanned surface will then be inside the nasal cavity, and not near the brain. The tracking device registration can however give a mass centre at any point inside the head by simply adapting the pattern used to acquire surface points. We do however not know whether the high number of points in the shape measurement registration will result in better accuracy even outside the area with maximal accuracy. This is because we have not managed to adapt Fitzpatrick's point based formulae to a surface based system.

Also, the shape measurement registration will need to registrate the tracking device coordinate system with the coordinate system of the shape measurement device. This part of the system is not yet completed, so we do not know the amount of error introduced here. Since this calculation is done in an area outside of the patient, it may dramatically move the area of highest accuracy even outside of the patient.

8.2.1 The Accuracy Metric

The accuracy metric given by the algorithm is in effect the FRE, and as stated previously, the FRE is not a good metric for registration accuracy. This is in particular true for our shape measurement registrations, because the determined overlap has a significant influence on the FRE. As can be seen from table 7.2 row one and two, when the filter sets the threshold too low the detected overlap is reduced and the resulting FRE becomes too low as well. Further, when dealing with surface based registration, the confidence in the FRE should depend on the amount of geometric constraint in the surfaces, as shown in section 3.7. This can be seen clearly in the scan of the back of the phantom (table 7.4 figure 7.14). This registration has good overlap, and low mean distance, but the near spherical shape leaves very little geometric constraint, so many other registrations results could have given equal mean distance. This is confirmed in table 7.4 where one can see that the NAI is much lower for the back scan than for the other scans.

Also worth notice is the fact that the failed registration attempt can not be detected by looking at the accuracy metric alone. Neither can it be detected by taking into account the detected overlap and the NAI. For instance the left side scan of volunteer 1 has higher mean distance and comparative overlap while still being "correct". Visual feedback in a similar form to how results are presented here should therefore be considered in a final product.

8.3 Experimental View on System Accuracy

From figure 7.31 one can see that the refinement clearly improves the target registration accuracy compared to the landmark registration. It should be mentioned that the landmark selection probably could be done with much higher accuracy by an experienced surgeon. It is therefor not possible from our tests to say that the method necessarily have high higher accuracy than a pure landmark registration, it is however possible to say that good accuracy can be achieved with less training and effort. Both figure 7.30 and figure 7.31 show that the resulting tool position on the navigation computer after registration is close enough to the surface for the yellow sphere to cross the surface of the patient in the visualisation. The sphere diameter is 8 mm. This mean that the target registration error is less than 4 mm for all the shown positions. For most is is much lower.

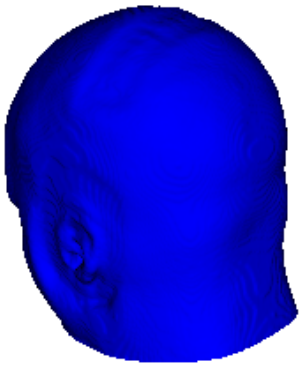

Figure 8.1: Deformations caused by hearing protection in the MR-scanner

8.4 Other Problems

8.4.1 Deformation

The outer surface of the human body is mostly soft. Although the head is usually considered rigid, even this can be affected by deformations that can affect a surface based registration. An obvious example would be facial expressions that might change between a conscious patient in the mr scanner, and a patient in full narcosis during surgery. Other causes of deformation may be caused by protection and fixation during scanning with either modality. An example is shown in figure 8.1.

Deformable registration is a topic that has gotten much attention lately[14, 20]. A proper deformable registration system should be able to overcome the problems with deformations. However a surface-based registration using deformations will have no way to say how areas except the actual surface should be deformed, therefore another source of information is most likely needed to overcome these problems. Combining the surface based registration with free-hand 3D ultrasound is believed to fill this gap[9].

8.4.2 Motion

All experiments done on volunteers were done while the person was conscious, and without any fixation. It is reasonable to believe that the volunteers have moved slightly during the data gathering. This is particularly true for the tracking device method, as this procedure took quite some time, and involved some discomfort for the volunteer. Patient motion during data gathering will result in deformations in the resulting dataset,

and this will result directly in an increase in the FRE. In a real world application, patient motion will be a problem, and a good registration system should be able to handle it. Using previous registration as initial guess[1], both registration method should be able to quickly realign provided new data are acquired for the patient after the movement. This should be particularly easy with the shape measurement device, because of it's quick scan time.

8.5 Comparison Between the Methods

It is obvious that both of the two methods discussed here have both good and bad sides. Possibly the first thing to notice is that the tracker based registration method does not reduce the amount of user interaction compared to marker based registration. The shape measurement based technique on the other hand remains fully automatic.

One possibly large drawback of the shape measurement device is that it does not work in areas covered with hair or clothing. Since most patients don't want to lose their hair unless it is absolutely necessary, this will restrain the area usable for registration with the scanner to only the face for head surgery. The tracking device should be able to sample positions at the patients scalp even with the presence of hair, at a possible reduction of accuracy.

The shape measurement device will introduce another device into the registration process, and the operating room. This device can become an additional source of error for the complete registration, and it can result in logistical problems in the operating room.

[1] provided the motion was not too big

Chapter 9

Conclusions

We have shown that using segmented surfaces from preoperative volume images can be used in patient registrations systems. Using stroked surfaces from a tracking device these can be used to improve an existing landmark registration to either improve accuracy or reduce the effort needed for an accurate registration. Using an extra shape measurement device we have shown how to create a fully automatic patient registration system. Although the resulting accuracy of such a setup has not yet been measured, it shows great promise.

We have also shown that giving a quantitative measure of the resulting accuracy is very difficult.

Chapter 10

Further Work

10.1 Speed Improvements

This section covers some of the known ways to improve speed of the registration process, that have for lack of resources not been implemented at the current stage.

10.1.1 Accelerated ICP

Besl suggests in the original ICP article a modification to the algorithm, called accelerated ICP. Based on the observation that several following iterations often move in the same direction he suggests a scheme for analysing the movement caused by following iterations, and extrapolate when the direction of the motion is compatible. Independent implementations [25] show that this can roughly reduce the time needed by a factor of 4.

10.1.2 Parallelisation

The bulk part(about 82%) of the time consumed during registration is used in finding the closest point in fixed data for each point in moving data. This part can easily be parallelised by keeping the Kd-tree structure in shared memory and allocating a given portion of the moving points to each thread of execution. With an increasing trend of placing several cpus in modern workstations, as well as new technologies such as multi-core cpus and simultaneous multithreading should allow great performance enhancement with this sort of parallelisation.

10.1.3 Off-line Kd-tree Building

Building the Kd-tree search structure is a fairly heavy task taking a noticeable part of the total registration time. Furthermore this task is only dependant on the fixed data. It should therefore be possible to complete this task off-line as a last step of the segmentation process. Alternatively it could be run simultaneously with the moving data acquisition.

10.2 Other Work

10.2.1 Filter Improvements

The filtering steps needs to be improved. Means must be taken to stop the filter from removing good parts of the surface, and to help it remove bad parts. There are several possible ways of improving the current filter: Change the time when the filter kicks in. This should probably be done adaptively when the registration is believed to be good. Including it too early could make it remove too many features from the surface either stopping the convergence or seriously delaying it. Including it too late could make the noisy areas move the registration in a wrong direction and get stuck in a local minima. This is what happened to the failed registration in our tests. Alternatively the filter could be modified to only remove connected areas at the edge of the surface. Another possibility is to find a completely new filter that works better, for instance try the statistical method, and set the threshold at mean plus two standard deviations, as suggested by [19].

10.2.2 Accuracy feedback

A quantitative measure capable of effectively separating successful registrations from failed ones is strongly desired. Ideally the measure should be quantifiable into a red-light/green-light system by selecting an appropriate minimal accuracy. As of yet none of the measures we have calculated fulfil this property. This is however related to the filter problems as described in 10.2.1. A combination of the mean distance and some measure of filter effectiveness might be suitable.

10.2.3 Data Capture Plans

For the tracker based registration, an necessary future step is to work out plans for patterns to use when capturing surface data for different uses. This can probably take advantage of Simon's work geometric constraint analysis[25, 26]. The pattern should be

easy for a human to recreate with the tracking probe, while providing enough geometric constraint for a accurate registration to be archived. Different patterns may be needed for different types of surgery, so developing these patterns, and testing them in the field will be a large task.

10.2.4 Clinical Testing

Testing the method in actual surgery has yet to be done. Also testing it on a wider range of input datasets should be done, to confirm the methods generality, and rule out that the method is over-fitted to the test data used.

Bibliography

[1] *Digital Imaging and Communications in Medicine (DICOM) Part 3: Information Object Definitions*, chapter C.7.6.2.1.1, pages 275–276. National Electrical Manufacturers Association, 2004.

[2] Edward Angle. *Interactive Computer Graphics, A Top-Down Approach Using OpenGL*, chapter 4.7–4.8, pages 184–193. Addison-Wesley, tredje edition, 2003.

[3] Sigmund Augdal. Overflatebasert registrering av volumbilder mot dybdebilder, 2004.

[4] Paul J. Besl and Neil D. McKay. A method for registration of 3d shapes. *IEEE Transaction on Pattern Analysis and Machine Intelligence*, 14(2):239–256, 1992.

[5] R. E. Ellis, D. J. Fleet, J. T. Bryant, J. Rudan, and P. Fenton. A method for evaluating ct-based surgical registration. In *Proceedings of the First Joint Conference on Computer Vision, Virtual Reality and Robotics in Medicine and Medial Robotics and Computer-Assisted Surgery*, pages 141–150, 1997.

[6] J. Michael Fitzpatrick, Derek L. G. Hill, and Jr Calvin R Maurer. *Handbook of Medical Imaging, Volume 2: Medical Image Processing and Analysis*, chapter 8. The International Society for Optical Engineering, 2004.

[7] J. Michael Fitzpatrick, Jay B. West, and Jr Calvin R Maurer. Predicting error in ridgid-body point-based registration. *IEEE Transactions on Medical Imaging*, 17(5), oktober 1998.

[8] Robert M. Haralick, Hyonam Joo, Chung-Nan Lee, Xinhua Zhuang, Vinay G. Vaidya, and Man Bae Kim. Pose estimation from corresponding point data. *Machine Vision for Inspection and Measurement*, pages 1–84, 1989.

[9] Toril A. Nagelhus Hernes, Frank Lindseth, Tormod Selbekk, Ola M. Rygh, Geir Arne Tangen, Inge Rasmussen, Arild Wollf, Ole Vegard Solberg, Erik Harg, Sigmund Augdal, Fred Couweleers, and Geirmund Unsgaard. Technological developments for improved computer assisted 3d ultrasound guided neurosurgery.

The International Journal of Medical Robotics and Computer Assisted Surgery, june 2005. Submitted for publication.

[10] Berthold K. P. Horn. Closed-form solution of absolute orientation using unit quaternions. *Journal of the Optical Society of America A*, 4:629–642, april 1987.

[11] Timothée Jost and Heinz Hügli. A multi-resolution scheme icp algorithm for fast shape registration. In *Proceedings of the First International Symposium on 3-D Processing Visualization and Transmission*, 2002.

[12] Timothée Jost and Heinz Hügli. A multi-resolution icp with heuristic closest point search for fast and robust 3d registration or range images. In *Fourth International Conference on 3-D Digital Imaging and Modeling*, 2003.

[13] Kitware Inc. *Insight Toolkit Software Guide*.

[14] Marloes M.J. Letteboer, Peter W.A Willems, Max A. Viergever, and Wiro J. Niessen. Non-rigid registration of 3d ultrasound images of brain tumors acquired during neurosurgery. 2003.

[15] William E. Lorensen and Harvey E. Cline. Marching cubes: A high resolution 3d surface construction algorithm. *ACM Computer Graphics*, 21(4):163–169, juli 1987.

[16] B. Ma, R. E. Ellis, and D. J. Fleet. Spotlights: A robust method for surface-based registration in orthopedic surgery. In *Proceedings of the International Conference on Medical-Image Computing and Computer-Assisted Intervention*, 1999.

[17] Ravikanth Malladi, James A. Sethian, and Baba C. Vemuri. Shape modeling with front propagation: A level set approach. *IEEE Transaction on Pattern Analysis and Machine Intelligence*, 17(2), februar 1995.

[18] Takeshi Masuda, Katsuhiko Sakaue, and Naokazu Yokoya. Registration and integration of multiple range images for 3-d model construction. In *Preceedings of International Conference On Pattern Recognition*, 1996.

[19] Jr. Maurer, C.R., G.B. Aboutanos, B.M. Dawant, R.J. Maciunas, and J.M. Fitzpatrick. Registration of 3-d images using weighted geometrical features. *IEEE Transactions on Medical Imaging*, 15:836–849, december 1996.

[20] Xavier Pennec, Alexis Roche, Pascal Cathier, and Nicholas Ayache. *Non-Rigid MR/US Registration for Tracking Brain Deformations*. Marcel Dekker Inc, 2005.

[21] Pietro Perona and Jitendra Malik. Scale-space and edge detection using anisotropic diffusion. *IEEE Ttransactions on Pattern Analysis and Machine Intelligence*, 12, July 1990.

[22] Szymon Rusinkiewicz and Marc Levoy. Efficient variants of the ICP algorithm. In *Proceedings of the Third Intl. Conf. on 3D Digital Imaging and Modeling*, pages 145–152, 2001.

[23] J. A. Sethian. *Level Set Methods and Fast Marching Methods*, chapter 8. Cambridge University Press, 1999.

[24] D.A. Simon, R.V. O'Toole, M. Blackwell, F. Morgan, A.M. DiGioia, and T. Kanade. Accuracy validation in image-guided orthopaedic surgery. In *Proceedings of the International Symposium on Medical Robotics and Computer Assisted Surgery*, pages 185–192, 1995.

[25] David A. Simon, Martial Herbert, and Takeo Kanade. Techniques for fast and accurate intra-surgical registration. *The Journal of Image Guded Surgery*, 1, april 1995.

[26] David A. Simon and Takeo Kanade. Geometric constraint analysis and synthesis: Methods for improving shape-based registration accuracy.

[27] Milan Sonka, Vaclav Hlavac, and Roger Boyle. *Image Processing, Analysis, and Machine Vision*, chapter 5.1.2, pages 129–130. Brooks/Cole Publishing Company, second edition, 1999.

[28] G. Turk and M. Levoy. Zippered polygon meshes from range images. In *Proeedings SIGGRAPH*, pages 311–318, 1994.

[29] S. Weik. Registration of 3-d partial surface models using luminance and depth information. In *Proceedings of the International Conference on 3-D Digital Imaging and Modeling*, pages 93–100, may 1997.

Appendix A

Article: Technological Developments for Improved Computer Assisted 3D Ultrasound Guided Neurosurgery

Submitted for publication in The International Journal of Medical Robotics and Computer Assisted Surgery, june 2005.

Technological Developments for Improved Computer Assisted 3D Ultrasound Guided Neurosurgery

Toril A. Nagelhus Hernes [1,2,3], PhD

Frank Lindseth [1,3], PhD

Tormod Selbekk [1,3], MSc

Ola M. Rygh [2,3,4], MD

Geir Arne Tangen[1,3] MSc

Inge Rasmussen [2] MD

Arild Wollf [1,3] MSc

Ole Vegard Solberg[1,3] MSc

Erik Harg [2] MSc

Sigmund Augdal [2] MSc

Fred Couweleers [1] MSc

Geirmund Unsgaard [2,3,4] PhD, MD

1) SINTEF, Trondheim, Norway
2) Norwegian University of Science and Technology, Trondheim , Norway
3) National Centre for 3D Ultrasound in Surgery, St. Olavs University Hospital, Trondheim, Norway
4) Dept of Neurosurgery, St. Olav University Hospital, Trondheim

Correspondence to:

Toril A Nagelhus Hernes

SINTEF Health Research

Dept of Medical Technology

Medical Technical Research Centre

Olav Kyrres gate 17

N-7005 Trondheim Norway

Phone: +47 93028341

Fax: +47 93070800

Email: Toril.N.Hernes@sintef.no

Word Count: 7 989

Keywords:

Intraoperative 3D ultrasound, multimodal imaging, brain shift, registration, neuronavigation, minimally invasive surgery

Abstract

The purpose of the present study was to develop and demonstrate new technological developments that we believe will be important for future neurosurgery and improved patient treatment. We have used intraoperative ultrasound imaging as a tool for solving the brain shift problem. Integrated with navigation and advanced multimodal display technologies, future possibilities for guidance of neurosurgical procedures are demonstrated. We show how advanced algorithms can make it possible to navigate and guide the procedure based on essential combined preoperative and intraoperative image information also when anatomy changes throughout the operation. New multimodal visualization technologies are demonstrated based on data acquired during neurosurgical procedures at our hospital. In conclusion, the new features demonstrate several important benefits that will help to optimize patient treatment in future neurosurgery.

INTRODUCTION

Systems for image guided surgery are now established on the neurosurgical market. Navigation systems have shown to be useful in the clinic. Surgical tools may be tracked by positioning systems and the surgeon may navigate the tools into the brain based on image information only [1-3]. Intraoperative imaging has shown to be important for obtaining improved resection and increased survival time for the patient undergoing surgery [4, 5]. The available navigation systems differ somewhat in software, positioning systems and visualization features but most of the commercial systems have practical limitations due to lack of integration with intraoperative imaging, providing the surgeon with *updated* image information. To cope with shifts that occur during surgery intraoperative imaging is needed. MR, CT and ultrasound have been presented as alternative intraoperative imaging modalities having different benefits and drawbacks in the practical clinical neurosurgical set up. All these intraoperative imaging modalities are reported to be useful for monitoring the progression of the operation, solving the brain shift problem that occur during surgery as well as for controlling the resection at the end of surgery [6-8]. In addition, examples on how intraoperative ultrasound has been used for updating preoperative images important for guidance has also been demonstrated [9, 10]. In recent years ultrasound has gained increased attention as an useful intraoperative imaging modality, due to improved image quality and relatively low price. In addition, more integrated solutions, that makes the technology user friendly and flexible has been presented [11]. In the evolution of the next generation ultrasound-based multimodal neuronavigation systems, advances in ultrasound, accuracy, registration algorithms and visualization and display techniques are important ingredients. These areas are therefore further described in this introduction:

Ultrasound imaging. A key parameter of any imaging modality used both for optimal patient diagnostics and treatment guidance, monitoring and control is the image quality. Resolution (the ability to distinguish two targets) is an important parameter for optimal image quality. 3D ultrasound image quality is related to resolution in all three directions. The spatial

resolution is in the 2D scan plane mainly determined by the frequency of the probe used. The radial (along the beam) resolution is related to the transmitted pulse length and the lateral (normal to the beam) resolution is related to the beam width (width of the main lobe at the focus). Higher frequency means better resolution, i.e. a better ability to differentiate two targets as separate objects. The drawback is loss of penetration of the ultrasound beam in the tissue with higher frequencies. Numbers on ultrasound resolution typically ranges from 0.1-1.5 mm dependent upon the probe used. One of the reasons why ultrasound image quality has improved dramatically in recent years is that the probes can be electronically tuned for a range of frequencies simultaneously. Optimal resolutions can be obtained at multiple depths, resulting in high image quality at a broad range of depths in one image. A 5MHz (4-8MHz) probe typically gives optimal image quality at a distance of 2- 6 cm from the probe. Such a probe will be suitable for most brain operations. A 10 MHz probe with optimal image quality in the near field (0.5- 4 cm) can also be used in cases where the structures (pathology) of interest are superficial.

In 3D ultrasound, resolution in all three directions is important for optimal volume quality. The image plane itself has a certain width that varies with the depth. This is the azimuth resolution (normal to the scan-plane) and is a key parameter for 3D reconstruction when many 2D frames are put together in order to form a 3D ultrasound volume. The quality of the 3D volumes is therefore determined by the quality of the 2D images and the way 3D reconstruction is performed. Various algorithms for ultrasound 3D reconstruction exist and they differ in speed and quality of the final generated volume [12, 13]. The resolution in the azimuth direction can also be improved by 1.5 D probes, and new real time 3D probes can simplify the acquisition of high resolution volumes. This opens for even more flexible use of ultrasound in neuronavigation. In addition, new features of ultrasound imaging such as blood flow imaging and strain imaging might give important information during both vascular and tumor neurosurgery [14, 15].

Registration. In neuronavigation several steps demand some kind of registration. The objective of registration is to establish a geometric transformation between two

representations (images or corresponding points) of the same physical object. It is common to distinguish between *image to image* registration and *image to patient* registration. Multimodal registration makes it possible to combine structural (MRI, CT) and functional (fMRI, PET, SPECT, tractograms, MRA) information for diagnosis and surgical planning from various imaging modalities. By comparing images acquired at different times (usually from the same imaging modality) registration is further used for monitoring progression of a disease, controlling of a surgical procedure and for postoperative follow up. Registration of preoperative images to the patient is a required step in any neuronavigation system using preoperative images. Most registration methods can be characterized as point-based, surface-based or volume-based [16, 17]. Point-based methods optimize the alignment of corresponding points in two images or in one image and in physical space and are used in neuronavigation system using skull fiducials, skin fiducials or anatomical landmarks as points. Surface-based registration methods are used in commercial systems. These methods try to match surfaces extracted from the image data with corresponding surfaces generated from physical space using a tracked pointer or a laser device [18-22]. Volume-based methods are used for registration of two volumes by optimizing their correlation or mutual information.

Accuracy in neuronavigation. An important parameter in computer assisted navigated neurosurgery is the *overall clinical accuracy* of the system being used. That means how accurately the surgeon can navigate the tip of a surgical instrument inside the brain by means of the image information, which is provided on the navigation monitor. The overall clinical accuracy is hence the difference between the location of a surgical tool as indicated in the image presented to the surgeon and where the tool tip is physically located in the patient. The better the accuracy, the more delicate and precise work can be performed. Numbers on *overall clinical accuracy* are practically impossible to measure because they depend not only on the navigation system, but also on patient preparation procedures, system setup, and system handling. The various steps in the preparation for and use of neuronavigation will hence affect the over all accuracy of a system. In summary, the steps in neuronavigation are: 1) Preoperative image acquisition and planning of therapy. 2) Patient registration and

planning in the operating room. 3) Intraoperative image acquisition, visualization and navigation/guidance (repeated several times) and control. 4) Possible postoperative data acquisition and evaluation. Several groups have described error sources associated with the various steps and use of neuronavigation in surgery [23-25]. For systems based on preoperative images, the errors are mainly caused by registration errors of preoperative images to the patients and by brain shifts that occur during therapy. For systems using intraoperative imaging, the brain shift errors are minimized due to updates of the map for guidance. For some of these systems, the intraoperative images, such as MR and CT must be registrated to the patient in the operating room [26], so the registration error is still present in the range of 2-3mm. For ultrasound-based systems, no registration is required since the ultrasound images are acquired directly in the same coordinate system as navigation is performed. The accuracy will be dependent upon the calibration of the ultrasound probe and the 3D reconstruction algorithm, typically in the range of 1-2 mm as described [25].

Visualization and display. In the litterature there are various ways to classify the different visualization techniques that exist. For medical visualization of 3D data from modalities like CT, MRI and ultrasound it is common to refer to three different approaches; *slicing, volume rendering and geometric (surface/polygon/triangle) rendering.* Slicing methods can be further sub-classed based on how the 2D slice data is generated and how this information is displayed. From the reconstructed volume we can extract both *orthogonal* and *oblique* slices (Figure 1). Orthogonal slicing is often used in systems for pre- and post-operative visualization, as well as in intra-operative navigation systems, where the tip of the tracked instrument determines the three extracted slices. The orthogonal slices may be relative to the orientation of the tracked instrument, the patient or the direction of the surgeons view (i.e. oblique slicing relative to the volume axis).

Volume- and geometric rendering techniques can produce similar visualization of 3D data, and in some cases one approach may be considered both a volume rendering and a geometric rendering technique. Still, volume rendering is a term used to describe a direct rendering process applied to 3D data where information exists throughout a 3D space instead of simply

on 2D surfaces defined in (and often extracted from) such a 3D space [27]. The two most common approaches to volume rendering are volumetric ray casting and 2D texture mapping. In ray casting each pixel in the image is determined by sending a ray into the volume and evaluate the voxel-data encountered along the ray using a specified ray-function (maximum, isovalue, compositing). Using 2D texture mapping, quads are generated along the axis of the volume that is most closely aligned with the viewing direction. The data is then mapped onto these polygons and projected into a picture using standard graphics hardware. The technique used to render the texture-mapped quads is essentially the same technique that is used to render geometric surface representations of relevant structures. In order to render geometric surfaces, the geometric representations from the image information must be generated, usually by some kind of segmentation algorithm.

Image fusion techniques might be beneficial when using the best of both MRI and ultrasound because it is easier to perceive an integration of two or more volumes in the same scene than mentally fusing the same volumes presented in their own windows. It also gives the opportunity to pick relevant and needed information from the most appropriate of the available datasets. Ideally, relevant information should include not only anatomical structures for reference and pathological structures to be targeted, but also important structures to be avoided.

In this paper we describe technology that we have developed and tested on clinical data for planning, guidance and evaluation. We have focused on areas in computer assisted neurosurgery, that we believe will be essential and important for achieving optimal patient treatment in the future. Improvement of intraoperative ultrasound due to its low cost, flexible usefulness and improved image quality has now made this imaging modality more attractive for neurosurgical applications. We demonstrate how combined usage of preoperative information and intraoperatively acquired data can solve the brain shift problem and enables efficient use of important preoperative information (e.g. fMRI) throughout the operation. We show how improvements demonstrated by developed prototype technologies, may affect clinical usage and open for future solutions in computer assisted therapy.

MATERIALS AND METHODS

Navigation software for future computer assisted guidance. A new prototype module-based navigation technology platform (CustusX, SINTEF, Trondheim, Norway) demonstrates new features in future neuronavigation. The system combines visualization of image data from CT, MR and intraoperative 2D and reconstructed 3D ultrasound and real-time endoscope/camera images. The complete system (Figure 2) consists of a computer (Macintosh 1.25Ghz PowerPC G4, Apple, Cupertino, CA, USA), magnetic or optical positioning system (Polaris or Aurora, NDI, Waterloo, Ontario, Canada or MiniBIRD, Ascension Technologies, Burlington, USA), navigation, image processing and visualization software (SINTEF, Trondheim, Norway), cameras (e.g., stand-alone, microscope or endoscope), and an integrate with ultrasound system with probes (various US-scanners). Conventional display techniques as orthogonal and oblique (anyplane) slicing can be used (Figure 1). Data available to the surgeon can be presented in a single 3D scene with fusion of the various coregistrated data sets. Real-time data from endoscopes as well as ultrasound probes can be correctly positioned into the 3D scene. There is also the opportunity to exclude information and to make occluding objects transparent. The software displays the preoperative or intraoperative 3D data as volumes together with surfaces of segmented objects in combination with slices (see below). Miscellaneous surgical instruments can be used in the navigation system, such as CUSA, biopsy forceps or other important equipment. Also flexible instruments can be used in combination with micropositioning systems. Models of the instruments can be displayed in correct positions in the 3D scene. The images are displayed with real-time tracking of the operator's instruments during planning or surgery guidance. Positions of biopsies can be marked and color set due to histo-pathological evaluation during surgery. Position tracking of the instruments can be turned off to allow manual inspection such as rotation and zooming of the 3D scene, which may be important for improved overview and interpretation during planning, guidance and control of the procedure.

Integrated display of surface and volume rendering from overlapping multimodal volumes. Volume rendering techniques and geometric rendering techniques can be used in combination with slicing methods as well as stereoscopic views in our prototype system. Volume rendering of multiple volumes in the same 3D scene with real time individual setting of the color transfer functions are supported, using the shader functionality offered by todays computer graphic cards. In order to be able to volume render multiple overlapping volumes properly, textures from all individual volumes are sorted together. This makes it possible to simultaneously volume render data from different imaging modalities with various size and resolution. In addition, high resolution volumes can be rendered in areas of special interest, whereas low resolution volumes (resampled) can be displayed in other areas for improved overview. This flexibility will fasten the interaction with the multivolume 3D data and makes it possible to navigate in real time based on the 3D data. Various semi- automatic segmentation algorithms are used in the system for generating geometric models of structures to be displayed in the 3D scene. The methods implemented, range from simple thresholding and region growing algorithms to more advanced methods like level-set segmentation features [28]. The parameter settings vary among the segmentation methods, which again are chosen due to the structure to be extracted. The segmentation result should be verified and manually edited when required. From the segmentation results a surface model was generated using the marching cube algorithm [29].

Markerless registration of the patient. Prototype technology for markerless registration of the patient in the operating room was developed. The method is based on matching a surface model extracted from preoperative MRI data of the head to a corresponding surface generated from the patient in the operating room using a structured light measuring technique. The registration of the two surfaces was performed using a modified version of the iterative closest point algorithm [30]. Starting from an initial transform between the segmented preoperative surface from MRI and the structured light generated intraoperative surface, the basic principle of the ICP algorithm is to: 1) find the closest point on the preoperative surface for each of the points in the intraoperative surface, 2) to calculate a new and better transform

based on all the corresponding point pairs, and 3) to terminate the iteration when some sort of stop criteria is met. Whereas the preoperative surface model is extracted and generated from MRI data using a fast marching level set algorithm [28] followed by the marching cubes algorithm, the intraoperative surface is generated using a structured light measurement technique. The method is based on illuminating the object of interest with a sequence of light patterns and observing the resulting scenes with a camera. From the observed scenes, co-ordinates of many points, distributed across the surface of the object, can be derived. This so-called "point cloud" is then modelled using multi-level B-spline approximation to give a surface description of the object that can be registered to the corresponding segmented surface.

Volume to volume registration for updating preoperative data based on intraoperative ultrasound: A software module for coregistration of preoperative data sets from MRI and intraoperative ultrasound were developed based on a three step approach to the problem. First, all the different preoperative MRI volumes are registered to a master MRI volume for multimodal preoperative planning. After preoperative data (master MRI volume) to patient registration is performed the master volume is registered to one of the ultrasound volumes acquired from dura mater (initial US volume) (step two). If the patient registration process is accurate and no brain shift has occurred at this stage in the operation the master MRI to initial US volume registration would be close to identity, however this is seldom the case. The third step is then to track the changes that occur during surgery by registering subsequent US volumes to the previous one and apply the detected changes to the preoperative data. Step one and two is based on rigid registration, while a non rigid method is used for step three. Registration algorithms based on mutual information [31, 32] is used for all three steps. Both tissue and angio data can be used for step two and three.

Patient image data used for demonstrating future technological solutions in ultrasound based neuronavigation: Image data was acquired from patients undergoing various neurosurgical procedures like brain tumor resections, clipping aneurysms or cyst drainages. Preoperative

3D MR images with high resolution (Picker or Siemens 1.5 T and Phillips 3T) and a slice thickness of 1.0 mm were acquired the day before surgery. Protocols for the various MR acquisitions (MR T1, MR T2, MRA, fMRI) were used. A prototype system utilizing features of navigation technology and intraoperative 3D ultrasound was originally developed within our research group. The commercial version of this system (SonoWand, MISON AS, Trondheim, Norway) was used during neurosurgical procedures for intraoperative 3D ultrasound image acquisition and registration of preoperative images to the patient using fiducial markers [11]. 3D tissue images as well as MR angiographies and fMRI were registrated to the patient and hence put in the same coordinate system as ultrasound acquisition was performed (Figure 3, Operation set up). A 4-8 MHz Flat Phased Array (FPA) ultrasound probe with optimal focusing properties at 3-6 cm was moved by free hand over the anatomical area of interest. The acquired 3D data sets were transferred to the navigation computer and reconstructed to a 3D volume. No patient registration was needed for the 3D ultrasound volumes since they were acquired in the same coordinate system as navigation was performed. All coregistrated images (preoperative data and intraoperative ultrasound data) were exported from the SonoWand system and imported into our prototype neuronavigation system after surgery. New technological features and clinical applications in neuronavigation were then demonstrated. Also data from healthy persons not undergoing surgery was used for development, testing and improving prototype technology.

RESULTS, - NEW DEVELOPMENTS IN COMPUTER ASSISTED NEUROSURGERY

Efficient and safe guidance using tracked surgical equipments. Clinical testing and simulation based on image data from preoperative MR and intraoperative ultrasound acquired before and during surgery, disclosed new possibilities when tracking devices were put directly on the surgical tools and not only on pointers and probes. Especially, tracking of CUSA and biopsy forceps made it possible to guide the surgical procedure directly and perform efficient and safe guidance simultaneously without spending time and effort on changing instrument when navigation was needed.

Improved image quality makes ultrasound a promising brain shift solver in future neuronavigation. Intraoperative ultrasound has improved dramatically in recent years especially due to better image quality. An image quality that was close to the quality of MRI was demonstrated during surgery (Figure 4). Intraoperative ultrasound was powerful for following the resection and update changes that occurred during surgery. Especially, 3D ultrasound imaging made it possible to guide surgical equipment based on correct and updated image information. Navigated 2D/3D ultrasound imaging in combination with other relevant 3D data improved the orientation and interpretation of ultrasound images as shown in figure 5-7. Integration with navigation technology made ultrasound more userfriendly and flexible in the clinic.

Userfriendly display using combined volume rendering, surface rendering and slicing. New visualization software made it possible to extract information and display information from an image volume in various ways. Our new software made it easier to add 3D objects in combination with slices from the volumes. Information from a volume could be displayed using various visualization techniques as shown in figure 5. Especially, technology for displaying multiple overlapping volume rendered objects simultaneously in one 3D scene made it easier to interpret 3D information from several volumes without preprocessing the

data. This technology made it possible to detect brain shift immediately after a new ultrasound volume was acquired as well as improving interpretation and orientation of ultrasound data, not covering the whole brain (Figure 6). In addition, geometric models were sometimes useful for displaying important anatomy as localization of fMRI and vessels as shown in figure 5. In addition, information from different image volumes could be displayed simultaneously using different techniques in one window as demonstrated by a brain tumor case (Figure 5). Here, the display of MRI, MRA, fMRI and intraoperative ultrasound angiography and tissue data made it easier to interpret specific localization of structures and brain shift. Essential information was displayed and unneccessary information was removed, hence developing a userfriendly 3D scene for guidance and control. 2D slices displayed in separate windows made it easier to interpret more detailed information. Visualization of a 2D slice in a 3D scene improved the understanding of orientation and localization of the 2D slice due to surrounding anatomy. When intraoperative images were displayed in the same 3D scene as preoperative information, brain shift could be observed as shown in figure 5. Here, a shift between preoperative MRA and intraoperative ultrasound angiography was easily detected. The knowledge of the exact position of surrounding vessels and functional areas was important for satisfactory surgical outcome. In our study a shift in tumor and vessel position was detected by intraoperative ultrasound. Thus also indicating a possible shift in functional areas in the brain (Figure 5).

Updating and repositioning essential preoperative images due to changes that occur during surgery. New advanced and automatic volume to volume registration algorithms made it possible to correct for changes that occurred during surgery. We have demonstrated the algorithm using preoperative MRA (Figure 6a) and intraoperative ultrasound angiography (Figure 6b). Multimodal display showed a shift (Figure 6c). The automatic volume to volume registration algorithm moved the preoperative information to the correct position (Figure 6d). When implemented in clinical use, this feature would make it easier for the surgeon to trust the location of important preoperative information as vessel position surrounding the area of interest. This may be especially important for fMRI data, which frequently is not possible to

acquire intraoperatively.

Intraoperative ultrasound, multimodal and equipment visualization. When ultrasound imaging was separately displayed in a single window, essential details were easily interpreted. However, in many cases more information about surrounding anatomy as well as a demand for solving the orientation problem with ultrasound was needed. Both these challenges were solved by displaying ultrasound and MR volumes together as shown in figure 7. Here, the MR images (as slices or volumes) were displayed in combination with available intraoperative ultrasound, obtaining better overview and improved orientation. A virtual sector of the ultrasound image plane to be acquired, we believe can help positioning the craniotomy in a convenient place for optimal imaging and patient outcome. In addition, visualization of the surgical instruments or probes can improve orientation and real time surgical guidance.

Integration of online pathological data for improved surgery. During brain tumor surgery some surgeons prefer to take several biopsies in order to improve the quality of surgery. Features in future navigation systems will take care of the biopsy positions and mark the histo-pathological output when the information of the biopsy status arrives in the operating room from the pathology department. The feature is demonstrated on data from a patient undergoing tumor surgery. Simulated biopsies acquired during surgery were marked yellow (Figure 7E). Biopsies with tumor tissue were marked red, making it possible for the surgeon to navigate the surgical instrument into place for removal of rest tumor tissue. Biopsies with normal tissue, or without tumor tissue were marked green in the 3D scene (Figure 7F). The brain shift occurring just after opening the cranium is severe and will also affect the biopsy results. In figure 7 it is demonstrated how intraoperative ultrasound is more in correspondance with simulated histo-pathological data from biopsies than preoperative MRI due to delineation of position of tumor border, even before surgery has started. This display, we believe, will improve the efficiency of surgery and makes it easier for the surgeon to perform total resection in cases where this is recommended.

Easy markerless patient registation. Although intraoperative ultrasound gives important updated information in neurosurgery, preoperatively acquired data as fMRI and tractograms are useful for planning and guidance. Our markerless registration algorithm enables automatic and easy registration of preoperative images to the patient (Figure 8). Our test was performed on a healthy person. The algorithm performed registration in seconds, was accurate and userfriendly. If integrated into clinical practice, the patient no longer need to have fiducial markers during preoperative MR scanning. We believe that this technology will fasten the total procedure and makes it convenient for the patient and the hospital personnel to handle the patient and the logistics related to usage of preoperative data in neuronavigation.

DISCUSSION

Technological developments open for new possibilities in treatment of tumors and vascular lesions in the brain. Ultrasound has also by other authors been introduced as a technology that solves one of the most challenging tasks in navigated neurosurgery; the brain shift problem [33-36]. Increased data power, better resolution and image quality as well as real time capabilities and advanced multimodal display will make future ultrasound technology even more userfriendly and optimized for efficient patient treatment than demonstrated today. New ultrasound technology and probe developments with higher frequencies will open for improved delineation of tumor borders, more accurate resection control as well as easier interpretation of information in the future. Sophisticated signal processing algorithms also open for new ways of extracting valuable information useful both in diagnostics and guidance of neurosurgery. Ultrasound strain imaging that already is being used for diagnostics of the heart [37, 38] might give more real time information for delineation of tumor during the procedure [39] (Figure 9). Ultrasound has also been found efficient as the only imaging modality for guiding of endoscopes [40, 41] and evacuation of hematomas [42]. Although ultrasound in tumor surgery is found adequate for guidance and resection control alone or in combination with preoperative images in neuronavigation [43-47], ultrasound has an additional potential for updating essential preoperative information from fMRI and other important information as demonstrated in the present paper. Our volume to volume registration algorithm could in some cases make it unnecessary to display intraoperative ultrasound as in the case shown in figure 6. However, our experiences are that in more complex cases, especially in tumor cases where tumor borders are difficult to interpret, automatic solutions may be erroneous. Therefore, a professional user of navigation systems using automatic MRI-updating based on intraoperative ultrasound, should for safety reasons be able to interpret ultrasound as well as MRI. We believe that warping algorithms for correction of changes that occur during surgery will emerge in commercial systems in the future. Other research groups have demonstrated reasonable results based on ultrasound for warping preoperative data [9]. Hence, new and selected information useful for optimal patient

treatment will be available in future operating rooms. An important information, valuable for improved image guidance in neurosurgery, is diffusion-tensor (DT) imaging–based tractography (Figure 10). Collaboration between radiologists, technologists and surgeons will make it possible to integrate also this information into the operating room in our hospital (feasibility tests already performed). This technology might give important information trying to preserve brain functions while maximizing the extent of tumor resection for prolonging survival as well as maintaining quality of life for patients. An important technological future aspect of this is not only to be able to integrate this information into the navigation system, but also to adjust these tractograms so they reflect the true positions during progression of the tumor resection when tissue changes (work in progress). Lately, several research groups have introduced diffusion-tensor (DT) imaging–based tractography in neuronavigation with the intention of more accurate and safe surgery guidance with improved patient outcome [48, 49]. Future work will use intraoperative ultrasound for updating important preoperative information from both tractograms and fMRI due to changes occurring during surgery.

Other sources of important information are also available during surgical procedures. Microscopes are frequently in use, but represent a challenge in combination with navigation technology. Other sources of information are endocopes, used for example during fenestration of cysts, and future High Definition (HD) camera, that also may provide important information. Optical tracking systems based on visual light will generate images as conventional cameras. Information from all these sources should be fused together with the radiological information used in the navigation systems, independently of where the fused 3D scene is displayed; on a monitor or for example in the ocular of the microscope. We have experienced that it is convenient to guide the surgical procedure with instrument tracking and images displayed on the monitor. A demonstration of an augmented reality display, fusing the camera/video image with 3D radiological data used in the navigation system, is presented (Figure 11). A similar view can be projected down to the patient or in the ocular of the microscope. This solution will equip the surgeon with supervision that in combination with advanced haptics and new tumorsensor technology will help the surgeon obtaining optimal patient treatment. Several instruments and probes may be tracked simultaneously, making it

possible to both acquiring real time data and interacting in real time with this updated 3D multimodality view.

CONCLUSION

In the present paper we have demonstrated new technological features for future computer assisted neuronavigation that are tested on data acquired in the clinic. We believe that new technology and increased computer power will optimize the solutions so they can meet the requirements for improved quality of patient treatment, increased efficiency, userfriendliness and flexibility in the clinic. The improved image quality and low cost of ultrasound makes the technology an attractive platform for solving the brain shift problem and for displaying real time updates of essential intraoperative and preoperative information. Although feasibility studies have demonstrated usefulness of new technology in the clinic, further work must be performed on effect on integration of new technology into clinical practice. Especially, clinical trials involving more patients must be performed.

ACKNOWLEDGEMENT

This work was supported by The Norwegian University of Science and Technology through Strategic University Program for Medical Technology, SINTEF through Strategic Institute Program, Research Council of Norway (NFR) through the FIFOS program project 152831/530, Ministry of Health and Social Affairs of Norway. We also want to thank Jon Bang, Reidar Brekken, Jon Harald Kaspersen and Svein Winther, scientists at SINTEF and neurosurgeons Tomm Muller and Frode Kolstad and Prof radiologist Kjell Arne Kvistad at St Olavs University Hospital for valuable discussions and collaboration during the work. In addition we want to thank Professor Olav Haraldseth, Erik Berntsen and Jian Xu at the Inst at Circulation of Medical Imaging, Medical Faculty at Norwegian University of Science and Technology.

REFERENCES

1. Kurtsoy A, Menku A, Tucer B, Oktem IS, Akdemir H. Neuronavigation in skull base tumors. Minimally Invasive Neurosurgery 2005;48(1):7-12.
2. Gumprecht HK, Widenka DC, Lumenta CB. BrainLab VectorVision Neuronavigation System: Technology and Clinical Experiences in 131 Cases Neurosurgery 1999;44(1):97-105.
3. Wirtz CR, Albert FK, Schwaderer M, Heuer C, Staubert A, Tronnier VM, Knauth M, Kunze S. The benefit of neuronavigation for neurosurgery analyzed by its impact on glioblastoma surgery. Neurological Research 2000;22(June):354-360.
4. Knauth M, Wirtz CR, Tronnier VM, Aras N, Kunze S, Sartor K. Intraoperative MR Imaging Increases the Extent of Tumor Resection in Patients with High-Grade Gliomas. AJNR Am J Neororadiol 1999;20:1642-1646.
5. Wirtz CR, Knauth M, Staubert A, Bonsanto MM, Sartor K, Kunze S, Tronnier VM. Clinical Evaluation and Follow-up Results for Intraoperative Magnetic Resonance Imaging in Neurosurgery. Neurosurgery 2000;46(5):1112-1122.
6. Grunert P, Müller-Forsell W, Darabi K, Reisch R, Busert C, Hopf N, Perneczky A. Basic Principles and Clinical Applications of Neuronavigation and Intraoperative Computed Tomography. Computer Aided Surgery 1998;3:166-173.
7. Albayrak B, Samdani AF, Black PM. Intra-operative magnetic resonance imaging in neurosurgery. Acta Neurochirurgica 2004;146(6):543-557.
8. Hammoud MA, Ligon BL, ElSouki R, Shi WM, Shomer DF, Sawaya R. Use of intraoperative ultrasound for localizing tumors and determening the extent of resection: a comparative study with magnetic resonance imaging. J. Neurosurg 1996;84(May):737-741.

9. Bucholz RD, Yeh DD, Trobaugh J, McDurmont LL, Sturm CD, Baumann C, Henderson JM, Levy A, Kessman P. The correction of stereotactic inaccuracy caused by brain shift using an intraoperative ultrasound device. *Cvrmed-Mrcas'97*, 1997:459-466.

10. Comeau RM, Sadikot AF, Fenster A, Peters TM. Intraoperative ultrasound for guidance and tissue shift correction in image-guided neurosurgery. Med. Phys. 2000;27(4):787-800.

11. Gronningsaeter A, Kleven A, Ommedal S, Aarseth TE, Lie T, Lindseth F, Lango T, Unsgard G. SonoWand, an ultrasound-based neuronavigation system. Neurosurgery 2000;47(6):1373-1379.

12. Rohling R, Gee A, Berman L. A comparison of freehand three-dimensional ultrasound reconstruction techniques. Medical Image Analysis 1999;3(4):339-359.

13. Estepar RS, Martin-Fernandez M, Alberola-Lopez C, Ellsmere J, Kikinis R, Westin CF. Freehand ultrasound reconstruction based on ROI prior modeling and normalized convolution. *Medical Image Computing and Computer-Assisted Intervention - Miccai 2003, Pt 2*, 2003:382-390.

14. Unsgaard G, Ommedal S, Muller T, Gronningsaeter A, Hernes TAN. Neuronavigation by Intraoperative three-dimensional ultrasound: Initial experience during brain tumor resection. Neurosurgery 2002;50(4):804-812.

15. Unsgaard G, Ommedal S, Rygh O, Lindseth F. Operation of AVMs assisted by stereoscopic navigation–controlled display of preoperative MR angiography and intraoperative ultrasound angiography. Neurosurgery 2005;56(4):S2:281-290.

16. Hajnal JV, Hawkes DJ, Hill DLG, editors. Medical Image Registration: CRC Press, 2001.

17. Maintz JBA, Viergever MA. A survey of medical image registration. Medical Image Analysis 1998;2(1):1-36.

18. Sun H, Farid H, Roberts DW, Rick K, Hartov A, Paulsen KD. A noncontacting 3-D digitizer for use in image-guided neurosurgery. Stereotactic and Functional Neurosurgery 2003;80(1-4):120-124.

19. Marmulla R, Muhling J, Wirtz CR, Hassfeld S. High-resolution laser surface scanning for patient registration in cranial computer-assisted surgery. Minimally Invasive Neurosurgery 2004;47(2):72-78.

20. Maurer CR, Fitzpatrick JM, Wang MY, Galloway RL, Maciunas RJ, Allen GS. Registration of head volume images using implantable fiducial markers. Ieee Transactions on Medical Imaging 1997;16(4):447-462.

21. Hoffmann J, Westendorff C, Leitner C, Bartz D, Reinert S. Validation of 3D-laser surface registration for image-guided cranio-maxillofacial surgery. Journal of Cranio-Maxillofacial Surgery 2005;33(1):13-18.

22. Raabe A, Krishnan R, Wolff R, Hermann E, Zimmermann M, Seifert V. Laser surface scanning for patient registration in intracranial image-guided surgery. Neurosurgery 2002;50(4):797-801.

23. Steinmeier R, Rachinger J, Kaus M, Ganslandt O, Huk W, Fahlbusch R. Factors influencing the application accuracy of neuronavigation systems. Stereotactic and Functional Neurosurgery 2000;75(4):188-202.

24. Poggi S, Pallotta S, Russo S, Gallina P, Torresin A, Bucciolini M. Neuronavigation accuracy dependence on CT and MR imaging parameters: a phantom-based study. Physics in Medicine and Biology 2003;48(14):2199-2216.

25. Lindseth F, Langø T, Bang J, Nagelhus Hernes TA. Accuracy Evaluation of a 3D Ultrasound–Based Neuronavigation System. Computer Aided Surgery 2002;7:197-222.

26. Wirtz CR, Bonsanto MM, Knauth M, Tronnier VM, Albert FK, Staubert A, Kunze S. Intraoperative Magnetic Resonance Imaging To Update Interactive Navigation in Neurosurgery: Method and Preliminary Experience. Computer Aided Surgery 1997;2:172-179.

27. Schroeder W, Martin K, Lorensen B. The visualization toolkit : an object-oriented approach to 3D graphics. 2 ed: Prentice Hall, 1997.

28. Sethian JA. Level set methods and fast marching methods : evolving interfaces in computational geometry, fluid mechanics, computer vision, and materials science. Cambridge: Cambridge University Press, 1999.

29. Lorensen WE, Cline HE. Marching Cubes: A High Resolution 3D Surface Construction Algorithme. Computer Graphics 1987;21:163-169.

30. Besl PJ, McKay ND. A Method for Registration of 3-D Shapes. Ieee Transactions on Pattern Analysis and Machine Intelligence 1992;14(2):239-256.

31. Maes F, Vandermeulen D, Suetens P. Medical image registration using mutual information. Proceedings of the Ieee 2003;91(10):1699-1722.

32. Viola P, Wells WM. Alignment by maximization of mutual information. International Journal of Computer Vision 1997;24(2):137-154.

33. Hill DLG, Maurer CR, Maciunas RJ, Barwise JA, Fitzpatrick JM, Wang MY. Measurement of Intraoperative Brain Surface Deformation under a Craniotomy. Neurosurgery 1998;43(3):514-528.

34. Trantakis C, Tittgemeyer M, Schneider JP, Lindner D, Winkler D, Strauss G, Meixensberger J. Investigation of time-dependency of intracranial brain shift and its relation to the extent of tumor removal using intra-operative MRI. Neurological Research 2003;25(1):9-12.

35. Letteboer MMJ, Willems PWA, Viergever MA, Niessen WJ. Brain shift estimation in image-guided neurosurgery using 3-D ultrasound. Ieee Transactions on Biomedical Engineering 2005;52(2):268-276.

36. Reinges MHT, Nguyen HH, Krings T, Hutter BO, Rohde V, Gilsbach JM. Course of brain shift during microsurgical resection of supratentorial cerebral lesions: limits of conventional neuronavigation. Acta Neurochirurgica 2004;146(4):369-377.

37. Heimdal A, Stoylen A, Torp H, Skjaerpe T. Real-time strain rate imaging of the left ventricle by ultrasound. Journal of the American Society of Echocardiography 1998;11(11):1013-1019.

38. D'Hooge J, Bijnens B, Thoen J, Van de Werf F, Sutherland GR, Suetens P. Echocardiographic strain and strain-rate imaging: A new tool to study regional myocardial function. Ieee Transactions on Medical Imaging 2002;21(9):1022-1030.

39. Selbekk T, Bang J, Unsgaard G. Strain processing of intraoperative ultrasound images of brain tumours: Initial results. Ultrasound in Medicine & Biology 2005;31(1):45-51.

40. Auer LM. Ultrasound stereotaxic endoscopy in neurosurgery. Acta Neurochir Suppl (Wien) 1992;54:34-41.

41. Yamakawa K, Kondo T, Yoshioka M, Takakura K. Ultrasound guided endoscopic neurosurgery--new surgical instrument and technique. Acta Neurochir Suppl 1994;61:46-8.

42. Unsgaard G, Gronningsaeter A, Ommedal S, Hernes TAN. Brain operations guided by real-time two-dimensional ultrasound: New possibilities as a result of improved image quality. Neurosurgery 2002;51(2):402-411.

43. Nikas DC, Hartov A, Lunn K, Rick K, Paulsen K, Roberts DW. Coregistered intraoperative ultrasonography in resection of malignant glioma. Neurosurg Focus 2003;14(2):Article 6.

44. Trantakis C, Meixensberger J, Lindner D, Strauss G, Grunst G, Schmidtgen A, Arnold S. Iterative neuronavigation using 3D ultrasound. A feasibility study. Neurological Research 2002;24(7):666-670.

45. Unsgaard G, Ommedal S, Muller T, Gronningsaeter A, Nagelhus Hernes TA. Neuronavigation by intraoperative three-dimensional ultrasound: Initial experience during brain tumor resection. Neurosurgery 2002;50(4):804-812.

46. Bonsanto MM, Staubert A, Wirtz CR, Tronnier V, Kunze S. Initial Experience with an Ultrasound-Integrated Single-Rack Neuronavigation System. Acta Neurochir (Wien) 2001;143:1127-1132.

47. Hernes TAN, Ommedal S, Lie T, Lindseth F, Langø T, Unsgaard G. Stereoscopic navigation-controlled display of preoperative MRI and intraoperative 3D ultrasound in planning and guidance of neurosurgery - New technology for minimally invasive image guided surgery approaches. Minim Invasive Neurosurg 2003;46:129-137.

48. Kamada K, Todo T, Masutani Y, Aoki S, Ino K, Takano T, Kirino T, Kawahara N, Morita A. Combined use of tractography-integrated functional neuronavigation and direct fiber stimulation. Journal of Neurosurgery 2005;102(4):664-672.

49. Rohde V, Spangenberg P, Mayfrank L, Reinges M, Gilsbach JM, Coenen VA. Advanced neuronavigation in skull base tumors and vascular lesions. Minimally Invasive Neurosurgery 2005;48(1):13-18.

FIGURE LEGENDS

Figure 1. Various display techniques can be used for guiding surgical procedures. A single 2D slice selected from the 3D volume due to the position of the instrument can be displayed (**A**: anyplane), or three orthogonal slices (**B**) can be selected due to the position and orientation of the surgical tool and due to the patient. Various 3D visualization techniques using volume rendering or surface rendering of models or objects can be used (**C**). The slicing and 3D display techniques can also be used simultaneously in one window/3D scene (**D**). Geometric models of instruments and probes can be visualized in correct position in the same 3D scene as radiological data (**C,D**).

Figure 2. The new platform for navigated surgery (**A**) can be used with an optical (**A**) or a magnetic (**B**) tracking system. In future neuronavigation systems all surgical instruments, rigid or flexible, can be tracked by position systems and hence the instruments can be directly used to control the display of images used for guidance. Here demonstrated by positioning sensors (reflecting spheres) on a pointer (**C**), biopsy forceps (**D**), endoscope (**E**), CUSA (**F**), ultrasound probe (**G**). Some of the instruments are used both in the SonoWand system and in own developed navigation system.

Figure 3. Set up in the operating room. The patient reference frame is attached to the rigid head holder. Planning based on preoperative MRI is performed using a pointer. Ultrasound acquisition is performed in the same coordinate system as navigation is performed. Two monitors are used, one for ultrasound image visualization and the other for navigation.

Figure 4. Technological developments have improved image quality of ultrasound imaging to become comparable to the quality of MRI as demonstrated on a patient with brain tumor. Corresponding slices from preoperative MRI (**A**) and intraoperative ultrasound before surgery (**B**) and intraoperative ultrasound after some resection of the tumor (**C**) are shown. Anatomical structures can easily be interpreted in MRI and also in the ultrasound image both before and after some resection.

Figure 5. Combination of techniques for 2D and 3D visualization. In figure **A**, preoperative MRI (grey scale), the segmented tumor (pink, surface rendered) from preoperative MRI, MRA (red, surface rendered), fMRI (yellow, surface rendered) from the tongue are displayed together with intraoperative ultrasound angiography (green, surface rendered) acquired from a patient with brain tumor. Intraoperative 3D ultrasound angiography showed a different location of vessels than preoperative MR. The differences in display was probably due to shift in the brain before surgery has even started as well as some registration errors of the preoperative data. In **B** additional 3D ultrasound tissue imaging shows that the shift easily also can be identified in other areas surrounding the tumor. Shift is hence detected on both the angiography data and on the tissue data and most likely, the positioning of the functional area as displayed was erroneous as well.

Figure 6. Advanced automatic volume to volume registration algorithm for updating preoperative MRI data based on intraoperative ultrasound. All data is from a patient with an aneurysm. Volume rendering of preoperative MRA (**A**, red), corresponding volume rendering of intraoperative ultrasound angiography (**B**, green) and simultaneous multimodal volume rendering of preoperative MRI (red) and intraoperative ultrasound (green) (**C**) shows a large shift just after opening the craniotomy. In figure **D**, the result of the automatic volume to volume registration algorithm that moves the preoperative data (yellow) to the correct position based on information from intraoperative 3D ultrasound (green) is presented. In this case, the preoperative data was moved approximately 5 mm for correct updating.

Figure 7. Various display of intraoperative ultrasound in combination with preoperative information, pathological status and instruments. Preoperative MR data of a patient with brain tumor (**A**) was used for planning in the operating room. The sector and plane generated by the 2D probe can be visualized and controlled by the pointer during planning. After 3D ultrasound acquisition, the MR volume can be displayed together with intraoperative ultrasound (**B**). The instruments as probe, CUSA etc can also be visualized in correct position in the 3D scene using more advanced techniques, giving a more realistic display of the instrument. As surgery proceeds, updated intraoperative 3D ultrasound information for direct guidance of surgery using CUSA with tracking device can be monitored (**C**). Real time 2D ultrasound will be easier to interpret when displayed in combination with surfaces or 3D displays due to improved orientation of the slices as shown in **D**. During most brain tumor surgery, several biopsies (possible positions marked with yellow dots) are taken in order to improve the quality of surgery (**E**). Features in future navigationsystems will take care of the histo-pathological information and display this information in the correct position in the 3D scene during surgery (**F**). Simulated histo-pathological results of biopsies acquired during surgery. Biopsies were classified as tumor tissue (red) and as normal tissue (green) as displayed in **F**. Be aware that if the biopsies were guided based on preoperative MRI data, the opposite answer would be expected, but due to brain shift, the results were in accordance with the intraoperative ultrasound data.

Figure 8. Markerless registration makes it easy to use preoperative images in neuronavigation. **A.** Surface made from preoperative MRI from a healthy volunteer. **B.** Surface made from face of the same person using the optical markerless method. **C**. Matching of the two surfaces using the markerless registration algorithm. The algorithm matches the two surfaces with an accuracy below 1 mm over the area of interest. This is better than solutions offered in many commercial avalilable navigation systems today.

Figure 9. Ultrasound B-mode tissue image of a metastasis in the brain (**A**), and a strain image of the same metastasis plotted from –3‰ (blue) to 3‰ (red) (**B**). The strain values are very small, and are generated from the normal arterial pulsation in the brain. Note the bluish area in the upper left part of the image, indicating tissue elasticity that is different from the green colored areas in the tumor mass.

Figure 10: New preoperative data will in the future be available in the operating room. (**A**) Display based on fMRI and diffusion-tensor data in addition to MRI and MRA. A tumor can be seen in green, functional tongue activations in orange and the pyramidal tracts in red and dark blue. The scene constitutes important preoperative information that will be imported into future neuronavigation system, used for preoperative planning in the OR and updated using intraoperative ultrasound so that the data also can be used for guidance during surgery. (**B**) Diffusion-tensor data (red) and fMRI data (yellow) close to a tumor (white). It is important for the surgeon to know the exact location of the tracts and fMRI data also when tissue shifts during surgery.

Figure 11: Image fusion techniques are used to merge a video stream (A) with a preoperative radiological planning scene (B) to an augmented reality display (C). The video stream could also be a microscope image. The three surface rendered structures that can be observed in the 3D scene are a tumor in pink (extracted from MRI-T1 data with contrast), the vascular tree in red (extracted from MRA) and functional tongue activations in yellow (extracted from fMRI). When planning the entry point and path down to the target (in this case, a tumor) it is crucial to avoid destruction of important functional areas and vessels.

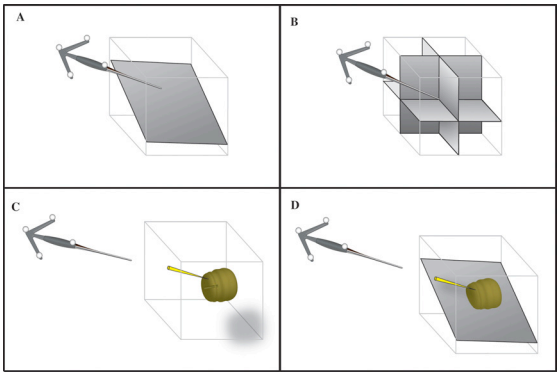

Figur 1

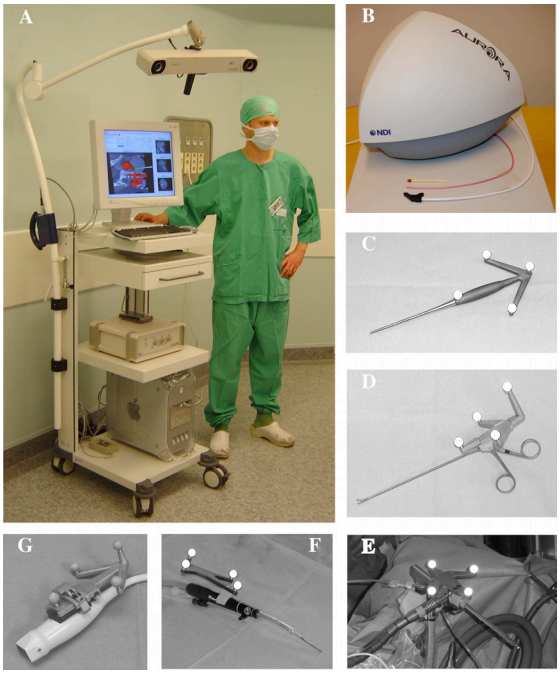

Figur 2

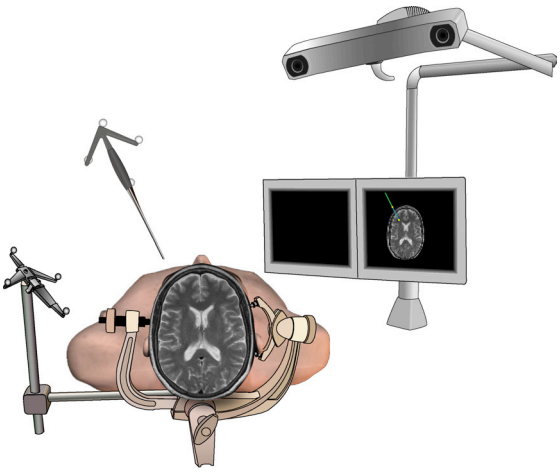

Figur 3

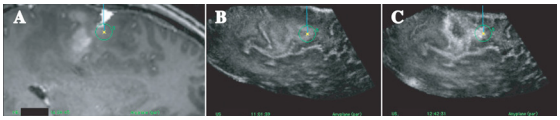

Figur 4

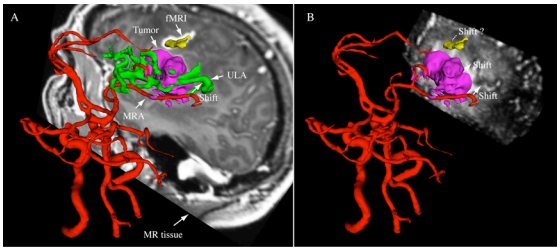

Figure 5

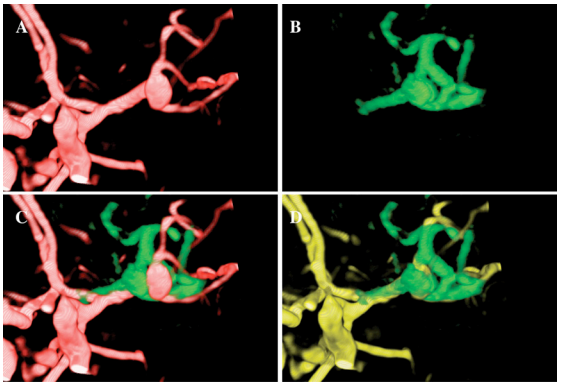

Figur 6

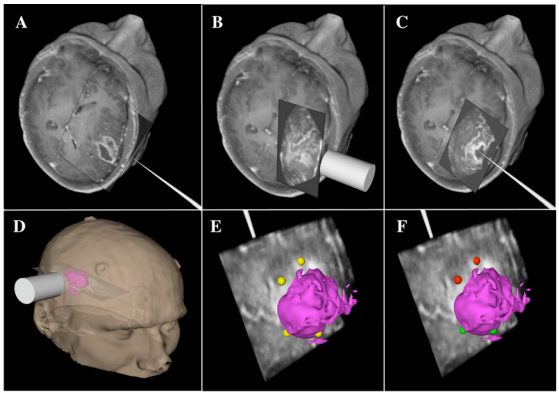

Figur 7

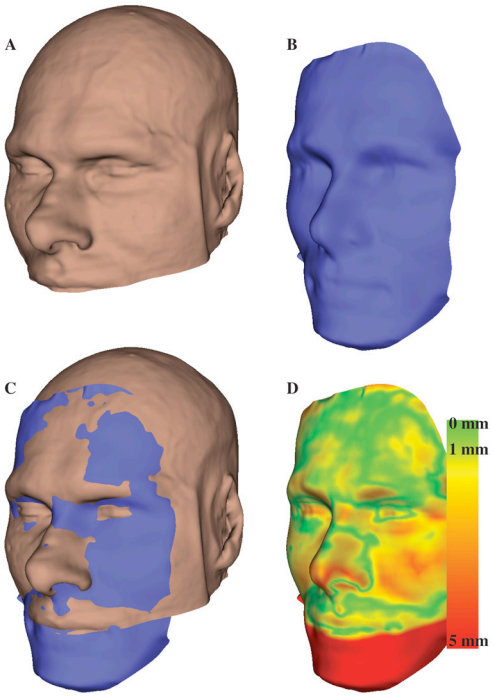

Figur 8

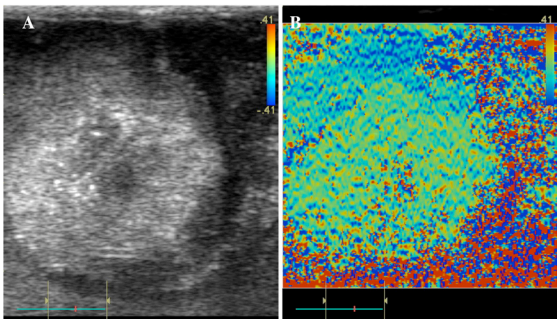

Figur 9

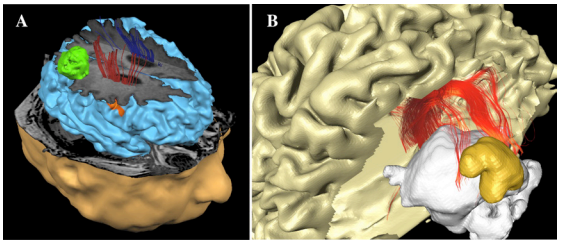

Figur 10

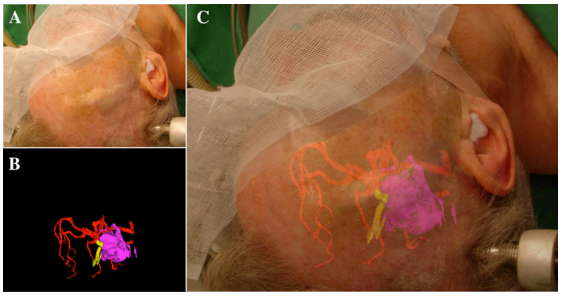

Figur 11